Design and Melting Behavior of the MSFR Freeze Plug

by

T. D. Shafer

to obtain the degree of Master of Science
at the Delft University of Technology,
to be defended publicly on Tuesday January 30, 2018 at 2:00 PM.

P&E report number:	2877	
Student number:	4421361	
Project duration:	Febuary 13, 2017 – January 30, 2018	
Thesis committee:	Dr. R. Delfos,	TU Delft, 3mE, supervisor
	Dr. Ir. W. P. Breugem,	TU Delft, 3mE
	Dr. Ir. D. Lathouwers,	TU Delft, TNW
	M. Tiberga	TU Delft, TNW

An electronic version of this thesis is available at `http://repository.tudelft.nl/`.

TU Delft

Abstract

The freeze plug is a key safety component of the molten salt fast reactor (MSFR), one of six next-generation nuclear reactor technologies being developed under the Generation IV International Forum (GIF). It should be designed to melt if an accident occurs, allowing the MSFR to drain before it incurs structural damage. Two freeze plug concepts have been considered in recent years, in which the plug is melted either through the decay heat produced in the core, or through heat generated by special heating rings and stored in steel blocks adjacent to the freeze plug. Variations consisting of both a single freeze plug, and multiple smaller plugs contained in a metal plate, have been proposed. This work seeks to evaluate the feasibility of these designs and study how parameters such as the sub-cooling of the plug affect melting times. Additionally, an alternative, wedge-shaped freeze plug design is proposed for increased reliability.

Simulations performed in COMSOL showed that the decay heat plug melts within 600 s only if placed within 0.01 m of the mixed core flow. Because such a placement makes the plug vulnerable to temperature and velocity fluctuations in the core during regular operation of the reactor, this design is considered unfeasible and is not recommended for further study. On the other hand, melting times under 600 s were possible with the heating ring design for a range of sub-cooling amounts and plug configurations, suggesting that this design is promising. A thin frozen layer was shown to form on top of the metal grate in the multi-plug configurations, preventing heat transfer through the top of the plate. Although the melting behavior of this layer warrants further investigation, its insulating effect was found to generally cause the single-plug designs to melt faster than the multi-plug designs.

A simplified, isothermal model of the wedge-shaped plug was simulated using the enthalpy-porosity approach to account for convection. To model the sinking of the wedge, an extended Darcy term approach was developed based on an analytical solution which was validated experimentally, with good agreement. This model shows that melting of the wedge is unsteady, and that melting times depend linearly on the wedge angle and sub-cooling. Unfortunately, melting times of the wedge plug could not be estimated with realistic, non-isothermal, time-dependent boundary conditions. For future study, a customizable numerical solver such as OpenFOAM is recommended, which would allow the sinking of the solid phase to be modeled more robustly through an immersed boundary method.

Acknowledgements

Thanks to Rene Delfos for the mentorship and encouragement throughout my years in Delft, and Danny Lathouwers and Marco Tiberga for their guidance throughout this project. Thanks also to Wout Cornel for helping me piece together my experiment, and to Zheng Liu and the COMSOL support team for patiently troubleshooting so many of my models.

I would certainly not be where I am today without the support and inspiration of my family and friends. Mom, Papa, Jarno: I couldn't have done this without you.

T.D. Shafer
Delft, January 2018

Nomenclature

Roman

u	Velocity vector	ms^{-1}
A	Darcy porosity function	
B	Tanh porosity function	
c	Proportionality constant	
C_A	Porosity constant (Darcy porosity function)	
C_B	Porosity constant (tanh porosity function)	
C_P	Heat capacity	$Jkg^{-1}K^{-1}$
D	Diameter	m
H	Cavity height	m
k	Thermal conductivity	$Wm^{-1}K^{-1}$
L	Length scale	m
L_H	Latent heat	Jkg^{-1}
P	Pressure	Pa
R	Radius	m
$s(t)$	Melting front position	m
S_b	Bouyancy force	
T	Temperature	K
t	Time	s
T_h	Heated wall temperature	K
T_m	Melting Temperature	K
T_{sub}	Sub-cooling amount	K
V_s	Solid sinking velocity	ms^{-1}

Greek

α	Thermal diffusivity	m^2s^{-1}
α_m	Mass fraction	
β	Thermal expansion coefficient	$kgm^{-3}K^{-1}$
ΔT	Phase change temperature range	K
Δx	Mesh element length	m
δ	Liquid film thickness	m
λ	Similarity variable	
μ	Dynamic viscosity	Pas^{-1}
ν	Kinematic viscosity	m^2s^{-1}
ρ	Density	kgm^{-3}
θ	Phase fraction	

Subscripts

l	Liquid
s	Solid

Contents

List of Figures

List of Tables

1 Introduction

Global energy consumption is projected to grow by 48% between 2012 and 2040 (EIA, 2016). Significant expansion of non-fossil energy sources, including nuclear, wind and solar, is necessary to support this demand while limiting climate change. Nuclear power plants in particular can provide a low-carbon base load energy supply that supplements intermittent energy sources like wind and solar. However, concerns about waste storage, proliferation, and accidents, especially in the aftermath of the Fukushima Daichi accident in 2011 are the root of significant public and political push back against the construction of new nuclear power plants.

The Generation IV International Forum (GIF) was formed in 2000 to accommodate these concerns and develop a new generation of nuclear reactors to help meet the world's rising energy needs. GIF is a collaboration between 14 countries to develop six nuclear reactor technologies that significantly outperform traditional Light Water Reactor (LWR) in the areas of proliferation, safety, resource saving, sustainability and waste production. One of the reactor designs being considered under GIF is the Molten Salt Fast Reactor (MSFR), which has particular advantages in the areas of safety and waste production. Notably, the MSFR uses a liquid fuel with strong negative temperature feedback that can be drained via a passively melting valve, the freeze plug, in the event of cooling or pump failure.

This thesis will address the design and feasibility of this freeze plug. The thesis structure is as follows. The remainder of this chapter provides some background on the MSFR and the freeze plug, and will outline the methodology of this thesis. Chapter 2 gives an overview of theory and literature dealing with solid-liquid phase change, and describes the relevant numerical methods available in COMSOL Multiphysics (COMSOL Inc, Burlington, MA , USA) for simulating the freeze plug. In Chapter 3, several reference studies of melting are validated in COMSOL. Finally, simulation results for three different freeze plug concepts -the SWATH design, decay heat design, and wedge shaped design- are presented in Chapters 5, 4, and 6.

1.1. Molten Salt Reactor History

Molten salt reactors were first investigated in the 1940's and 1950's under the Aircraft Nuclear Propulsion (ANP) program, which sought to develop a compact nuclear powered jet engine that would allow a strategic bomber to fly for extremely long periods of time without landing to refuel. The first molten salt reactor, the 2.5 MW_{th} Direct Current Reactor (DCR), was developed under this program as part of the Aircraft Reactor Experiment (ARE) in Oakridge National Lab (ORNL). This reactor used a molten fuel consisting of uranium flouride, sodium flouride, and zirconium flouride, and liquid sodium as coolant. Compared to traditional reactors based on solid fuel, using a liquid fuel eliminates the risk of the core melting down (since the fuel was already in a molten state), and allows the reactor to run at higher temperatures, thereby increasing the efficiency of steam generation. The DCR reached criticality and was operated for 1000 hours (on land) in 1954 (Thornton, 1963).

Although investigations into military applications of the molten salt reactor ended when ANP was shut down by John F. Kennedy in 1961, its clear potential as a civilian power reactor led ORNL to develop the Molten Salt Reactor Experiment (MSRE), a 7.5 MW_{th} test reactor designed to demonstrate the safety and feasibility of the molten salt reactor concept (Mahaffey, 2014). The MSRE reached criticality in 1965 and ran until 1969 without significant technical challenges (Haubenreich & Engel, 1970). The MSRE program was shut down in 1970, largely due to a lack of government interest in improving the existing and more technologically mature

solid-fuel light water reactor technology that was already widely used (Mahaffey, 2014).

The MSFR that was selected as a GIF generation IV reactor in 2000 is an adaptation of this original concept, reworked to overcome some of the MSRE's shortcomings. Notably, and unlike the MSRE, the MSFR does not have a solid moderator in the core, and operates on the fast neutron spectrum. In 2015, the SAMOFAR (Safety Assessment of a MOlten salt FAst Reactor) project was launched to deliver experimental proof of several of the reactor's key safety features. This thesis contributes to one component of this deliverable.

1.2. MSFR Reference Configuration

The studies done under the SAMOFAR project help inform an evolving MSFR design. The most current design, hereafter referred to as the reference configuration, is shown in figure 1.1. The reference configuration is a 3000 MW_{th} reactor operating on the Thorium fuel cycle. It includes three circuits: the fuel circuit, the intermediate circuit, and the energy conversion circuit, as well as a routine draining system (not shown) and emergency draining system, with associated storage areas.

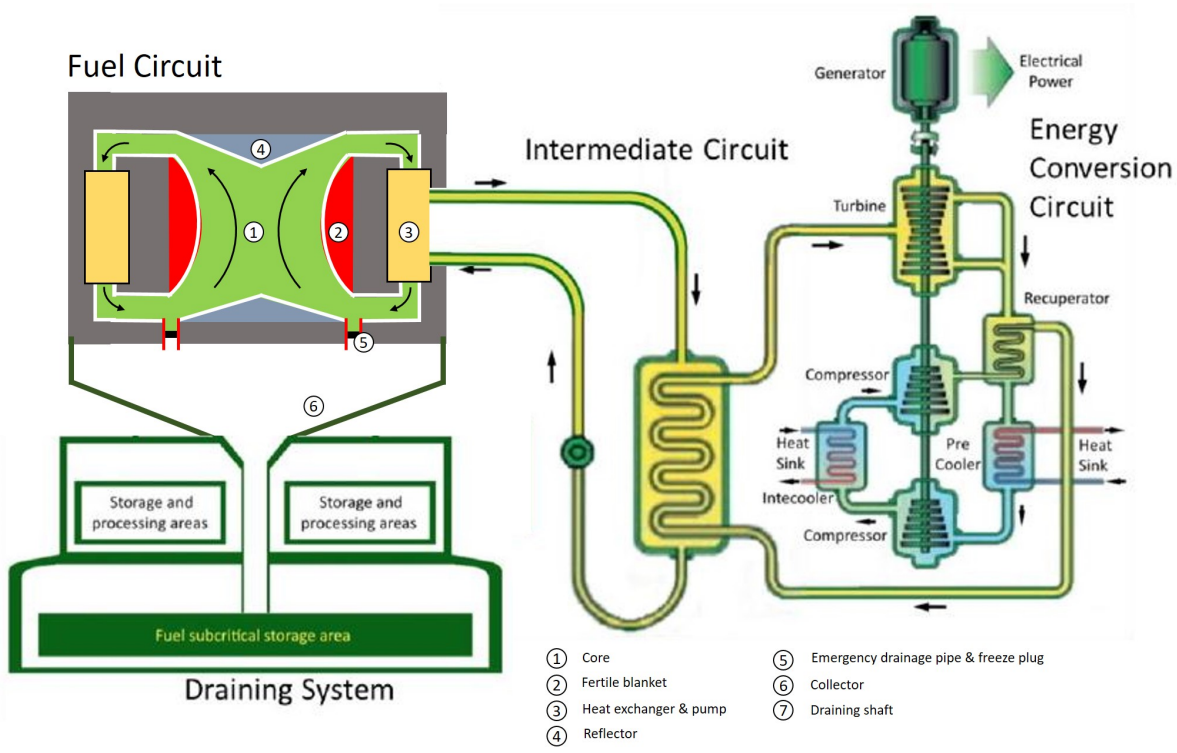

Figure 1.1: MSFR Reference Configuration. Adapted from (Allibert et al., 2016)

Fission takes place in the molten fuel salt inside the core region. Pumps drive the fuel through sixteen external fuel loops containing heat exchangers, ensuring a temperature drop of 100 K between the inlet and outlet of the fuel loop. Neutronic reflectors are located at the lower and upper walls of the reactor, while the side walls contain a fertile blanket for breeding thorium.

Based on the most recent recommendations made under the SAMOFAR project (Allibert et al., 2016), the reactor will contain both a routine draining system, designed to contain the fuel during regular maintenance work, and an emergency draining system. In the case of emergency, several passive valves (i.e., freeze plugs), located at the bottom of the reactor core are triggered to open to allow the fuel salt to flow into the draining tank underneath. The fuel is transferred to the draining tank via pipes running through the bottom of the reflector. From these pipes, the fuel drains into a funnel-shaped collector which leads to the main draining shaft, and to the passive storage tank below. Similar valves are also located at the bottom of the actively cooled maintenance storage tanks, though these lie outside the scope of this thesis.

1.2.1. MSFR freeze plug

The freeze plug is a critical safety component of the MSFR. It is a passive valve consisting of a plug of frozen fuel salt designed to melt in the event of an accident that requires the draining of the reactor core. Potential accidents scenarios which might invoke the use of a freeze plug include failure of the heat exchangers and/or pump, and power loss to the reactor (which would cause the former). In a worst case scenario in which both the pumps and heat exchangers fail, the MSFR will immediately become sub-critical. Without a heat sink, however, the decay heat generated by fission products will cause the temperature in the core to rise. To avoid structural damage to the reactor, Brovchenko et al. (2013) recommend that the fuel salt must be drained before reaching the critical temperature of 1473K.

Design history The freeze plug valve was first used in the ORNL MSRE design of the 1960's. The original ORNL freeze plug was formed by first raising the molten salt into the core by applying pressure below the location of the plug and then applying a cooling gas flow to the outside of the pipe. In this design, an airflow of 115 m^3/h were used to form the plug, while 25 m^3/h was used to keep the plug frozen. The plug was designed to melt when the cooling supply was turned off, by using either the residual heat in the pipe adjacent to the freeze plug, or by turning on heaters adjacent to the drainage pipe. The ONRL design contained 12 different freeze plugs based on the same principle, including a horizontal plug in the reactor drain and fill pipe with an analogous purpose to the freeze plugs in the emergency drain pipes of the MSFR. This plug was formed in a flattened section of pipe with dimensions 2.0 x 6.3 x 5.0 cm and was capable of thawing in 5 minutes with the use of a thermocouple heater, and in < 10 minutes without the heater (Robertson, 1965).

Current MSFR freeze plug The reference configuration of the MSFR includes a vertical freeze plug, based on the ORNL design, at the base of each of the sixteen fuel loops in the reactor core, as shown in Figure 1.2.

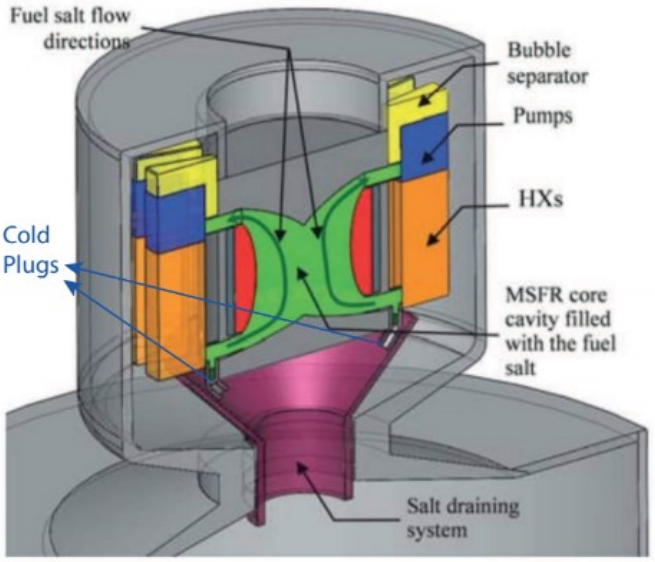

Figure 1.2: Location of the freeze plugs in the MSFR (Ghetta et al., 2017b)

Unlike the ORNL design, the freeze plugs in the MSFR must work passively, (i.e., without an active power input after power loss). These freeze plugs will be located in the drainage pipes between the reactor core and collector, and must be some distance away from the reactor core to allow room for cooling and heating equipment. A preliminary freeze plug geometry, shown in Figure 1.3, has been developed under SAMOFAR for the ongoing Thermal ExcHanges (SWATH) experiments, and will be used to study the solidification process and melting time of the plug both experimentally and numerically. In this preliminary design, hereafter referred to as the 'SWATH design', the plug is formed around a copper plate which is cooled with pressurized air during operation. The plug is surrounded by a steel block that stores heat generated by heating rings above and below the plug. When the cooling system shuts off, the thermal energy stored in this steel mass will be transferred to the copper disk by conduction, causing the freeze plug to melt (Ghetta et al., 2017b). Before this

design was developed, a different concept was considered which instead relies only on decay heat to melt the plug. This will hereafter be referred to as the 'decay heat design'. Schematics of the two designs are shown in Figure 1.3.

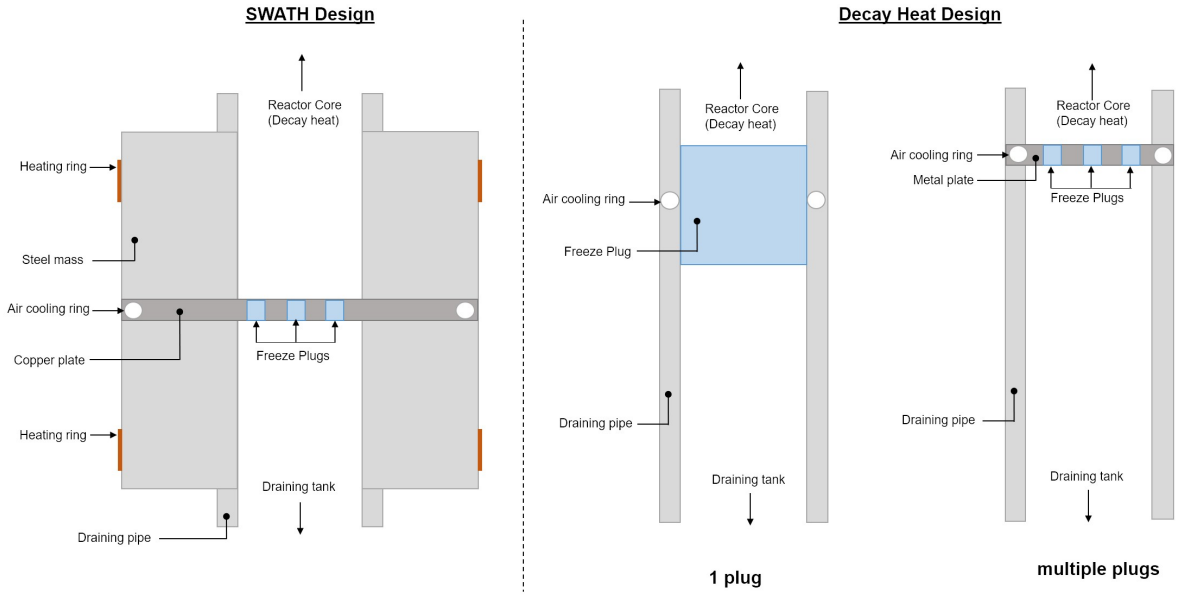

Figure 1.3: Left: Schematic of the SWATH freeze plug design (adapted from (Ghetta et al., 2017b)). Right: Decay heat design featuring both one-plug and multiple-plug configurations.

1.2.2. Previous work on the decay heat freeze plug

Past work on the MSFR freeze plug has been focused on the decay heat design. Both a single-plug design, which contains one plug occupying the full width of the draining pipe, and the multi-plug design, which consists of several smaller freeze plugs contained in a metal plate, have been considered (see Figure 1.3). The single-plug design was studied most extensively by Swaroop (2016), who specifically considered how heat transfer to the freeze plug is affected by convection in the draining pipe above it. This work found that significant thermal stratification can be expected in the draining pipe above the freeze plug, such that the decay heat in the core is overwhelmingly transported to the plug by conduction. This is quite inefficient since the fuel salt has a low conductive heat transfer coefficient (see material properties in Section 2.1). Consequently, the freeze plug has to be located extremely close to the reactor core in order to melt quickly enough. It is important to note that this study only considered melting through the top surface of the freeze plug: melting of the plug through the sides, due to conduction of decay heat through the draining pipe, was not taken into account. This means that Swaroop (2016) assumed that the entire mass of the freeze plug would have to be melted in order for the plug to drop, failing to consider the possibility that the sides of the freeze plug might melt and detach from the draining pipe long before this happens.

Several studies have also considered a freeze plug concept consisting of multiple cylindrical plugs in a metal plate. These studies supposed that using multiple plugs inside a plate could accelerate melting by reducing the total volume that needs to be melted and by increasing heat transfer through the sides of the plugs. A recent study by Makkinje (2017) specifically sought to optimize the size and spacing between freeze plugs in such a design to minimize the combined melting and draining time. Considering a Hastelloy-N grate, this study found that increasing the spacing between freeze plugs speeds up melting until the space between plugs reaches approximately 1/2 the freeze plug diameter, after which gains in melting times become insignificant. Deurvorst (2017) found that the melting speed could be further reduced by introducing vertical heat fins to the top of the plate to conduct decay heat from the core, while van Tuyll (2016) found that incorporating a more conductive material like copper into the Hastelloy-N grate could also reduce melting times by improving heat transfer to the sides of the plugs. The conclusion (and, indeed, guiding assumption) in all of these studies -that a multi-plug design melts more quickly than a single plug design- is predicated on the assumption that the metal grate efficiently conducts heat to the sides of the plugs. To model this, the COMSOL simulations of Makkinje (2017), Deurvorst (2017) and van Tuyll (2016) all used a constant temperature

boundary condition applied directly at the top of the metal plate and freeze plugs throughout the melting process. This is only accurate if the freeze plugs are perfectly contained within the holes of metal grate, and is no longer conservative in the more realistic event that frozen salt builds up on the outside of the plate.

1.2.3. Freeze plug design criteria

The purpose of the freeze plug can be summarized by two design criteria:

1. In the event of an accident (e.g., power loss), the plug must melt in time to allow the reactor to drain before the temperature of the fuel reaches 1473K.

2. The plug must not melt or fall out unless an accident occurs. This means that it must withstand the pressure in the reactor and potential velocity and temperature fluctuations without failing.

1.2.4. (Lack of) design constraints

In order to design a plug that achieves the design criteria in Section 1.2.3, concrete constraints on the freeze plug's melting time, position, and sub-cooling temperature are required, since these are the primary drivers of the plug's performance. Unfortunately, these cannot be established until it is known how the plug is formed and cooled, and until the thermohydraulics of a finalized MSFR design have been studied in more detail. In the absence of key constraints, these factors will therefore be treated as free parameters in this thesis. Once more constraints are known, a design can be chosen that complies with them. These parameters, which are studied in detail in this thesis along with other design parameters related to the geometry of the freeze plugs, include:

- **Melting time** The freeze plug should be designed to melt and allow the reactor to drain before the reactor reaches the critical temperature of approximately 1200°C. Although there is no definitive estimate for how long this will take, previous estimates suggest between 480 s (Brovchenko et al., 2013) to 1600 s (Ghetta et al., 2017a), (see Section 2.2). Because of this uncertainty, this thesis will avoid making claims about the feasibility of freeze plug designs based on melting time alone.

- **Plug position** The freeze plug must be located some distance down the draining pipe, away from the reactor core, to make room for electrical equipment on the outside of the draining pipe (Ghetta et al., 2017b). Unfortunately, the size of this distance will depend on practical construction considerations and can therefore not be estimated until the cooling mechanism is finalized and prototyped. Maintaining the plug some distance from the core is also important for the reliability of the plug. As mentioned previously, the flow and temperature conditions in the reactor are not well understood at present, particularly not in the accident conditions which would trigger the melting of the freeze plug. Placing the plug too close to the reactor core, where it is the most reactive to the temperature and flow conditions, also makes the plug vulnerable to still unknown temperature and velocity fluctuations that may cause the plug to melt prematurely. In the absence of more accurate thermohydraulic data, it is therefore considered advantageous to shield the plug from the conditions in the core as much as possible by locating the plug further down the draining pipe.

- **Plug sub-cooling** It is unrealistic for the freeze plug to have a uniform temperature equivalent to the melting temperature, T_m. Instead, the plug will have a temperature gradient, with temperatures ranging from $T = T_m$ at the melting front to a minimum sub-cooled temperature $T = T_m - T_{sub}$ at a point closest to the cooling source. Some sub-cooling will be necessary to freeze the plug fully and protect against variability in the cooling source. Keeping T_{sub} too small increases the possibility of the plug melting prematurely, for example due to variability in the cooling source, or core temperature. On the other hand, choosing T_{sub} to be too large will slow down the melting process substantially, as will be discussed in more detail in Section 2.5.

1.3. Open Questions

No simulations or experimental investigations of the SWATH heat plug design have been conducted at the time of this thesis. At this stage, it would be valuable to develop a preliminary understanding of how various parameters such as the intensity of cooling, and the design of the freeze plug (e.g., a single plug or multiple plugs in a grate) affect the melting times. Identifying what parameters have the most effect on the melting

time of the freeze plug would be particularly valuable to guide the research questions of upcoming experimental work.

Quite some research has already been done on the MSFR decay heat freeze plug design. The conclusions from these studies - that the single-plug design is unfeasible (Swaroop, 2016), while various configurations of the multi-plug designs melt well within 100 s (Deurvorst (2017); Makkinje (2017); van Tuyll (2016))- are based on very simplistic COMSOL simulations, and leave quite some open questions for further study. In particular, the role that the realistic solidified shape of the freeze plug (including likely salt build up on the outside of the plate) plays in the melting process of the multi-plug design has not yet been considered. For the single-plug design, it would additionally be valuable to understand the role that heat transfer through the draining pipe plays in melting.

Finally, all previous studies of the freeze plug have assumed a cylindrical plug shape with a 1-to-1 height to diameter aspect ratio in order to maximize the surface area to volume ratio of the plugs, since the friction acting between the frozen salt plugs and a metal enclosure is not known. In reality, it is not known whether the plugs that have been studied will withstand the hydrostatic pressure in the core during transient reactor operation without falling out prematurely. In order to address this uncertainty, an alternative plug design that does not rely on friction to stay in place may be desirable.

1.4. Research goals

Based on the open questions above, the central research question driving this thesis is:

> *What are the most important determinants of melting time for the decay heat and SWATH freeze plug designs, and how do melting times vary within realistic ranges of these parameters?*

A wedge-shaped plug design, which takes advantage of contact melting has been recommended to improve the stability and reliability of the freeze plug. The secondary research question addressed in this thesis is therefore:

> *Can a wedge-shaped freeze plug improve the stability of the freeze plug without increasing melting times significantly?*

The questions presented above were addressed by modeling the different freeze plug designs in COMSOL. Following this thesis, more extensive experimental and numerical studies, such as those proposed in the SWATH experiments, will be performed to finalize the freeze plug design. In addition to more elaborate studies of the plug solidification and melting time, work will be done to estimate the thermodynamic properties of the solidified fuel salt which are currently unknown (Ghetta et al., 2017b).

2

Background and Theory

In this thesis, three different freeze plug designs are studied: the original decay heat plug is studied in Chapter 5, the SWATH heat ring plug is studied in Chapter 4, and a new, wedge shaped plug is discussed in Chapter 6. This chapter presents background information required to study these plugs. First, the material properties of the freeze plug are described in Section 2.1, and the velocity and temperature distribution in the MSFR after shutdown are presented in Section 2.2. Next, Section 2.3 describes the theory behind the flow in the MSFR draining pipe, which resembles non-isothermal cavity driven flow and discusses its relevance to the freeze plug design.

Next, the theoretical and mathematical background applied in this study is presented. Section 2.5 gives an overview of the analytical melting problem considering conduction only. Two popular numerical methods applied to macroscopic melting problems, which can be broadly categorized as either transformed grid or fixed grid methods (Lacroix & Voller, 1990), are described in Sections 2.6 and 2.7. Next, the different modes of heat transfer involved in a system undergoing solid-liquid phase change like the MSFR freeze plug are discussed. Melting with convection is discussed in Section 2.8, and close contact melting is discussed in Section 2.9.

2.1. Materials and Fuel Composition

The fuel used in the MSFR reference configuration will be either LiF-ThF_4-$^{233}UF_4$ or LiF-ThF_4-$^{enr}UF_4$-(Pu-MA)F_3, with a LiF content of approximately 77.5% for both fuels (Ghetta et al., 2017a). The reference fuel for the reactor is LiF-ThF_4 (78-22 mol%), which has comparable physico-chemical properties to the candidate fuels in the liquid phase. The high melting point of LiF-ThF_4 (841K) makes this fuel impractical for experimental facilities due to the high working temperatures required. For this reason, LiF-NaF-KF (6.5-11.5-42 mol%), commonly known as 'FliNaK', which has a lower melting temperature (727K) will be used in the SWATH experiments (Ghetta et al., 2017a).

In addition to the lower melting temperature, attention should be drawn to the fact that FliNaK has a significantly lower latent heat, L, than the reference fuel, which increases its melt rate substantially as will be discussed at greater length in Section 2.5. Both FliNaK and LiF-ThF_4 have extremely low thermal conductivities and therefore transport heat more efficiently by convection than by conduction. It should also be noted that prior studies of the freeze plug (for example Swaroop (2016), Makkinje (2017), and Deurvorst (2017)) have substituted CsCl for the reference fuel in the solid state because its solid and liquid state properties are included in the COMSOL material library. While the density, thermal conductivity, latent heat of fusion, and melting temperature of CsCl are comperable to LiF-ThF_4, the heat capacity of CsCl is only about one third the heat capacity of LiF-ThF_4. As will be discussed at greater length in Section 2.5, this means that a smaller heat flux is required to raise CsCl to the melting temperature, and that the melting results from these studies are not conservative.

The reactor vessel and draining pipes will be made of Hastelloy-N (Allibert et al., 2016). Additionally, copper is used in the SWATH design to increase heat transfer to the freeze plug. To simplify the setup of COMSOL simulations, material properties are assumed to be constant with temperature in both the solid and liquid phases. Relevant material properties are listed in Table 2.1.

Table 2.1: Material Properties

Property	Units	Reactor		Fuel Salt			
				FliNaK[a]		**LiF-ThF$_4$**[b]	
		Hastelloy-N	**Copper**	Solid[c]	Liquid [d]	Solid [e]	Liquid
Thermal Conductivity (k)	W·m^{-1}K^{-1}	23.6	401	0.92 [f]	0.92	1.5 [f]	1.5
Density (ρ)	kg·m^{-3}	8860	8960	2360	2020	4502	4390
Heat Capacity (C_p)	J·kg^{-1}K^{-1}	578	377	1332	1658	815	1000
Dynamic Viscosity (μ)	Pa · s	-	-	-	0.0029	-	0.01
Latent Heat (L_H)	J·kg^{-1}	-	-	$1.857 \cdot 10^4$[g]		$1.59 \cdot 10^5$[h]	
Melting Temperature (T_m)	K	-	-	727		841	

[a] 6.5-11.5-42 mol%. Properties from Williams et al. (2006)
[b] 78-22 mol%. Properties from Benes & Konings (2009)
[c] Solid FliNaK properties given for 702K, based on subcooling of $T_m - 25K$ and calculated by weighted average based on molar mass percentage
[d] All fluid properties provided at 923K, the average steady state fuel temperature
[e] Solid LiF-ThF$_4$ properties given for 816K, based on subcooling of $T_m - 25K$, and calculated by weighted average based on molar mass percentage
[f] Thermal conductivity of solid phase assumed to be identical to liquid conductivity
[g] Williams (2006)
[h] Derived from data in Capelli et al. (2013)

2.2. Temperature and Velocity After Shutdown

During operation, a temperature difference of 100 K is present in the MSFR between the inlet and outlet of the heat exchanger loops. After power loss (i.e., a worst case scenario in which both the pumps and heat exchangers fail), turbulent mixing in the reactor causes the temperature to smear out rapidly. The residual heat in the reactor is estimated to follow a logarithmic fit (Allibert et al., 2016; Ghetta et al., 2017a):

$$Q = 6.45908 \cdot 10^6 - 6.9200 \cdot 10^5 \ln(t[s]) \qquad \mathrm{W/m^2}. \tag{2.1}$$

Assuming a lumped capacitance model and assuming no external heat losses, we have $Q = \rho C_p \frac{dT}{dt}$. The mean temperature in the reactor can now be computed for a certain time interval, dt, from Equation 2.1. Fitting a line to the resulting temperature distribution, shown in Figure 2.1, gives a function for the temperature after power loss (Equation 2.2).

$$T(t) = -0.0001t^2 + 0.5244t + 923 \quad \mathrm{K} \tag{2.2}$$

According to this simplistic estimate, the temperature in the reactor reaches the critical temperature of 1473 K 1630 s after power loss[1]. This is substantially longer than the estimate made by Brovchenko et al. (2013), who estimated that the reactor would reach 1473K within 480 s.

It should be emphasized that this estimate of the temperature evolution is a rough approximation, stemming from a simplistic model. At the time of the writing of this thesis, the MSFR design has not been finished, and no detailed thermohydraulic studies have been conducted which would give accurate information specific to the kind of accident scenario expected to trigger the melting of the freeze plug.

The mean velocity in the reactor during transient operation is 1.4 m/s (Ghetta et al., 2017a).As shown in Figure 2.1, the velocity decays rapidly after reactor shutdown, to just 25% of the initial velocity after two seconds, after which time the decay is more gradual. Again, this velocity evolution is rough approximation. Moreover, the freeze plugs are to be located at the base of the reactor's concentric recirculation loops where the velocity may be higher than the mean.

2.3. Non-Isothermal Driven Cavity Flow

Driven cavity flow is a common benchmark for numerical flow simulations, and numerous reference studies exist for driven cavity flow in cavities with different aspect ratios and for Reynolds numbers up to $2 \cdot 10^4$ (Erturk

[1] This is not entirely conservative. Equation 2.1 was obtained from Ghetta et al. (2017a), and was derived using data in Allibert et al. (2016) for the first 300 s after shutdown only. This equation underestimates heat production at longer times. The raw data in Allibert et al. (2016) suggests that the critical temperature of 1200°C is reached in 1340 s, not 1630 s.

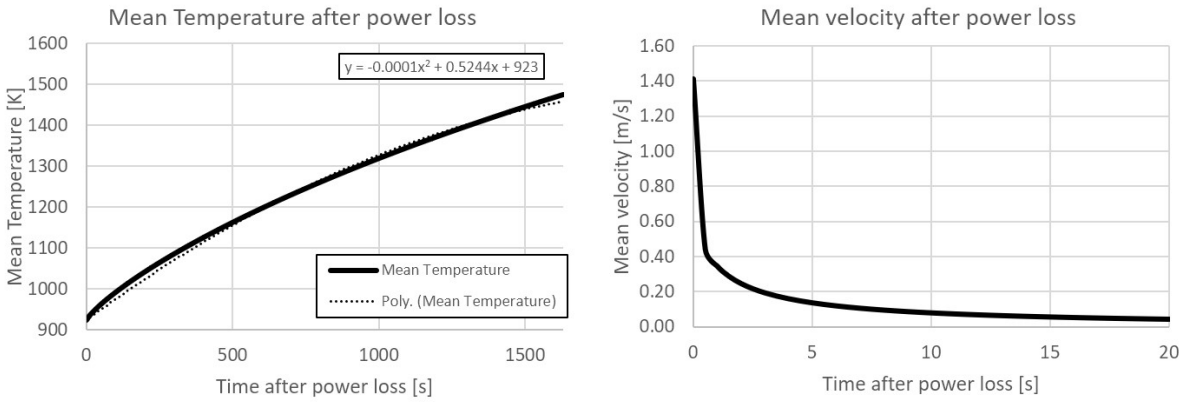

Figure 2.1: Left: Mean temperature in the MSFR core after shutdown. Right: Mean velocity after shutdown (Tano, 2017)

.

et al., 2005). By comparison, non-isothermal driven cavity flow, in which a temperature gradient exists in the cavity, has been studied relatively little. The case of a stable temperature gradient, in which the top of the cavity is maintained at a higher temperature than the bottom of the cavity, is particularly relevant to this thesis. If the velocity at the top of the cavity is zero, the fluid in the cavity is stratified and gravitationally stable, and conduction is the only heat transfer mechanism in the cavity. When lid-driven flow is introduced, forced convection will bring fluid flow into the cavity and increase the heat transfer rate. The degree to which such lid driven motion increases heat transfer is governed by the bulk Richardson number, which describes the ratio of lid-driven forced convection to bouyancy driven natural convection:

$$\mathrm{Ri} = \frac{\mathrm{Gr}}{\mathrm{Re}^2}, \qquad \text{where} \qquad \mathrm{Gr} = \frac{g\beta(T_\infty - T_m)H^3}{\nu^2}. \tag{2.3}$$

Here, the length scale of the Reynolds number is the width of the cavity, while the length scale in the Grashof number is the cavity height. The following observations were made by Iwatsu et al. (1993) on a square, 2-D geometry, for Reynolds numbers Re < 3000:

Ri << 1,	bouyancy effect are dominated by forced convection. Flow resembles conventional lid-driven flow.
Ri ≥ $O(1)$,	bouyancy effects become noticeable, but convective heat transport is still significant;
Ri >> 1,	bouyancy effects dominate. Flow is stratified in majority of the cavity, and heat transfer is primarily by conduction.

For flow described by Ri ~ $O(1)$, the dominant mode of heat transfer is strongly dependent on the Prandtl number (Iwatsu et al., 1993). When Pr << 1, The thermal boundary layer is significantly thicker than the momentum boundary layer, the temperature distribution in the cavity is mostly linear, and conduction dominates the heat transfer process. With Pr > 1 on the other hand, a strong circulatory cell in the cavity ensures that convective heat transfer plays a role in the top portion of the cavity, while conduction still dominates near the bottom. Similar relationships have been observed in 3-D simulations of a square cavity (Iwatsu & Hyun, 1995).

Because the mean velocity in the core is expected to decrease rapidly after shutdown, the Reynolds number in the fluid cavity in the draining pipe above the freeze plug decreases rapidly as well, from $1.74 \cdot 10^5$ (turbulent flow) during transient reactor operation, to $2.39 \cdot 10^3$ (laminar flow) just 50 s after power loss for a draining pipe with diameter $D = 0.2$ m. For a cavity with a height of 0.2 m, the Bulk Richardson number simultaneously increases from 72 (partially stratified flow) to $5.68 \cdot 10^5$ (fully stratified flow), while the Prandtl number of LiF-ThF_4 is Pr = 6.67. Figure 2.2 shows the increase of Ri with time for different cavity heights.

Thus, while we can expect considerable mixing between the core flow and the draining pipe cavity during transient operation, this mixing will likely be suppressed rapidly after power loss due to the decaying core velocity and increasing core temperature. Since conduction dominates the heat transfer to the freeze plug

after power loss, convection (due to the flow in the reactor core) will be ignored in the remainder of this thesis.

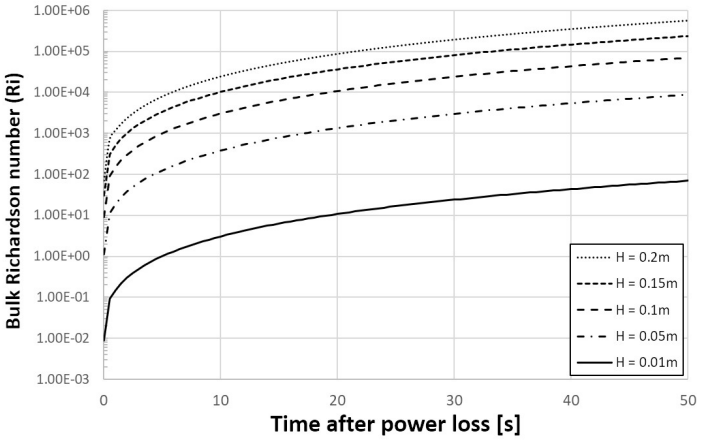

Figure 2.2: Bulk Richardson number after power loss for increasing height of the draining cavity above the freeze plug.

2.4. Draining of the Reactor

It is important that the freeze plug both melts in time, and allows the reactor to drain sufficiently quickly. An analytical model for the draining time for a representative reactor was derived by Wang et al. (2016), and showed good agreement with a more recent model of the draining process which uses the volume of fluid (VoF) method in Fluent (Ansys, Canonsburg, PA, USA) (Ghetta et al., 2017a). The time required to drain the reactor depends on the length and width of the draining pipe, and the degree to which the freeze plug obstructs the pipe (either due to partial melting of the plug, or with a design consisting of a single freeze plug encased in a metal plate). Figure 2.3a shows that the reactor drains in 95 s with a draining pipe length of 2.0 m and pipe diameter of 0.2 m, and that draining times increase sharply for smaller diameters. For this reason, a draining pipe diameter of 0.2 m is assumed throughout this thesis for efficient draining.

Figure 2.3b further shows that draining times increase to approximately 250 s when the diameter of the freeze plug is reduced to 0.1 m. The relationship shown in Figure 2.3b is based on pressure losses through a single hole, which is a conservative estimate for pressure losses through a multi-hole plate with the same ratio of open area to a given pipe cross section (Malavasi et al., 2012).

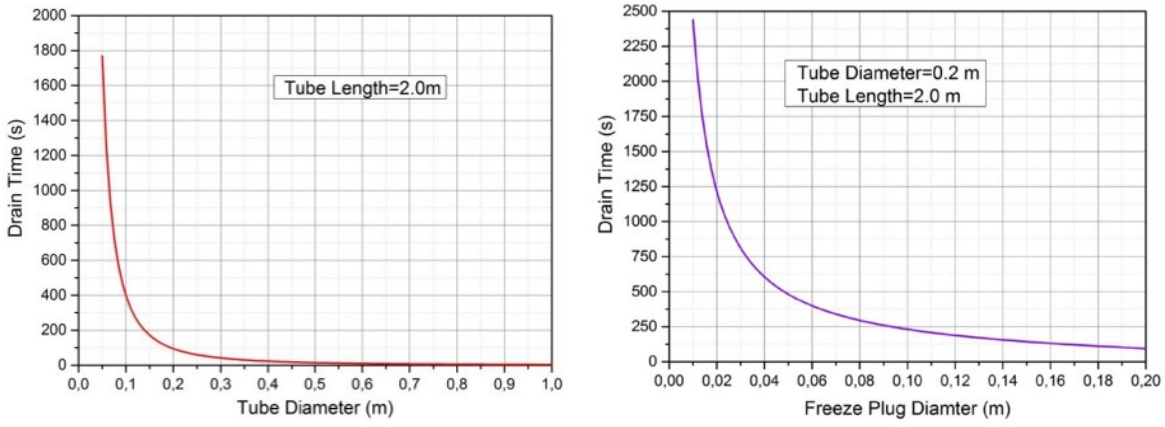

(a) **(b)**

Figure 2.3: Draining time as a function of the draining pipe diameter (Figure 2.3a) and freeze plug diameter (Figure 2.3b). A draining pipe length of 2.0 m is assumed. From Wang et al. (2016).

2.5. Analytical Melting Problem

Melting is characterized by the absorption of latent heat at the phase change temperature, T_m. A material kept below T_m is said to be sub-cooled, with its temperature given by $T = T_m - T_{sub}$. The state relations describing solid-liquid phase change in terms of the temperature and thermal energy content, e, of a material is shown in Figure 2.4. When thermal energy is added to the material, it increases in temperature linearly until reaching T_m. The material remains at T_m until it has acquired sufficient energy to overcome the binding forces that maintain its solid structure. This energy is the latent heat L_H of a material, and represents the difference in thermal energy between a material's solid and liquid states (Alexiades & Solomon, 1993). The phase change interface refers to the region where solid and liquid phases coexist. For most pure or eutectic materials, this interface is a sharp front with negligible thickness. For impure materials, this interface may have an apparent thickness commonly described as a "mushy zone".

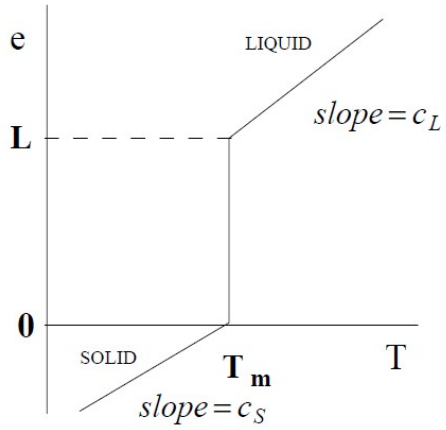

Figure 2.4: State relation, showing thermal energy e = e(T) for material with constant c_L (Alexiades & Solomon, 1993)

A general characteristic of phase change problems is that, in addition to the temperature distribution, the location of the phase change interface is unknown. This means that, beside the heat equation for both solid and liquid phases (Equations 2.4 and 2.5) an additional condition is required to describe the location of the phase change interface. An analytical description of this position is given by the Stefan condition (Equation 2.6), which relates the melting front normal velocity, $\frac{ds}{dt}$, to the difference in heat flux over the melting front:

$$\frac{\partial T_l}{\partial t} = \alpha_l \frac{\partial^2 T_l}{\partial x^2}, \qquad \text{Heat conduction in liquid;} \tag{2.4}$$

$$\frac{\partial T_s}{\partial t} = \alpha_s \frac{\partial^2 T_s}{\partial x^2}, \qquad \text{Heat conduction in solid;} \tag{2.5}$$

$$k_s \frac{\partial T_s}{\partial x} - k_l \frac{\partial T_l}{\partial x} = L_H \rho_s \frac{ds}{dt}, \qquad \text{Stefan condition at boundary.} \tag{2.6}$$

Analytical solutions to the Stefan condition exist only for the most simple cases. For example, the Neumann solution (Equation 2.7) describes the position of the phase change boundary, $s(t)$, for a 1D problem with isotropic heat transfer by conduction only:

$$s(t) = 2\lambda\sqrt{\alpha_l t}. \tag{2.7}$$

In this solution, the latent heat is assumed to be constant, thermophysical properties are assumed to be constant in the solid and liquid phases, and phase change is assumed to occur at a fixed temperature. λ is the solution to the transcendental equation

$$\frac{\mathrm{St}_l}{e^{\lambda^2}\,\mathrm{erf}(\lambda)} - \frac{\mathrm{St}_s\sqrt{\alpha_s}}{\sqrt{\alpha_l}e^{\frac{\alpha_l\lambda^2}{\alpha_s}}\,\mathrm{erf}\left(\lambda\sqrt{\frac{\alpha_l}{\alpha_s}}\right)} = \lambda\sqrt{\pi}, \tag{2.8}$$

where the liquid and solid Stefan numbers, St_l and St_s, are defined in Equations 2.14 and 2.15. It is evident from the Neumann solution to this simple 1D problem that melting by conduction progresses at $s(t) \propto \sqrt{t}$. In

the event that the latent heat is much greater than the specific heat capacity, the effects of differences in the material properties of the solid and liquid phases vanish, and a simple approximation exists for λ (Kowalewski & Gobin, 2004):

$$\lim_{\mathrm{St}_l \to 0} \lambda = \sqrt{\mathrm{St}_l/2}. \tag{2.9}$$

Additional insight is gained by rewriting the Stefan condition in non-dimensional form:

$$-\frac{\partial \theta_l}{\partial x} + \Delta T^* k^* \frac{\partial \theta_s}{\partial x} = \frac{\rho^*}{\mathrm{St}} \frac{ds}{dt}, \tag{2.10}$$

with the temperature, density, and heat conductivity non-dimensionalized as follows:

$$\theta_s = \frac{T_s - T_m}{T_{sub} - T_m} \qquad \theta_l = \frac{T_l - T_m}{T_\infty - T_m}, \tag{2.11}$$

$$\rho^* = \frac{\rho_l}{\rho_s} \qquad k^* = \frac{k_l}{k_s}. \tag{2.12}$$

Equation 2.10 shows that the melting velocity in conduction-dominated melting is controlled by the non-dimensional sub cooling number and the Stefan number in both liquid and solid phases:

$$\Delta T^* = \frac{T_{sub} - T_m}{T_\infty - T_m}, \quad \text{Sub-cooling number;} \tag{2.13}$$

$$\mathrm{St}_l = \frac{C_{p_l}(T_\infty - T_m)}{L_H}, \quad \text{Stefan number, liquid;} \tag{2.14}$$

$$\mathrm{St}_s = \frac{C_{P_s}(T_\infty - T_m)}{L_H}, \quad \text{Stefan number, solid;} \tag{2.15}$$

Whereas the Stefan number, which may be seen as a measure of sensible heat storage, is proportional to the melt rate, the initial sub-cooling of the solid retards the melting process. This is because when the initial temperature of the solid is below its melting temperature, a portion of the energy delivered to the melting front is used to raise its temperature, rather than melting the solid (Sparrow & Broadbent, 1982).

2.6. Transformed Grid Method

The transformed grid method uses a body-fitted curvilinear grid to precisely fit the solid-liquid interface location. In this method, boundary conditions can be applied directly to the melting interface, which is explicitly tracked by applying the normal interface velocity from Equation 2.6 to the melting front at each time step. This method models the melting front as a sharp interface and is therefore well suited for pure or eutectic materials. The moving boundary method included in COMSOL is called the Deformed Geometry Method.

One major challenge with this method is that, since the melting front is continuously tracked, it must also be defined for every time step in a simulation. This makes the method poorly suited for most realistic melting problems, which may contain multiple fronts, or fronts which appear and/or disappear over the course of the melting process. This also means that this method is poorly suited for studying the freeze plug. Consider, for instance, a single freeze plug in a cooling pipe. During transient conditions and at the beginning of the melting process this freeze plug only has one melting front at the top of the plug. Later on, new melting fronts will appear at the sides of the plug. In order to apply the deformed geometry method to this problem, these melting fronts have to be predefined at the beginning of the simulation by introducing a thin fluid layer between the plug and the cooling pipe. This is an unphysical representation of the problem and additionally means that no sub-cooling temperature, T_{sub}, can be applied to the plug. The apparent heat capacity method described below is more versatile in this regard and is therefore favored.

2.7. Enthalpy-Porosity Method

There are a variety of fixed grid methods for modeling solid-liquid phase change (see review by Voller et al. (1990)). Of these, the apparent heat capacity method is widely used and available in COMSOL. This method involves reformulating the heat equation to account for the enthalpy jump at the phase change interface. This

method is popular because of it's versatility and convenience: it is easy to adapt to complex geometries, and is easy to implement since the governing equations have the same form as the heat equation (Jin et al., 2018). In this method, the melting front is implicitly tracked by smearing the phase change region over several grid cells, and the Stefan condition is only implicitly incorporated. To account for convection, the apparent heat capacity method may be reformulated into the enthalpy-porosity method from Brent et al. (1988) by adding a source term to the momentum equation to ensure that the zero velocity condition in the solid region of the PCM remains satisfied.

2.7.1. Apparent heat capacity method

In the apparent heat capacity method, the enthalpy jump at the phase change boundary is accounted for through a modified heat capacity term, C_{app}. To avoid problems associated with a jump in material properties at $T = T_m$, a small artificial temperature region, ΔT, is introduced over which phase change occurs. The modified heat capacity term, C_{app}, can then be defined to account for the latent heat in terms of the solid and liquid phase fraction in a given cell undergoing phase change:

$$C_{app} = \begin{cases} C_{pl} & T > T_m + \Delta T, & \text{Liquid phase;} \\ \frac{1}{\rho}(\theta_l \rho_l C_{pl} + \theta_s \rho_s C_{ps}) + L_H \frac{d\alpha_m}{dT} & T_m - \Delta T < T < T_m + \Delta T, & \text{Mushy zone;} \\ C_{ps} & T_m - \Delta T \geq T, & \text{Solid phase,} \end{cases} \tag{2.16}$$

where θ_l is the liquid phase indicator, linearized over ΔT, θ_s is the solid phase change indicator, defined as $\theta_s = 1 - \theta_l$, and α_m is the mass fraction, varying from $-\frac{1}{2}$ in the solid phase to $\frac{1}{2}$ in the liquid phase:

$$\alpha_m = \frac{1}{2}\frac{\theta_l \rho_l - \theta_s \rho_s}{\rho}. \tag{2.17}$$

The phase of the material undergoing phase change is no longer represented by a step function from solid to liquid at the melting interface. Instead, within the mushy zone defined by the interval $2\Delta T$ around the material's melting temperature, T_m, the liquid fraction is assumed to be a linear function of the temperature as shown in Figure 2.5, and according to Equation 2.18.

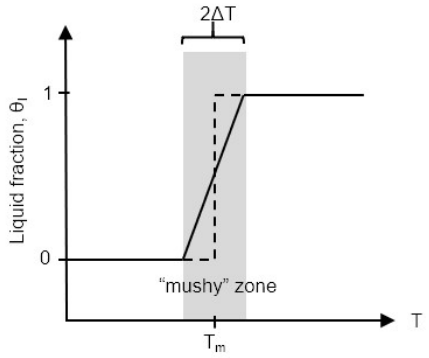

Figure 2.5: Schematic of mushy zone.

$$\theta_l = \begin{cases} 1 & T > T_m + \Delta T, & \text{liquid phase;} \\ \frac{(T - T_m + \Delta T)}{2\Delta T} & T_m - \Delta T < T < T_m + \Delta T, & \text{mushy zone;} \\ 0 & T_m - \Delta T \geq T, & \text{solid phase,} \end{cases} \tag{2.18}$$

Finally, the density is defined in terms of the liquid and solid phase fractions as

$$\rho = \theta_s \rho_s + \theta_l \rho_l. \tag{2.19}$$

Accuracy The accuracy of the apparent heat capacity method depends on the size of the computational time step (Δt), mesh size, and phase change temperature range (ΔT) (Jin et al., 2018; Voller & Cross, 1981). With implicit discretization of the heat equation, the apparent heat capacity from the previous time step is used to compute the temperature at a certain node in the following time step, which leads to calculation

errors whenever a cell undergoes phase change. For example, if the temperature at a node increases from the solid phase to the mushy zone within one time step, the apparent heat capacity from the liquid phase is used to compute the temperature. This leads to an exaggerated temperature increase, since no latent heat is accounted for. For this reason, an exaggerated temperature decrease can be expected when the temperature at a node decreases from liquid to solid. More serious errors occur if the temperature at a node increases from below $T_m + \Delta T$ to above $T_m + \Delta T$ in one time step, in which case the latent heat absorption and associated phase change process is skipped entirely. Jin et al. (2018) found that the magnitude of ΔT relative to the amount of heating applied to the phase change material strongly affects the amount of error, and suggests using a phase change temperature range of at least 5% of the heating temperature for accurate results.

As a general rule of thumb, ΔT should be additionally be chosen to be smaller than the sub-cooling temperature (van Noorden, 2017). If ΔT is chosen too large, it is possible for the mushy zone to cover the entire solid phase, such that the liquid fraction throughout the entire solid phase is greater than zero. This would mean that the full latent heat is not accounted for within the apparent heat capacity term, and would cause accelerated melting, particularly for materials which in reality have a sharp melting front for which the mushy zone is inherently unphysical. In summary, a useful criteria for the phase change temperature range is:

$$0.05(T_m - T_h) \leq \Delta T \leq T_{sub}, \tag{2.20}$$

where, T_h is the heating temperature observed applied to the phase change material, while T_{sub} is the degree to which the frozen solid is sub-cooled below the melting temperature.

For the same reason cited above, Jin et al. (2018) also found that the apparent heat capacity produced inaccurate results for large time steps (> 2s), since large time steps allow a large amount of heat to be transferred. To avoid this, Voller & Cross (1981) recommends that the mesh size and time step be chosen such that at least two nodal temperatures lie within the phase change range at each time step.

2.7.2. Porosity method

A challenge with the apparent heat capacity method is ensuring that the zero velocity condition at the solid/liquid interface is accounted for as regions solidify. A common approach, first described by Brent et al. (1988), is to model cells undergoing phase change as pseudo-porous, with the porosity defined as the element liquid fraction, θ_l. With the porosity approach, the momentum equation includes an additional volume source term, $A\mathbf{u}$, (commonly called the Darcy term), which gradually reduces velocities to zero over the solidification region:

$$\rho \frac{\partial \mathbf{u}}{\partial t} + \rho \mathbf{u} \cdot \nabla \mathbf{u} = -\nabla P + \mu \nabla^2 \mathbf{u} + A\mathbf{u} + S_b, \tag{2.21}$$

where S_b is a buoyancy term which induces natural convection. Assuming the Boussinesq hypothesis to be valid (i.e., density variations can be ignored), S_b is defined as

$$S_b = \rho_l g \beta (T - T_m), \tag{2.22}$$

where T_m is the reference temperature at which β, the thermal expansion coefficient, and ρ_l are evaluated. The effect of A is to force velocities in solid elements close to zero, but to have no effect in liquid elements. In elements that are changing phase, A increases such that it dominates the transient, diffusive, and convective terms in the momentum Equation 2.21. A commonly used form of A is given by equation 2.24. This form was developed specifically for modeling the mushy zone of impure PCM's. In the phase change region, it forces the momentum equations to mimic Carman-Kozeny equations for flow in porous media:

$$\nabla P = \frac{C(1-\theta_l)^2}{\theta_s^3}\mathbf{u}. \tag{2.23}$$

The corresponding form for A is then:

$$A = \frac{C_A(1-\theta_l)^2}{\theta_l^3 + \epsilon}, \tag{2.24}$$

where ϵ is a small computational constant used to avoid division by zero, usually set to $\epsilon = 0.001$ (see for example Brent et al. (1988); Voller & Prakash (1987)). It should be emphasized that Equation 2.24 was developed

with consideration of the morphology of the mushy zone. In materials with a sharp melting front, this volume force becomes a numerical fix and other forms of A may be suitable (Voller & Prakash, 1987). In this thesis the porosity function, B, based on a smoothed delta function, is implemented alongside the traditional Darcy function:

$$B = C_B \tanh(e^2 - 2e^2\theta_l) + C_B. \tag{2.25}$$

In Figure 2.6, the magnitude of both functions is shown as a function of the liquid fraction, θ_l, with the porosity constant, C, chosen such that both functions have the same maximum value ($C_A = 10^5$ and $C_B = 5 \cdot 10^7$). It is obvious that the original porosity function is not symmetric over the melting front. The value of A at the center of the melting front is $2 \cdot 10^5$, while the value of B is much higher at $5 \cdot 10^7$. Effectively, this means that the original porosity function allows flow penetration deeper into the mushy zone than the new function, B.

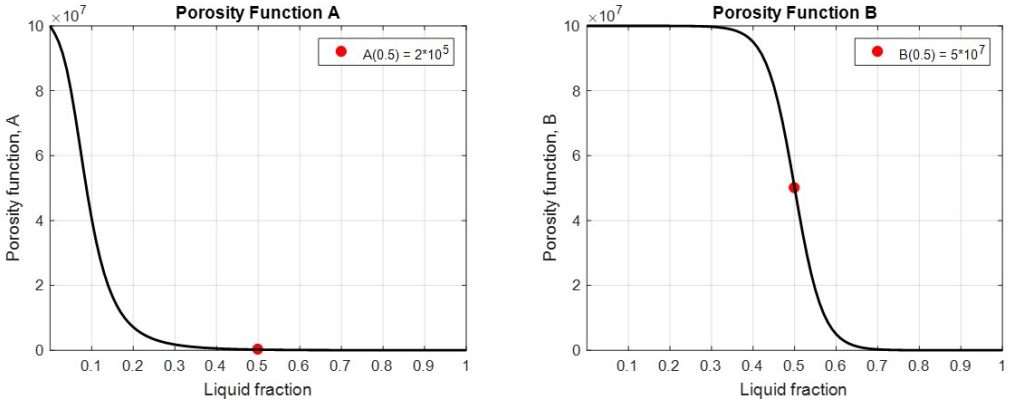

Figure 2.6: Carman-Kozeny porosity function, A (left), and new porosity function, B (right) plotted as function of liquid fraction, θ_l

Choice of porosity constant, C The porosity constant, C, in Equations 2.24 and 2.25 controls the degree of penetration of the convective flow into the mushy phase change region (Brent et al., 1988). Although it is generally agreed that this constant should be chosen to reflect the kinetic processes in the mushy zone, which are different for different materials (Shmueli et al., 2010), no consensus exists for an optimum value. The value of C chosen in most studies for melting with natural convection (based on the standard porosity function, A) lies in the range $10^5 - 10^6$. For example, Jianfeng et al. (2010) used a value of $C = 10^5$ in a study of solidifying molten salt. Brent et al. (1988) used a value of $C = 1.6 \cdot 10^6$ for modeling melting gallium in a square cavity. The same value was used by Binet & Lacroix (1998) for a study of n-Octadecane in a square cavity, though an effort by Hannoun et al. (2003) to determine a reference study for gallium melting in a square cavity uses the much higher value $C = 10^{15}$. Further, Samara et al. (2012) used a value of 10^5 for modeling the melting of aluminum in a vertical cylindrical tube, though the accuracy of this solution relative to experimental findings is not discussed. More recently, Shmueli et al. (2010) considered C values ranging from $10^5 - 10^{10}$ in a study of melting in a vertical cylindrical tube. Comparison with experimental results showed inaccurate, accelerated melt times for $C = 10^5$, with the most accurate results obtained for $C = 10^8$.

Relatively few numerical studies have been performed on melting with forced convection. Among those using the enthalpy-porosity approach, Kumar & Roy (2010) used $C = 1.016 \cdot 10^6$ in a study of the melting of a metal spherical particle exposed to forced convection, while Jianfeng et al. (2010) used a value $C = 10^5$ for studying solidification of a salt in pipe flow.

2.7.3. Advantages and limitations of the enthalpy-porosity method

One of the key advantages of the enthalpy method is that it can be easily applied to large-scale problems with complex melting front shapes (Voller et al., 1990). This makes it generally well-suited for studying the freeze plug. There are, however, also some important limitations to this method. Since the MSFR fuel salt has a eutectic composition, it will have a sharp melting interface, such that the mushy zone in the enthalpy method is inherently unphysical. Moreover, as discussed above, the solutions obtained through the enthalpy method are sensitive to the choice of the porosity constant and phase change temperature range for which the

most suitable values are problem-specific. Finally, the enthalpy method assumes isotropic thermophysical properties in the solid phase, and does not take into account how the different components of the eutectic salt are distributed. In a recent investigation of the microstructure of the fuel salt FliNaK during solidification, Tano et al. (2017) found that the thermal conductivity was highly anisotropic: roughly 8 times higher in the direction of crystal growth than in the perpendicular direction. A numerical method which would take this into account by considering the microstructure of the solid phase is the phase field method. However, this method is excessively resource intensive at the macroscopic scales of the freeze plug and will therefore not be investigated in this thesis.

2.8. Melting with Convection

Heat transfer by forced convection due to mixing of the core flow in the draining pipe will enhance heat transfer to the freeze plug, particularly during transient conditions, and could additionally contribute to erosion of the plug. During the melting process, heat transfer may be enhanced by convection in the event that the plug is melted from the sides.

2.8.1. Forced convection

Heat transfer with forced convection occurs in the presence of fluid motion that is caused by external forces. In Section 2.3, it was established that forced convection will likely have little effect on the freeze plug during the melting process. Effects of forced convection may be more relevant during transient conditions when the velocity in the vicinity of the freeze plug is higher. However, studying these effects lies outside the scope of this thesis.

2.8.2. Natural convection

Natural convection is generated by the temperature difference between the heated surface and the frozen solid, for example between a heated vertical wall adjacent to a frozen solid. The intensity of the natural convection is described by the Rayleigh number, whereas the Prandtl number controls the relative thickness of the momentum and thermal boundary layers:

$$Pr = \frac{C_p \mu}{k_l}; \tag{2.26}$$

$$Ra = \frac{g\beta(T_W - T_m)H^3}{\alpha\nu}, \tag{2.27}$$

where the reference length is chosen as the height of the heated wall, H. Natural convection can be described by three regimes, shown in Figure 2.7:

1. **Conduction regime** The first regime corresponds to short melt times for which conduction is the dominant heat transfer process and the melting front remains parallel to the heated wall. In this regime, the Neumann solution (Equation 2.7) describes the position of the melting front in a rectangular geometry. The dimensionless heat transfer at short times is time dependent, and is described by the Nusselt number as $Nu \approx (\tau)^{-1/2}$ (Kowalewski & Gobin, 2004). Here, τ is the dimensionless time, defined as $\tau = SteFo = \frac{k_l(T_w - T_m)}{\rho_l L_H H^2} t$.

2. **Mixed regime** In the second regime conduction is gradually replaced by convection. This begins in the top of the melt layer when the thermal boundary layer thickness, δ_z is smaller than the width of the melt zone, s, at a given point. The height of the convection region, z, can be described in terms of the Rayleigh number and the dimensionless time, τ, as (Bejan, 2013): $z \approx HRa\tau^2$.

3. **Convection dominated regime** The mixed regime ends when the convection region extends to the bottom of the cavity, that is, $z = H$. This occurs approximately when $\tau \approx Ra^{-1/2}$ (Bejan, 2013). In this regime, natural convection dominates the melt rate, and the Nusselt number at the melting front becomes invariant in time as $Nu \approx Ra^{1/4}$ (Kowalewski & Gobin, 2004).

As shown in Figure 2.7, the effect of natural convection dominated melting is accelerated melting at the top of the front where the flow is directed into the frozen solid, while melting at the base of the front may

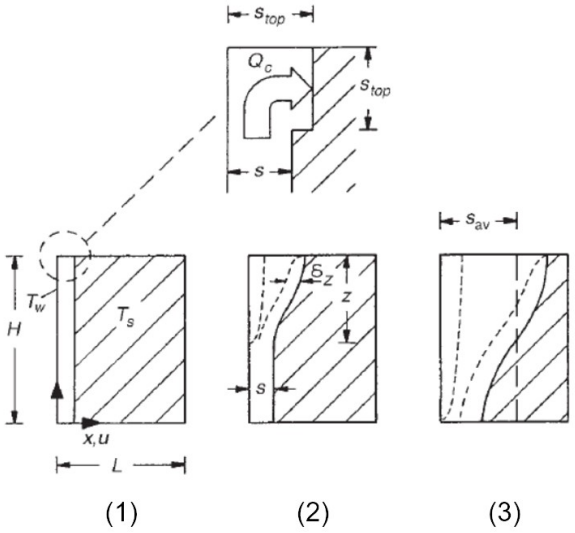

Figure 2.7: Schematic diagram showing three natural convection regimes, including: (1) Conduction regime, (2) mixed regime, and (3) convection dominated regime. Adapted from (Bejan, 2013)

remain unaffected or even suppressed (Sparrow & Broadbent, 1982). In the case of the freeze plug, natural convection is only relevant with regard to melting the sides of the freeze plug. Since the plug is expected to drop as soon as the sides have been melted, however, this effect is not considered relevant for accurate simulations. Nevertheless, the characteristics of natural convection are important to keep in mind, since most reference studies involving phase change in the presence of flow are based on natural convection.

2.9. Close Contact Melting

Close contact melting occurs when a solid is melted from below and stays in close contact with a heat source while it melts. When this occurs, the thin melt layer that is formed between the melting front and heat source is squeezed out by the weight of solid, which is allowed to descend. Since accumulation of liquid between the heated surface and solid is prevented, the melting rate remains approximately constant, and is significantly larger than buoyancy induced melting, where the two surfaces are not in contact, or where movement of the solid is prevented. The increase can be significant. For a block of *n*-Octadecane subjected to a constant temperature from below, Moallemi et al. (1986) found that close contact melting increased the melting rate of the solid sevenfold. More recent literature on contact melting emphasizes its potential for improving the performance of latent heat thermal energy storage systems. For example, Kozak et al. (2014) showed that contact melting increased melt rates by a factor of 2.5 for a PCM in a finned concentric pipe storage geometry.

The principles of contact melting are illustrated in Figure 2.8 for a rectangular solid block. The block descends downward with a sinking velocity, V_s, while it is melting, thereby continuously squeezing out melt fluid. A thin molten layer with thickness δ remains between the melting block and the heated surface at all times.

2.9.1. Analytical models

Almost all analytical models of contact melting assume that the lubrication theory holds in the molten layer, which implies that the thickness of the molten layer, δ is negligible compared to other dimensions in the model, or $\delta << L$. Applying a scaling analysis to the heat equation and momentum equation then indicates that convection in the molten layer is negligible compared to conduction, and the pressure gradient across the molten layer is negligible (see, for example, Bejan (2013)). Assuming body forces in the molten layer are negligible, and that inertial terms in the Navier Stokes equations can be ignored, the governing equations for a standard contact melting problem shown in Figure 2.8 are:

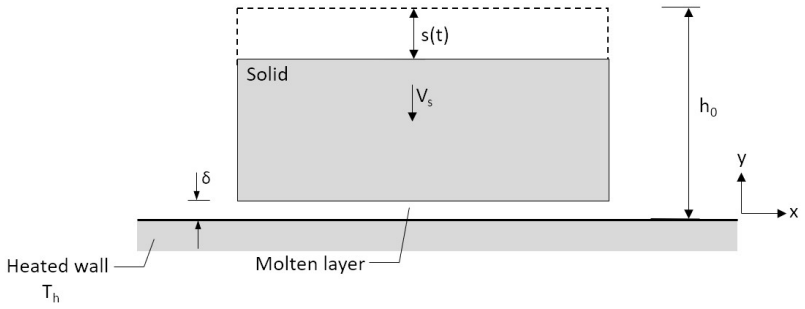

Figure 2.8: Schematic diagram of close contact melting involving a rectangular block on a heated surface. The solid block descends downward with a sinking velocity, V_s, and a thin molten layer with thickness δ remains between the melting block and the heated surface.

$$\frac{\partial^2 T}{\partial y^2} = 0; \tag{2.28}$$

$$\frac{dP}{dx} = \mu \frac{\partial^2 u}{\partial y^2}; \tag{2.29}$$

$$\frac{\partial u}{\partial x} + \frac{\partial v}{\partial y} = 0; \tag{2.30}$$

$$-k_l \left(\frac{\partial T_l}{\partial y}\right)_{y=\delta} = -k_s \left(\frac{\partial T_s}{\partial y}\right) + L_H \rho_s V_s. \tag{2.31}$$

Here, Equations 2.28 and 2.29 are the heat and continuity equations with the lubrication approximation, 2.30 is the continuity equation, and 2.31 is the Stefan condition at the lower melting surface of the solid. Most studies assume that the solid is at the melting temperature, T_m (e.g. Bejan (2013), Bareiss & Beer (1984), Rozenfeld et al. (2015), Kozak et al. (2014)). To avoid the difficulty of solving for the temperature gradient in the solid, the solid temperature gradient in Equation 2.31 may be replaced by an adjustment to the latent heat $L_H \rightarrow L_H + c_s T_{sub}$, reducing the Stefan condition to (Moallemi et al. (1986), Groulx & Lacoix (2006),Myers et al. (2008)):

$$-k_l \left(\frac{\partial T_l}{\partial y}\right)_{y=\delta} = \left(L_H + C_{p_s} T_{sub}\right) \rho_s V_s. \tag{2.32}$$

Analytical solutions have been derived for a range of geometries and boundary conditions. Notably, Bejan (2013) derived a general expression for the sinking velocity of the solid that is transferable to a range of geometries, based on the assumption that melting is quasi-steady (i.e. the thickness of the melting front is invariant for the majority of the melting process), and ignoring the changing mass of the solid during the melting process. Bareiss & Beer (1984) developed one of the first closed form analytical solutions for close contact melting in a horizontal cylindrical pipe based on a force balance in the thin film, again assuming quasi-steady melting. More recently, Kozak et al. (2014) considered close contact melting in a vertical annular enclosure with a non-isothermal base, and developed an analytical expression for the time-dependent melt volume and melt layer thickness based on the heat transfer rate determined in a numeric model. This analytical model was later extended to contact melting in geometries with non-horizontal isothermal heated surfaces by Rozenfeld et al. (2015).

2.9.2. Numerical methods

Because the porosity function suppresses the motion of the solid phase, the enthalpy-porosity approach is not well suited for modeling contact melting. The challenge in modeling close contact melting lies in coupling the sinking solid to the liquid melt surrounding it, while simultaneously capturing phase change. Most efforts to model contact melting have used the enthalpy-porosity approach and accounted for the sinking of the solid by reducing the porosity of the solid (by arbitrarily restricting the size of the porosity constant) such that it settles throughout the simulation. In such approaches, the solid phase is effectively modeled as a slightly deformable liquid, similar to a highly viscous fluid. Both Assis et al. (2007) and Hosseinizadeh

et al. (2013) have applied such approaches in Fluent and achieved reasonable agreement with experiments for close contact melting inside a spherical enclosure. Another method based on a similar principle which has been applied with mixed success is the effective variable viscosity approach, where settling is accomplished by ramping up the viscosity of the solid phase, thus again modeling the solid as a highly viscous fluid (Kasibhatla et al., 2017). Indeed, while these methods appear to reasonably capture the settling of the solid, they generally exaggerate melt rates due to the exaggerated porosity of the solid phase.

Satisfactory numerical methods which combine solid-liquid phase change with solid bulk motion and a full solution of the continuity and momentum equations are still being actively explored. A promising method was recently proposed by Kozak & Ziskind (2017). This method, implemented in Matlab (Mathworks, Natick, MA, USA), robustly couples the sinking solid with the flow in the melt for the basic problem of melting in a rectangular cavity. It couples the apparent heat capacity method with an immersed boundary method, and accounts for the sinking of the solid phase through forcing functions. An alternative approach has been suggested by Faden et al. (2018), in which the solid sinking velocity is again calculated using an immersed boundary method, but then applied through an extended Darcy term in the momentum equation.

3

Method Validation

The following chapter presents several validation studies for modeling solid-liquid phase change using COMSOL. First, Section 3.1 examines the simple case of phase change with conduction, which is implemented using the apparent heat capacity method, and will be used to study the SWATH and decay heat freeze plug designs in Chapters 4 and 5. For the study of the wedge-shaped plug in Chapter 6, both convection and the sinking of the solid must be accounted for. Since coupling of the apparent heat capacity method with convection and close contact melting both present unique numerical challenges, Sections 3.2 and 3.3 will examine these phenomena individually using common reference studies from literature.

3.1. Melting with Conduction

For solid-liquid phase change in 1D with conduction only, melting proceeds with the square root of time, according to the Neumann solution given by Equation 2.7. In the following study, the effect of mesh size, melting temperature range, ΔT, and the computational time step, Δt, on the accuracy of the COMSOL solution are examined.

3.1.1. Validation study design

2D melting by conduction was modeled in COMSOL on a 0.1 x 0.1 m square using the fuel salt LiF-ThF_4 initially frozen with sub-cooling of $T_{sub} = 5K$, as shown in Figure 3.1. A temperature boundary condition of 923 K was applied to the left side of the square, which is equal to the average steady state temperature of the reactor, while the right side was maintained at the sub-cooled temperature $T_f = T_m - T_{sub}$. The top and bottom sides of the square were modeled as adiabatic. The phase dependent properties of LiF-ThF_4 listed in Table 2.1 were used for this simulation. Temperature boundary conditions are summarized in Table 3.1.

Table 3.1: Definitions of temperatures used in the conduction validation study

Parameter	Description	Value
T_m	Melting Temperature [K]	841
T_f	Frozen Temperature [K]	836
T_h	Heated wall temperature [K]	923
$T_h - T_f$	Maximum temperature difference [K]	87

Mesh containing 50 to 400 elements over the height of the square were considered, which corresponds with mesh element lengths ranging from $2 \cdot 10^{-3}$ m to $2.5 \cdot 10^{-4}$ m. Phase change temperature ranges, ΔT, ranging from 5 K to 50 K, or 1 to 10 times the size of the sub-cooling temperature, T_{sub}, were considered to study the importance of choosing ΔT to be less than or equal to the sub-cooling temperature.

3.1.2. Implementation in COMSOL

Melting was implemented in COMSOL using the heat transfer module with a phase change material, which models solid-liquid phase change using the apparent heat capacity method described in Section 2.7. A tetra-

hedral grid was used in all studies in order to allow for the possibility of applying this method to arbitrary geometries.

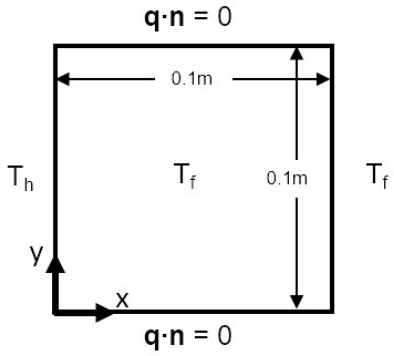

Figure 3.1: Initial conditions and boundary conditions of 2D conduction only COMSOL model

3.1.3. Computation of melting time

In the apparent heat capacity method the phases are described according to the phase indicator, θ_l:

$$\theta_l = \begin{cases} 1, & \text{for liquid phase;} \\ 0, & \text{for solid phase.} \end{cases} \tag{3.1}$$

The center of the melting front is located at $\theta_l = 0.5$, while the region defined by $0 < \theta_l < 1$ captures the width of the macroscopic melting front, commonly known as the mushy zone. In this study, the distance melted at a given time was computed at the centerline ($y = 0.05$ m) by integrating the phase indicator $\theta_l \leq 0.5$ over that line:

$$\text{Distance melted} = \int_0^{0.1} (\theta_l \leq 0.5) \text{dx}. \tag{3.2}$$

3.1.4. Mesh size

A mesh refinement study was conducted to study the sensitivity of the solution on mesh. In Figure 3.2 the analytical and COMSOL solutions are compared with increasing mesh refinement. It is evident that results closely follow the analytical solution for all mesh sizes, and that mesh refinement primarily increases the smoothness of the solution.

The L_2- norm of the error was compared for the different mesh based on the time-dependent position of the melting front

$$\epsilon_{L_2} = \sqrt{\sum_k \left(s_k - s_{ex}(t_k)\right)^2 \Delta t_k} \tag{3.3}$$

where the exact solution, s_{ex} is the Neumann solution (Equation 2.7). Table 3.2 compares the error and computing time for each mesh. Computation effort increases significantly for the finest mesh, and the biggest gains in accuracy are gained by reducing the mesh size from $2 \cdot 10^{-3}$ m to $1 \cdot 10^{-3}$ m. Based on this comparison, a mesh size of $5 \cdot 10^{-4}$ m is preferred for accuracy, although the mesh size of $1 \cdot 10^{-3}$m yields good accuracy for little computational effort. The phase change temperature range, ΔT, was set to 10K in these simulations.

3.1.5. Melting temperature range, ΔT

To study the sensitivity of the solution to the size of the melting temperature range, ΔT, simulations were run for increasting ΔT from 5K to 50K. The results are shown in Figure 3.3.

It is evident that the progression of the melting front is exaggerated for $\Delta T > 10$K. For $\Delta T = 50$ K, the position of the melting front is 28% farther than the analytical solution for the duration of the study. This nicely illustrates the importance of the criteria for ΔT mentioned in Section 2.7.2, which suggest that $\Delta T \leq T_{sub}$. A large ΔT corresponds with a wide mushy zone, and thus a wide region over which the apparent

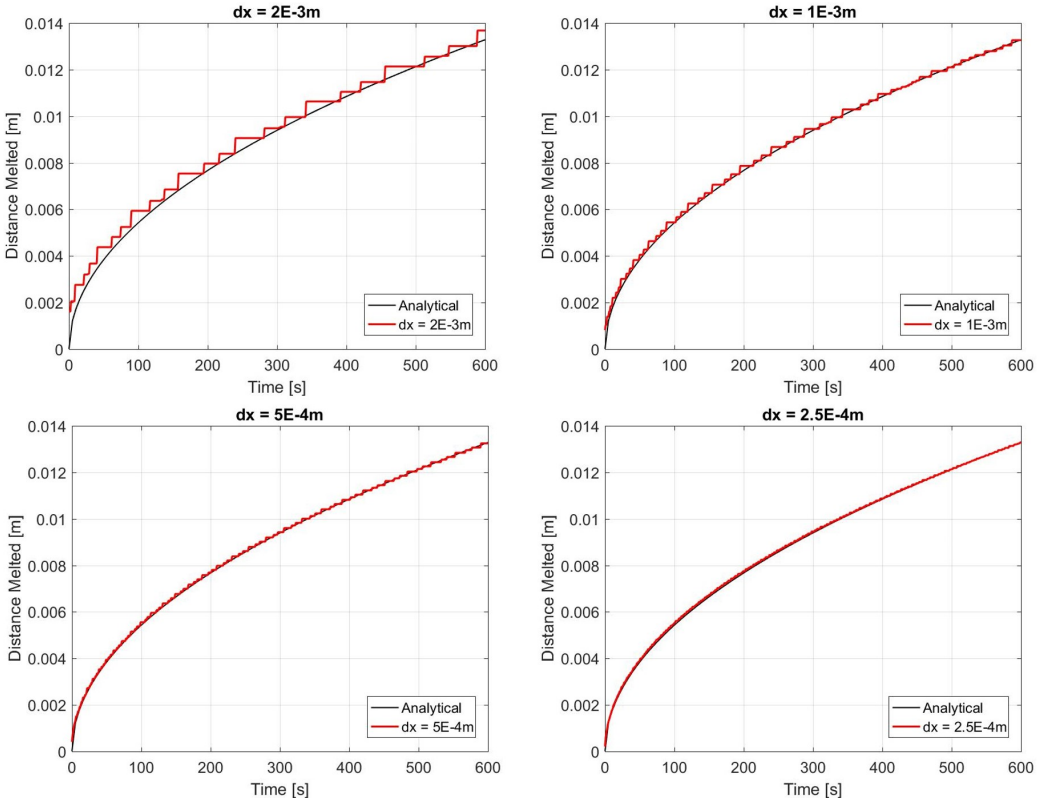

Figure 3.2: Melting distance obtained from COMSOL compared to analytical solution for decreasing mesh element size

Table 3.2: Melting by conduction: comparison of error in melting front position and computational effort for different mesh sizes.

Element length (m)	Elements per side	ϵ_{L_2}	Computing Time (s)
$2 \cdot 10^{-3}$	50	0.0085	78
$1 \cdot 10^{-3}$	100	0.0030	117
$5 \cdot 10^{-4}$	200	0.0016	323
$2.5 \cdot 10^{-4}$	400	0.0015	2077

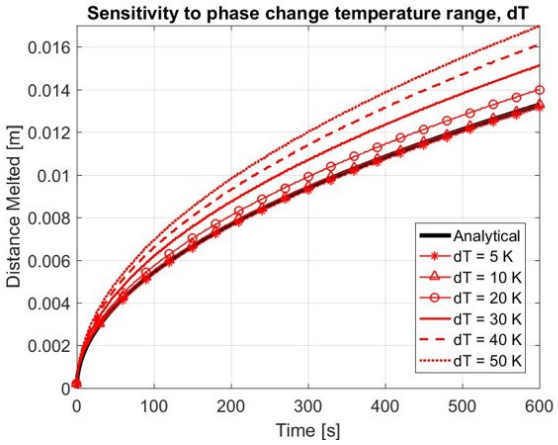

Figure 3.3: Melting distance obtained from COMSOL compared to analytical solution for increasing melting temperature range

heat capacity from Equation 2.16 (containing a contribution from the latent heat) is applied. In this case, accurate results are still obtained for $\Delta T \leq 10$ K because the size of the mushy front does not limit the range

of the liquid fraction in the model. This is supported by Table 3.3, which shows how the deviation from the analytical solution with increasing ΔT corresponds with a decreased range of the liquid fraction, θ_l.

Table 3.3: The deviation of the of melting front position from the analytical solution after 600s for increasing ΔT is correlated with a reduced range in liquid phase fraction, θ_l

ΔT	θ_l range	% Deviation in melting front position
5K	$1 \geq \theta_l \geq 0$	0%
10K	$1 \geq \theta_l \geq 0$	0%
20K	$1 \leq \theta_l \geq 0.10$	5%
30K	$1 \leq \theta_l \geq 0.20$	14%
40K	$1 \geq \theta_l \geq 0.27$	21%
50K	$1 \geq \theta_l \geq 0.31$	28%

In general, ΔT should be chosen to be smaller than T_{sub}. Nevertheless, this study shows that physical solutions are can still be expected as long as $\theta_l \geq 0$ throughout the solid. This is a useful criteria, since it will allow us to assess the accuracy of solutions in which sub-cooling is minimal or inhomogeneous, in which case assigning $\Delta T \leq T_{sub}$ may not be feasible.

3.2. Melting with Convection

The objective of this validation study is to assess the accuracy of COMSOL modeling in the presence of flow, and to assess how various parameters influence the accuracy of results. In Section 2.8, the effect of both forced and natural convection on the freeze plug were discussed. Significant forced convection is only anticipated during the transient operation of the freeze plug, due to mixing in the draining pipe cavity above the freeze plug, and due to the squeezing out of melt fluid in contact melting. On the other hand, natural convection is expected to play an insignificant role in heat transfer during the melting process. Melting with convection is commonly implemented using the Enthalpy-Porosity formulation of the apparent heat capacity method described in Section 2.7. Reference solutions for melting with convection primarily exist for studies of natural convection, among which the case of natural convection in a square cavity with a heated left wall has received the most attention. Reference solutions have been found for this case study for both high Prandtl materials such as *n*-Octadecane, (Pr = 50, Bertrand et al. (1999)) and low Prandtl number materials such as Tin and Gallium, (Pr = 0.01, 0.025, Bertrand et al. (1999); Brent et al. (1988); Hannoun et al. (2005); Viswanath & Jaluria (1993)). High Prandtl compounds are defined as having a Prandtl number greater than one, such that melting is quickly dominated by natural convection (Bertrand et al., 1999). Since LiF-ThF_4 has a Prandlt number of 6.67, the case studies using *n*-Octadecane are the most applicable for validation purposes.

3.2.1. Validation study design

The reference solution from Bertrand et al. (1999) of melting *n*-Octadecane in a square cavity that is heated from the left side was replicated in COMSOL. The dimensions and boundary conditions are the same as those used for melting with conduction (Section 3.1), shown in Figure 3.1. The temperatures and material used in this study are listed in Table 3.4. The parameters of interest are those which are known to affect the accuracy of the enthalpy-porosity method (see discussion in Section 2.7), including

1. Mesh element length, Δx;
2. Size of phase change temperature range, ΔT;
3. Size of the porosity constant, C_A and C_B; and
4. Choice of porosity function A or B.

The meshes considered range from 250 to 550 mesh elements over the height of the square, which corresponds with a maximum mesh element side length of $4.0 \cdot 10^{-4}$ m and a minimum length of $1.8 \cdot 10^{-4}$ m. Since the number of mesh elements used in the reference solutions compiled in Bertrand et al. (1999) are not reported, this range was selected based on recommendations by Hannoun et al. (2005), who developed a reference solution for melting tin. The phase change temperature range, ΔT, was varied from 1 K to 5 K, representing a range from 1/2 to 2.5 the size of T_{sub}. Porosity functions A and B were compared, and simulations were first run with increasing porosity constants until the models no-longer achieved convergence.

Table 3.4: *n*-Octadecane Material Properties from Bertrand et al. (1999)

Property	Units	*n*-Octadecane[(a)]
Thermal Conductivity (λ)	$W{\cdot}m^{-1}K^{-1}$	0.2
Density (ρ)	$kg{\cdot}m^{-3}$	800
Heat Capacity (C_p)	$J{\cdot}kg^{-1}K^{-1}$	1250
Kinematic Viscosity (ν)	$m^{\cdot 2}s^{-1}$	10^{-5}
Latent Heat (L)	$J{\cdot}kg^{-1}$	$1.25\cdot10^5$
Melting Temperature (T_m)	K	303
Sub-cooling (T_{sub})	K	2
Heated wall temperature (T_h)	K	313

(a) Properties assumed to be identical in solid and liquid phases.

For porosity function A the values $C_A = 10^3, 10^4$ and 10^5 were compared, while for the porosity function B the values $C_B = 5\cdot10^5, 5\cdot10^6$ and $5\cdot10^7$ were compared.

3.2.2. Implementation in COMSOL

A tetrahedral grid was used in all studies since it is more suitable for the complex geometries involved in the freeze plug study. Melting was implemented in COMSOL using the heat transfer module with a phase change material. The non-isothermal flow module was used to couple the heat transfer and flow modules. Bouyancy effects due to temperature variations were accounted for through a volume force based on the Boussinesq approximation.

The no penetration condition was accounted for through the enthalpy-porosity formulation described in Section 2.7, in which the addition of a volume force, $A\mathbf{u}$ or $B\mathbf{u}$ (depending on the choice of porosity function) in the momentum equation drives the velocity to zero in the solid phase. Both the original porosity function, A (Equation 2.24) and the new porosity function, B (Equation 2.25) were studied. The location of the melting front is defined as in Section 3.1.2. More detailed COMSOL solver settings used here and in subsequent sections are summarized in Appendix D.

3.2.3. Sensitivity to porosity constant, C and choice of porosity function

As discussed in Section 2.7.2, higher porosity constants have been shown to yield more accurate results with the enthalpy-porosity method. For this reason, an effort was made to set the porosity constant as high as possible. Originally, attempts were made to use a porosity constant greater than 10^5 with the traditional porosity function, A, based on these recommendations. However, no convergence could be achieved with such high constants. The highest porosity constant for which convergence could be achieved with function A is $C_A = 10^5$, and $C_B = 5\cdot10^7$ for function B. As was shown in Figure 2.6, these constants correspond with the same maximum value of the porosity function of 10^8 (observed in the solid phase).

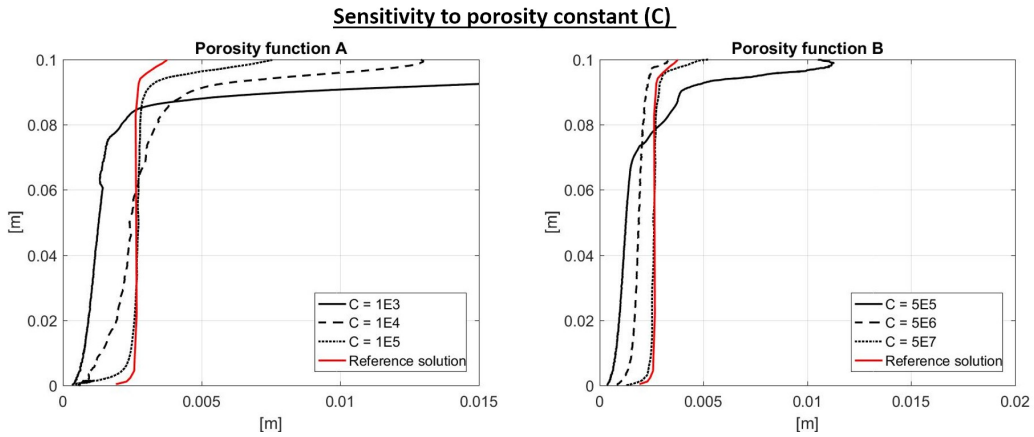

Figure 3.4: Melting front shape after 250 s for increasing porosity constants using porosity function A (left) and B (right). Reference solutions from Bertrand et al. (1999).

Figure 3.4 shows the shape of the melting front obtained in COMSOL after 250 s of melting for increasing values of C, compared with the reference solution in Bertrand et al. (1999). A melting temperature range of 2.5 K and mesh element length of $2.2 \cdot 10^{-4}$ m were used in both models. It is clearly evident that low values of C exaggerate the effects of natural convection, enhancing melting at the top of the cavity where the convective flow is directed into the melting front, and suppressing melting at the bottom of the cavity where the convective flow is directed away from the melting front. The porosity constant clearly controls the degree to which flow penetrates the mushy zone, and, as expected, the most accurate results are obtained with the highest constants. The results obtained from function B are more accurate than those obtained from function A for the same reason. Since function B resembles a smoothed step function over the center of the mushy region, defined by $\theta_l = 0.5$, it allows less penetration into the mushy zone than the function A, which peaks around $\theta_l = 0.1$.

Based on these results, it can be recommended to use porosity function B with $C_B = 5 \cdot 10^7$ for future COMSOL studies involving the melting with convection.

3.2.4. Sensitivity to mesh size

The sensitivity of the results to mesh size was studied by comparing the shape of the melting front obtained in COMSOL with the reference solutions in Bertrand et al. (1999) after 250 s of melting for decreasing mesh element size. The results of this study are shown in Figure 3.5, for both porosity functions A and B. Unless otherwise noted, a melting temperature range of 2.5 K and time step of 0.01s were used, and the porosity functions were set at their maximum values ($C_A = 10^5$, and $C_B = 5 \cdot 10^7$).

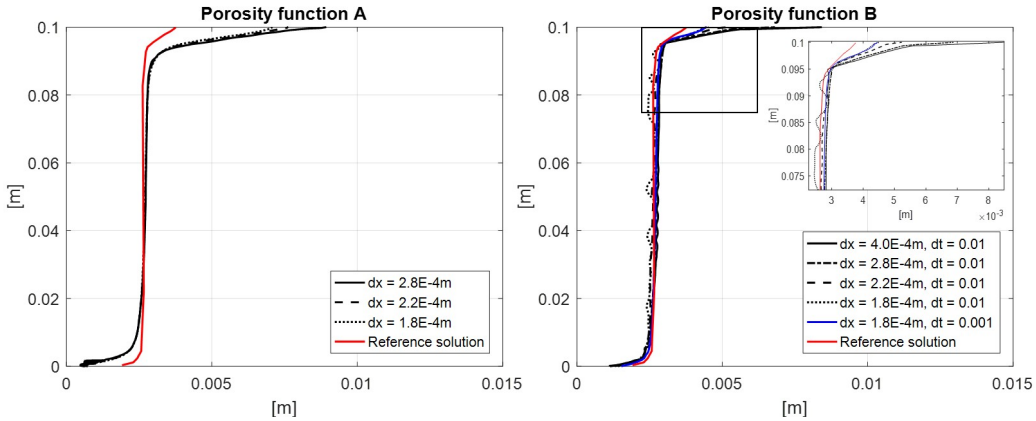

Figure 3.5: Melting front shape after 250s for increasing mesh element length using porosity function A (left) and B (right). Reference solutions from Bertrand et al. (1999).

The accuracy of the melting results appears to improve minimally with mesh refinement. The greatest difference is observed at the top of the melting front, where the highest velocities occur, suggesting that localized mesh refinements in high-velocity regions may be desirable. Table 3.5 lists the computing times required for each mesh, and shows that the mesh with 450 elements is the most efficient. The coarsest mesh with 250 elements per side required more than ten times longer to run for porosity function B than the mesh with 450 elements per side, and did not converge for porosity function A, likely because the high temperature gradient within at the melting front was not resolved sufficiently. On the other hand, instabilities begin to appear in the melting front for the finest mesh for porosity function B, as evident by the irregular melting front over the height of the cavity. These instabilities are likely the result of the melting front moving too far in a given time step relative to the mesh size, and are eliminated by using a smaller time step of 0.001 s.

Table 3.5: Melting with natural convection: comparison of computational effort for different mesh sizes using porosity function B.

Max. element length (m)	Elements per side	Computing Time (s)
$4.0 \cdot 10^{-4}$	250	168226
$2.8 \cdot 10^{-4}$	350	19520
$2.2 \cdot 10^{-4}$	450	17886
$1.8 \cdot 10^{-4}$	550	30949

3.2.5. Sensitivity to phase change temperature range, ΔT

The sensitivity of results to the phase change temperature range, ΔT, are shown in Figure 3.6. While the results appear to improve with a smaller ΔT, the improvement is not as significant as that observed previously in Section 3.1.5, despite the fact that the range of ΔT represents a similar fraction of the total temperature difference in the model. The reason for this is that the full range of the liquid fraction remains accounted for in the solid phase for all values of ΔT, i.e. the minimum liquid fraction for $\Delta T = 1$ K and $\Delta T = 2.5$ K is zero, while for $\Delta T = 5$, $1 \geq \theta_l \geq 0.003$. Some irregularities can be seen in the melting front with $\Delta T = 1$ K, likely because the mesh is too coarse for such a narrow mushy region, moreover, convergence was not achieved for smaller ΔT on the same mesh.

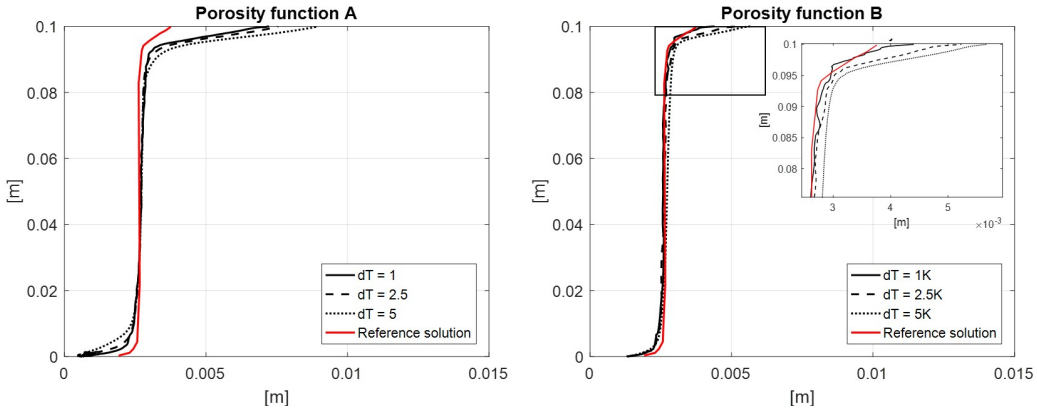

Figure 3.6: Melting front shape after 250s for increasing phase change temperature range, ΔT, using porosity function A (left) and B (right). Reference solutions from Bertrand et al. (1999).

3.2.6. Longer melting times

Due to long computation times, the previous studies were only run for 250 s when the effect of natural convection on the melting front is still minimal. To see whether the accurate results achieved at 250 s also hold at longer times when the convection effects on the melting front are more pronounced, studies were run with porosity function B, ($C_B = 5 \cdot 10^7$) for 1000 s. Figure 3.7 shows COMSOL results for $\Delta T = 1$ K and 2.5 K compared with reference solutions in Bertrand et al. (1999). A range of reference solutions is shown to reflect that these do not precisely agree on the melting front at the top of the cavity. Both results follow the reference solutions nicely, but similarly diverge a the top of the cavity. As expected, the thickness of the mushy zone has the greatest affect on results when the flow is directed into the melting front.

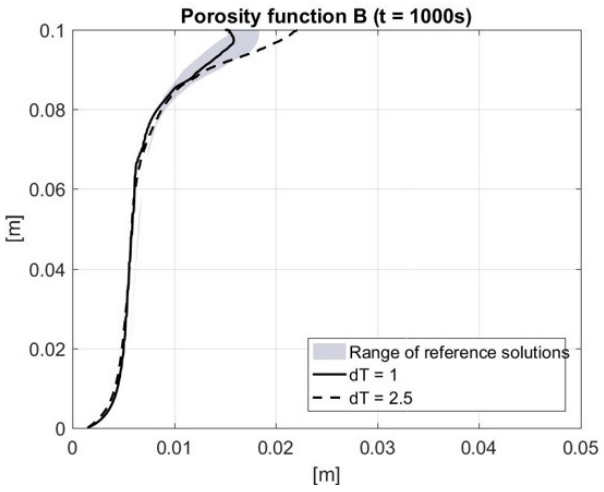

Figure 3.7: Melting front shape after 1000 s of melting for phase change temperature range, ΔT of 1 and 2.5 K using porosity function B. Range of reference solutions adapted from Bertrand et al. (1999).

3.2.7. Discussion

The simulations of melting with natural convection show that in combination with strict solver tolerances, good agreement with literature results was obtained with the porosity function B, and $C_B = 5 \cdot 10^7$. The width of the phase change region and mesh size were found to be comparatively less important for the accuracy of the solution, although convergence was improved by a sufficiently fine mesh.

For materials with sharp melting interfaces, most studies seek to minimize the size of the artificial mushy zone introduced by the enthalpy-porosity method as much as possible. However, a very small ΔT requires additional mesh refinement, requiring a smaller computational time step and increasing computational effort. Indeed, a similar reference study on melting Gallium with natural convection reports simulations of up to 3 months using $\Delta T = 0.025$ with 400 - 600 mesh elements per side. For the purposes of this study, it is valuable to know that reasonable accuracy can be obtained with substantially larger ΔT.

3.3. Close Contact Melting

As mentioned in Section 2.9, modeling close contact melting numerically is still a problem under investigation. The more promising approaches, which use an immersed boundary method and determine the sinking velocity through a force balance around the solid, unfortunately cannot be implemented in COMSOL. In the following section, a semi-analytical approach is described and validated against the analytical and experimental results from Bareiss & Beer (1984). The purpose of this study is to verify that this approach accurately models contact melting in COMSOL for simple geometries for which the sinking velocity and molten layer thickness can be estimated analytically. This methodology will then be applied to the problem of the wedge shaped plug in Chapter 6.

3.3.1. Description of the reference problem

The reference problem chosen to test this approach in COMSOL involves contact melting of *n*-Octadecane in a heated horizontal cylinder. Melting results are compared to the analytical solution from (Bareiss & Beer, 1984) which has been shown to agree well with experimental findings (Bareiss & Beer, 1984; Sparrow & Geiger, 1986). A schematic of the melting problem is provided in Figure 3.8. The initial solid temperature, including sub-cooling, is given by $T_m - T_{sub}$. The solid sinks with velocity V_s due to melting at the bottom, while the distance s_0 describes the downward movement of the top melting front due to the combined effects of sinking and melting at this front. A thin molten layer with thickness δ forms between the solid and the pipe. The point x_p describes a point on the melting front at which the sinking velocity (Equation 3.5) is prescribed.

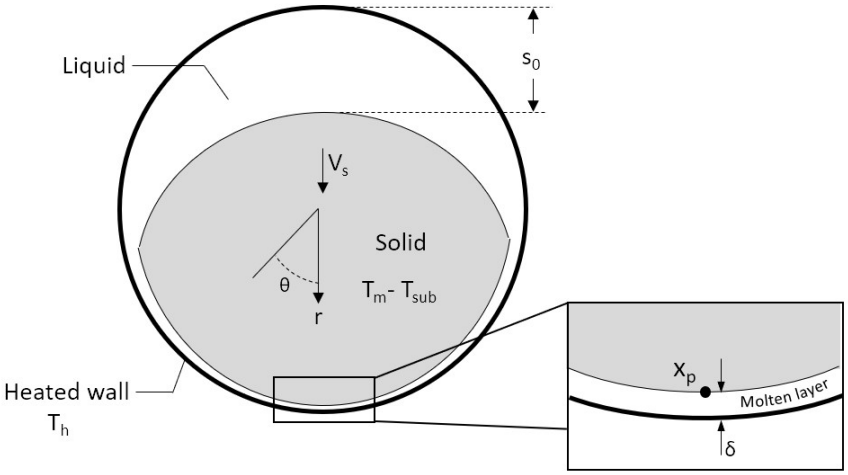

Figure 3.8: Schematic of contact melting inside a horizontal cylinder heated from all sides with temperature T_h.

3.3.2. Implementation of contact melting in COMSOL

The challenge with modeling close contact melting is accounting for the sinking of the solid phase as it is being melted. One way of doing this is to prescribe the solid velocity through an extended Darcy term approach (see Faden et al. (2018); Kozak & Ziskind (2017), among others). The Darcy term in the momentum equation then becomes

$$A(\mathbf{u}-\mathbf{u_s}), \tag{3.4}$$

where A is the porosity function, and $\mathbf{u_s}$ is the sinking velocity of the solid. In liquid cells ($\theta_l = 1$) the Darcy term has no effect, while in solid cells ($\theta_l = 0$) the sinking velocity is prescribed. In the mushy zone ($0 < \theta_l < 1$), the Darcy term suppresses flow according to either the porosity function A or B. Generally, the sinking velocity is assumed to only have a vertical component, V_s.

In this thesis, a semi-analytical method is proposed for prescribing the solid sinking velocity. This approach fixes the position of the contact melting front at the estimated thickness of the molten film layer, which is assumed to stay constant throughout the melting process. The sinking velocity is defined as proportional to the difference between the temperature at a fixed point on the melting front, x_p, and the the melting temperature, T_m:

$$V_s = -c\Big(T(x_p) - T_m\Big), \quad \text{for} \quad T(x_p) > T_m, \tag{3.5}$$

where, c is a proportionality constant. One might expect that if c is chosen to be too large, the melting interface might advance beyond x_p in a given time step. This might lead to an oscillating sinking velocity, or cause convergence problems in the event that the solid is asked to move beyond the domain. On the other hand if c is chosen too small, the solid will melt more quickly than it sinks, and the thickness of the molten layer will increase with time. To implement this method, the thickness of the film layer is first estimated *a priori* through a simple analytical description of the contact melting process.

3.3.3. Geometry and boundary conditions

A horizontal pipe with a radius of 0.02m was modeled. The walls were heated 20K above the melting temperature, while the solid was sub-cooled at 5K below the melting temperature. Following the recommendations from Section 3.2, a phase change temperature range of ΔT = 5K is used, which is equivalent to T_{sub}. Distinct material properties are assigned to the solid and liquid phases, which are assumed to be temperature independent. The material properties are listed in Table 3.6, along with relevant boundary conditions and dimensions.

Table 3.6: Octadecane Material Properties and study parameters from Hosseinizadeh et al. (2013)

		***n*-Octadecane**	
Property	**Units**	**Solid**	**Liquid**
Thermal Conductivity (λ)	$W{\cdot}m^{-1}K^{-1}$	0.35	0.149
Density (ρ)	$kg{\cdot}m^{-3}$	865	770
Heat Capacity (C_p)	$J{\cdot}kg^{-1}K^{-1}$	1990	2660
Kinematic Viscosity (ν)	$m{\cdot}^2s^{-1}$	-	10^{-5}
Latent Heat (L_H)	$J{\cdot}kg^{-1}$	$2.41 \cdot 10^5$	
Melting Temperature (T_m)	K	301	
Sub-cooling (T_{sub})	K	5	
Heated wall temperature (T_h)	K	321	
Porosity Constant (C)	-	$C_A = 10^5$, $C_B = 5 \cdot 10^7$	
Pipe Radius (R)	m	0.02	

Phase change was implemented in COMSOL in the same way as for the preceding case study for melting with natural convection (Section 3.2). Both porosity functions A and B were considered, with the porosity constants set to $C_A = 10^5$ and $C_B = 5 \cdot 10^7$, respectively. A mesh refinement study was conducted, and the effect of the proportionality constant, c, was studied.

3.3.4. Analytical solution

A relationship between the molten layer thickness and the sinking velocity can be derived by applying the Stefan condition (Equation 2.32) to the cylindrical geometry at the lower melting front, and adjusting the latent heat to account for sub-cooling.

$$-k_l \frac{T_h - T_m}{\delta(\theta)} = \Big(L_H + c_s T_{sub}\Big)\rho_s V_s cos(\theta), \tag{3.6}$$

$$\delta(\theta) = \frac{k_l \Delta T}{\rho_s \Big(L_H + c_s T_{sub}\Big) V_s cos(\theta)}. \tag{3.7}$$

Experiments by Bareiss & Beer (1984) showed that the total melting velocity of the solid was nearly uniform from the onset of melting, $t = 0$, to the time when the entire solid was melted, $t = t_f$. Two effects contribute to the melting velocity: the sinking of the solid with velocity, V_s, due to melting at the bottom, and melting of the top surface. The total distance moved by the top of the solid due to both of these effects is given by s_0 in Figure 3.8. The melting speed for the horizontal cylinder can thus be represented as

$$\frac{ds_0}{dt} \approx \frac{D}{t_f}, \tag{3.8}$$

where, D is the diameter of the cylinder. Sparrow & Geiger (1986) found that the rate of melting of the lower surface represents 88% − 94% of the total melting in a horizontal cylinder. Thus, the total melting velocity is approximately equivalent to the sinking velocity

$$V_s \approx \frac{D}{t_f}. \tag{3.9}$$

The time needed to melt the entire solid can be approximated by the dimensionless expression (Bareiss & Beer, 1984)

$$\frac{\alpha t_f}{R^2} = 2.49\left(\frac{\rho_l}{\rho_s} St\right)^{-3/4} (Pr\,Ar)^{-1/4}(1 + C)^{-1}, \tag{3.10}$$

where Ar is the Archimedes number defined by

$$\mathrm{Ar} = \left(1 - \frac{\rho_l}{\rho_s}\right)\frac{gR^3}{\nu^2}. \tag{3.11}$$

Additionally, C is an empirical correction that accounts for (relatively minor) additional melting due to natural convection on the top surface of the solid:

$$C = 0.25\left(\frac{\rho_l}{\rho_s} St \frac{Ra}{Pr\,Ar}\right)^{1/4}. \tag{3.12}$$

It follows that the estimated melting time for this case study is 510 s. From Equations 3.9 and 3.7 the sinking velocity must then be approximately $7.7 \cdot 10^{-4}$ m/s, while the molten layer thickness is approximately $\delta = 1.73 \cdot 10^{-4}$ m.

3.3.5. Meshing

A mixed mesh was used with quadrilateral boundary layer elements in the lower half of the cylinder in the region of the thin molten melt layer. Thin boundary layer elements were chosen in order to resolve the melting front, which maintains a large temperature gradient when it remains adjacent to the hot wall, and to resolve the flow in this melt layer. This region was taken to be three times the expected thickness of the molten layer. Elsewhere in the cylinder (including near the top boundary), a courser triangular mesh was used to ensure that the melting front does not skip over mesh elements while sinking.

A mesh sensitivity study was performed on both the boundary layer mesh and interior mesh. The number of elements spanning with width of the boundary layer was varied from 6 to 24, while the maximum element size of the triangular mesh was varied from $5.0 \cdot 10^{-4}$ to $1.6 \cdot 10^{-4}$ m (equivalent to the coarsest and finest mesh considered in previous studies). The proportionality constant was taken to be $c = 10^{-5}$, and the reference point, x_p, was located a distance $\delta = 7.3 \cdot 10^{-4}$ m from the bottom of the cylinder. Figure 3.9 shows the non-dimensional progression of the top melting front as a function of the non-dimensional time for the different meshes. The melting follows the uniform behavior predicted by Bareiss & Beer (1984). The solution does not vary with refinement of the interior mesh, and shows only a very mild deviation when for the coarsest boundary layer mesh. Based on these results, it was decided to proceed using 12 boundary layer elements and the coarsest interior mesh.

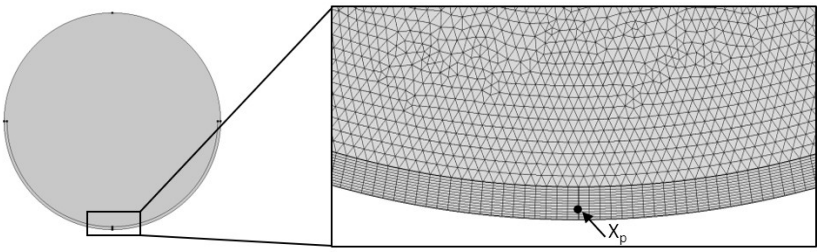

Figure 3.9: Meshing for close contact melting in a horizontal cylinder, showing boundary layer mesh near the melting front and triangular mesh elsewhere.

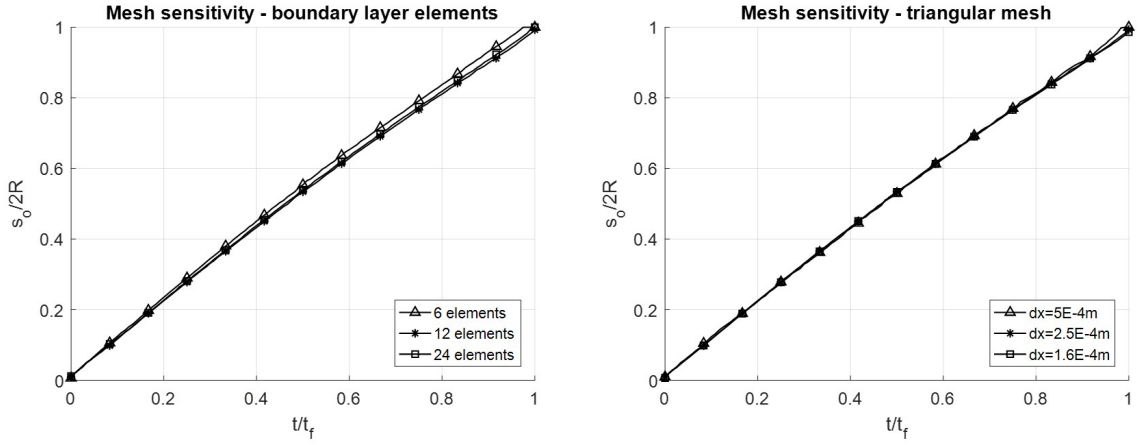

Figure 3.10: Shift in top melting front of sphere as a function of the dimensionless time for increasing number of boundary layer mesh element (left) and triangular elements (right); $c = 1 \cdot 10^{-5}$, $t_f = 600$ s.

3.3.6. Effect of proportionality constant, c

The appropriate value of the proportionality constant depends on the melting speed, and the thickness of the molten layer. In this study, values of c from 10^{-6} to $5 \cdot 10^{-5}$ were tested to approximate the most appropriate value. This range was selected based on the assumption that the sinking velocity should be approximately $7.7 \cdot 10^{-5}$ m/s. Considering the temperature difference of 20 K between the melting front and hot wall, it is clear that $c > 4 \cdot 10^{-6}$, and smaller values should cause the solid to sink more slowly than it is being melted, resulting in an increased liquid film thickness, δ.

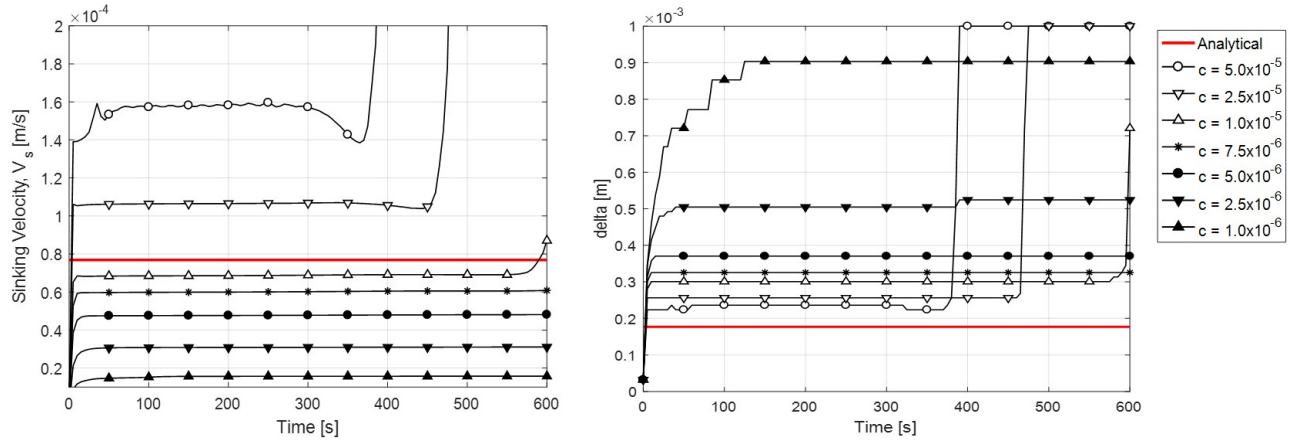

Figure 3.11: Sinking velocity (left) and molten layer thickness (right) as a function of time for increasing values of the porosity constant, c, and compared to the analytical solution from Bareiss & Beer (1984).

Figure 3.11 shows both the sinking velocity, V_s, and molten layer thickness, δ as a function of time for all

proportionality constants considered. For the largest value ($c = 5{\cdot}10^{-5}$), the sinking velocity appears unstable. For all smaller values, the velocity reaches a steady state after an initial increase. The asymptotic behavior shown for $c = 5 \cdot 10^{-5}$ and $c = 2.5 \cdot 10^{-5}$ corresponds with full melting, and appear disproportionately sensitive to c compared to the rest, suggesting that these are too large for the position x_p chosen. Figure 3.11 also shows that choosing to locate x_p on the melting front means that the melting front will reach a steady state position some distance further away. As expected, the observed δ increases with decreasing c, and is particularly exaggerated for the lowest values ($c = 2.5 \cdot 10^{-6}$ and $c = 1.0{\cdot}^{-6}$), suggesting, as predicted, that these are too small for the position of x_p chosen. This analysis indicates that an appropriate value for c is between $5 \cdot 10^{-6}$ and $1 \cdot 10^{-5}$. However, since δ exceeds the analytical estimate for these (indeed, all) values of c, the corresponding melting times are lower than the analytical estimate.

This is illustrated in Figure 3.12, which shows the shift in the top melting front as a function of the dimensionless time for different values of c. The melting time is comparable to the analytical estimate when $c = 2.5 \cdot 10^{-5}$. For this value, a high sinking velocity appears to compensate a molten layer which is 25% too large.

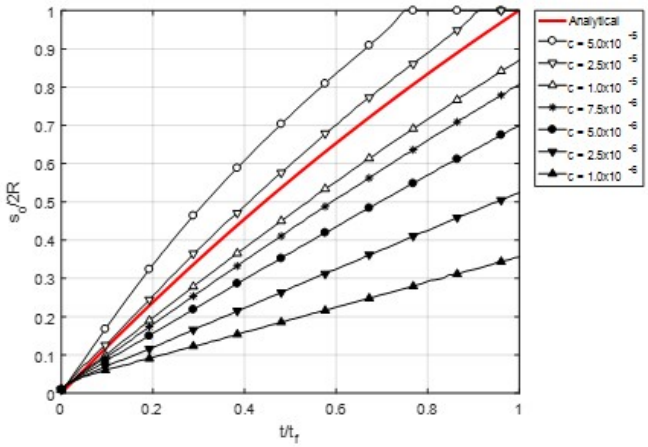

Figure 3.12: Shift in top melting front of sphere as a function of the dimensionless time for increasing number of boundary layer elements (left), and interior triangular elements (right).

Figure 3.13 shows the melting progression at 100 s, 200 s, 300 s, and 400 s for $c = 2.5 \cdot 10^{-5}$. These images show that the shape of the melting front is nicely maintained throughout the melting process and is consistent with the experimental results from Bareiss & Beer (1984).

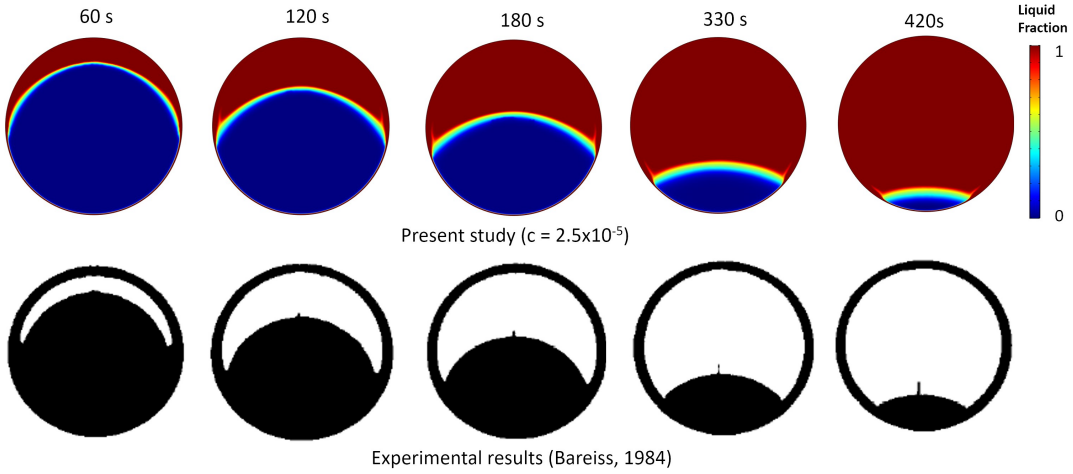

Figure 3.13: Top: Melting progression for close contact melting in a vertical cylinder for $c = 2.5 \cdot 10^{-5}$. Bottom: Experimental results from Bareiss & Beer (1984).

Figure 3.14 shows the steady-state lower melting front location for $c = 2.5 \cdot 10^{-5}$ imposed on the mesh and

flow field, showing that the lower melting front remains smooth throughout the melting process, and the flow field in the molten layer is well-resolved.

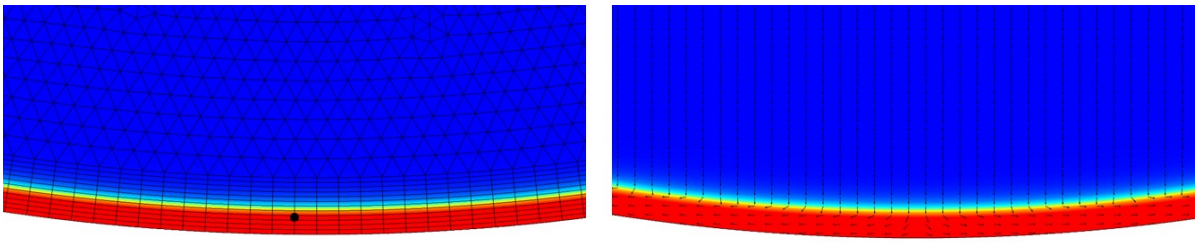

Figure 3.14: Steady-state position of lower melting front with meshing (left) and normalized velocity flow vector field (right) for $c = 2.5 \cdot 10^{-5}$. Blue corresponds with solid phase, and red with liquid.

3.3.7. Discussion

This simulation relied on predefining the location of the melting front, δ, from an analytical description of the problem. The melting front is then effectively fixed at this location through a sinking velocity defined to be proportional to the temperature of a reference point at this location. It was found that choosing the reference point at the melting front leads to a steady-state molten layer thickness greater than the analytical estimate. As a result, the proportionality constant, c, which produced the most accurate melting time did not have the same molten layer thickness or sinking velocity as the reference solution. It follows that this analysis should be repeated with x_p located mid-way between the expected melting front location and heated wall.

Despite this shortcoming, the melting behavior observed is consistent with the experimental and analytical results from Bareiss & Beer (1984) when the appropriate proportionality constant is chosen. In particular, the shape of the partially melted cylinder matches what has been reported in experiments by both Bareiss & Beer (1984) and Moallemi et al. (1986). Figure 3.15 shows the melting progression for *n*-Octadecane in a heated sphere using a new immersed-boundary method approach (Gudibande & Iyer, 2017) along with less accurate results obtained with a relaxed porosity constant approach in Fluent (Hosseinizadeh et al., 2013). The present method of 'fixing' the location of the solid according to a known analytical solution produces more realistic melting results than methods previously applied in commercial software in which a small porosity constant must be used to achieve the sinking behavior.

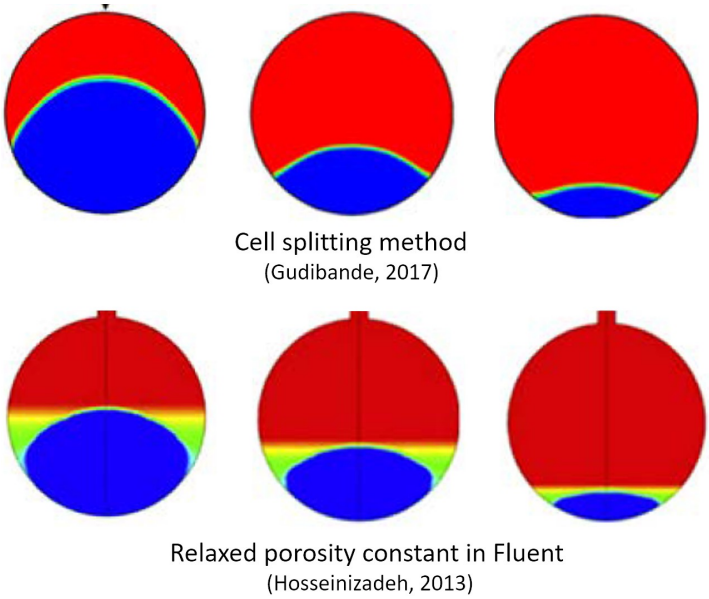

Figure 3.15: Comparison of the melting results for *n*-Octadecane in a heated sphere by Gudibande & Iyer (2017), who used a cell-splitting method with good agreement with experiments and Hosseinizadeh et al. (2013), who used a relaxed porosity method in Fluent, with less realistic results.

It should be emphasized that, unlike immersed-boundary like methods, the present approach is not generalizable. Reliance on a geometry-specific analytical solution restricts the applicability of this approach to simple geometries for which analytical solutions exist. Moreover, as implemented above, this approach is only appropriate for melting problems in which the molten layer thickness is quasi-steady, and cannot easily be generalized to non-isothermal melting problems or problems in which the force acting on the molten layer changes throughout the melting process.

4

Study of SWATH Plug Design

The following chapter presents a COMSOL study of the freeze plug design proposed in the SWATH experiments. This design is modeled at both the proposed experimental scale described in Ghetta et al. (2017b) and a larger scale consistent with the realistic dimensions of the MSFR. The performance of this design is evaluated for different freeze plug designs, different initial temperatures of the freeze plugs, and different salt compositions. The goal of this study is to determine which parameters have the greatest affect on the melt times of the freeze plug and to make design recommendations.

4.1. SWATH Freeze Plug Description

The defining characteristic of the SWATH freeze plug design is that its performance does not depend on the transfer of decay heat from the reactor core to the plug itself. This is in contrast to previous designs considered within SAMOFAR (e.g., Swaroop (2016)), which relied exclusively on the decay heat to melt. The operating principle of the SWATH design is to melt the freeze plug using heat stored in steel blocks adjacent to the draining pipe (Figure 4.1). This is advantageous, because the performance of the freeze plug no longer depends on detailed knowledge of the thermohydraulics of the MSFR core during accident scenarios, or the efficiency of decay heat transfer to the plug itself. Consequently, the freeze plug can be designed and optimized independent of the reactor, and can be located some distance away from the reactor core, where it is less exposed to temperature and velocity fluctuations that may undermine the plug's stability during transient operations.

Another important difference between the two designs lies in the direction of heat transfer to the plug. As illustrated in Figure 4.1, the dominant heat transfer mode to the plug is through the plug sides via the steel mass around the draining pipe. This is in contrast with the decay heat design, where both the heat transfer through the fluid in the draining pipe above the plug, and through the sides of the plug via the draining pipe, play an important role. Previous studies considering a design with multiple freeze plugs are based on heat transfer primarily through the top of the plug (e.g., see those mentioned in Section 1.2.2). Therefore, the design suggestions from these studies can not be directly transferred to the SWATH design.

4.2. Study Design

First, the SWATH design was modeled in COMSOL at approximately 1/4 the realistic reactor scale. This scale, henceforth referred to as the 'experimental scale', matches the scale of the model that is studied under the SWATH experiments described in Ghetta et al. (2017b). The SWATH design is also modeled at a realistic scale, hereafter referred to as the 'reactor scale', in order to make a broader assessment of its feasibility as an alternative freeze plug design. Since experimental work on the SWATH design will be conducted using LiF-NaF-KF ('FliNaK'), this salt is used for the experimental scale simulations. At the reactor scale, a more realistic fuel composition, LiF-ThF_4, is also considered.

Parameters that were studied are summarized in Table 4.1. A design consisting of one plug with the same diameter as the draining pipe was considered, as well as designs featuring a metal grate with multiple plugs. This design was studied for a grate containing four and seven plugs, in order to see how having a central plug (as with the 7-plug design) affects melting times. Plug aspect ratios of 0.5, 1.0, and 1.5 were considered to assess the effect of using an aspect ratio greater or less than one. P/D ratios ranging from 1.05 to 2.0

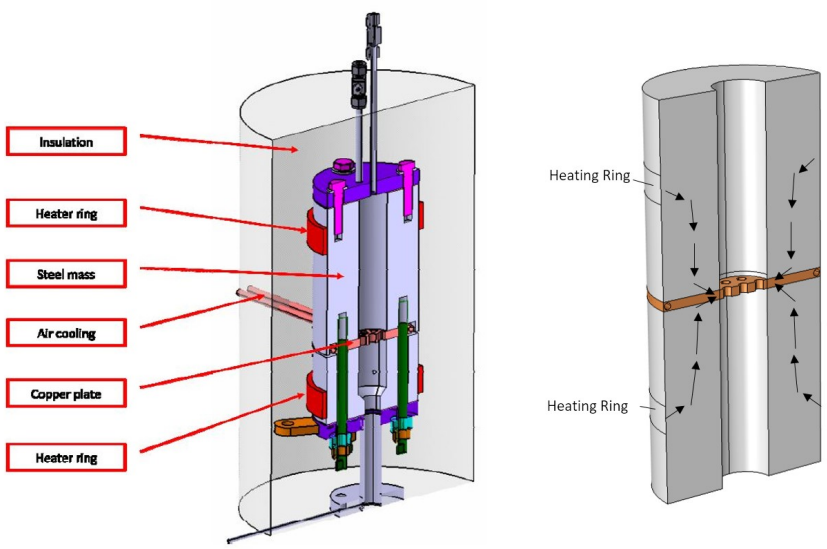

Figure 4.1: SWATH heat plug design. The experimental model from Ghetta et al. (2017b) is shown on the left, and a cross section of the COMSOL model used in this study is shown on the right. Black arrows roughly illustrate the heat flux from the heat rings to the sides of the freeze plugs in the copper grate.

were studied to match the range considered by Makkinje (2017) for the decay heat design. Finally, the sub-cooling of the plugs was varied from 5 K to 25 K. As mentioned in Section 1.2.3, the actual sub-cooling is an unknown parameter; this range was chosen to reflect likely upper and lower extremes. Fewer parameters were considered at the reactor scale because the experimental scale studies were used to narrow down parameters of interest.

Table 4.1: Parameters evaluated in SWATH study for both simulations conducted at the experimental and reactor scale.

	Experimental Scale	**Reactor Scale**	
Parameter	FliNaK	FliNaK	LiF-ThF_4
Number of plugs	1, 4, 7	1, 7	1,7
Aspect Ratio	0.5, 1.0, 1.5	1.0	1.0
P/D ratio	1.05, 1.25, 1.50, 1.75, 2.0	1.05, 1.50, 2.0	1.05, 1.50, 2.0
Sub-cooling (T_{sub}) [K]	5, 10, 15, 20, 25	5, 10, 15, 20, 25	5, 10, 15, 20, 25

4.3. Geometry and Boundary Conditions

For the experimental scale, dimensions were used as reported in Ghetta et al. (2017b). For the scaled model, all dimensions were increased by a factor of 4 in order to simulate the same design with a realistic draining pipe diameter of 0.2 m. Key model dimensions are listed in Table 4.2 and shown in Figure 4.2.

Table 4.2: SWATH experimental and reactor scale model dimensions.

				Heater		
Model	**Height** [m]	**Pipe Radius** [m]	**Steel Thickness** [m]	**Width** [m]	**Distance** [m]	**Power** [W]
Experimental Scale	0.355	0.025	0.0575	0.025	0.08875	1250
Reactor Scale	1.420	0.100	0.2300	0.100	0.35500	6375

The boundary conditions used in the simulations are shown in Figure 4.2 as well. All exterior boundaries of the SWATH design are assumed to be adiabatic. This includes the interior of the draining pipe below the freeze plug and the bottom of the copper plate. The single freeze plug was modeled as axisymmetric, while

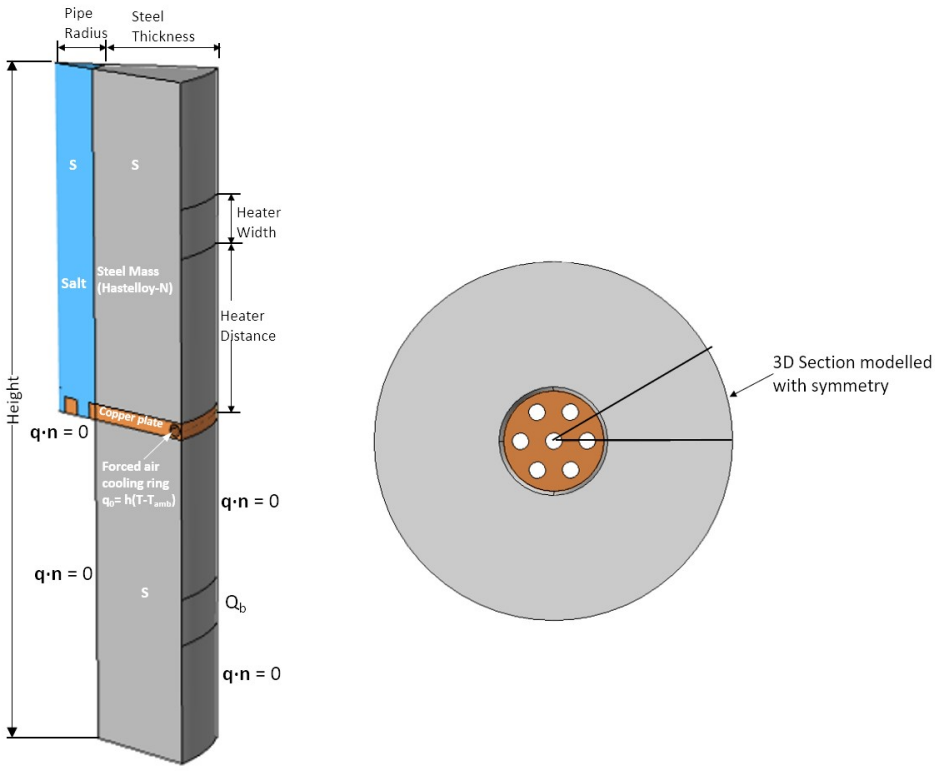

Figure 4.2: COMSOL model geometry and boundary conditions are shown on the left. A top view of the full SWATH model is shown on the right, of which only a section was modeled using symmetry boundary conditions (indicated with an S).

all others were modeled in 3D with symmetry boundary condition $-\boldsymbol{n}\cdot\boldsymbol{q} = 0$ used on all interior surfaces marked with an 'S' in Figure 4.2. The heaters were modeled as a boundary heat source $Q_b = \frac{P}{A}$ W/m^2, with A defined as the surface area of the heater rings. Forced air cooling was modeled by applying a convective heat flux boundary condition to the interior surface of the cooling ring, $q_0 = h_{air}(T - T_{amb})$, with the ambient temperature T_{amb} = 293 K. A relationship between the convective heat transfer coefficient, h_{air}, and the volumetric air flow rate through the cooling pipes was established experimentally for the ORNL freeze plug design in Richardson (1962). This correlation is shown in Figure 4.3.

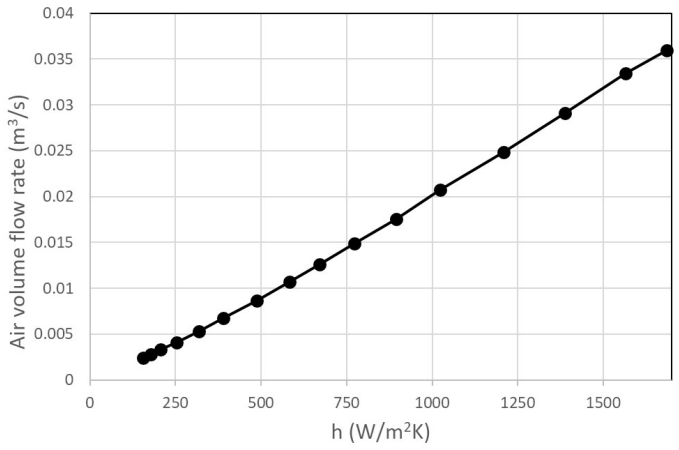

Figure 4.3: Heat transfer coefficient measured as a function of cooling air flow for the ORNL freeze plug. Experimental data, adapted from Richardson (1962).

In the experimental model, the power was set at P = 1250 W for both heating rings, based on the specifications from the SWATH experimental setup in Ghetta et al. (2017b). For the reactor scale model, increasing

the power by a factor of 16, proportionally to the increase in surface area, led to unacceptably high temperatures in the model (i.e. larger than 1800 K). Hence, the power was reduced to 6375 W, for which the maximum steady state temperature within all models fell below the critical temperature of 1473K (Brovchenko et al., 2013).

In all models, the cooling pipe was assumed to be encased in the copper plate. For the models containing multiple plugs, the cooling pipe was assigned a diameter $D_{cooling} = D - 2$ mm. For the model with one plug, the diameter was chosen at $D_{cooling} = D/4$, where D is the freeze plug diameter.

Because the diameter of the cooling pipe, copper plate thickness, and freeze plug height vary across all simulations, the cooling airflow needed to form the plug also varies. Thus, the convective heat transfer coefficient of the airflow was assigned manually for each simulation such that the desired minimum (sub-cooled) temperature was obtained in the freeze plugs. Since the melting results are very sensitive to the sub-cooling temperature, care was taken to ensure that the margin of error in the sub-cooling was 0.05 K of the desired sub-cooling temperature, which is deemed sufficiently small relative to the total sub-cooling temperature. This minimum temperature was generally observed only at the exterior edges of the freeze plugs closest to the draining pipe (and, hence, closest to the cooling pipe). By default, the thickness of the copper plate was set equivalent to the freeze plug diameter, D. This was done for consistency with prior studies of the freeze plug, which assume a one-to-one plug diameter to height ratio to maximize the surface area, and hence friction, between the plug and the surrounding grate.

4.4. Freeze Plug Configurations

Simulations were run for several different freeze plug configurations, including a single plug and designs involving four and seven plugs in the copper grate. Copper grates containing both four and seven plugs are included to study the effect of plugs not located the same distance from the exterior of the draining pipe. The size of the freeze plugs in both of these configurations was determined from circle packing theory, which defines the maximum diameter, D_p, of a hole packed in a circle of radius R:

$$D_p = \frac{2R}{1}, \qquad \text{for one hole;} \tag{4.1}$$

$$D_p = \frac{2R}{1+\sqrt{2}}, \quad \text{for four holes;} \tag{4.2}$$

$$D_p = \frac{2R}{3}, \qquad \text{for seven holes.} \tag{4.3}$$

It is necessary to maintain some copper between the individual plugs for the structural integrity of the copper grate, and in order to conduct heat to the sides of the plugs. The ratio of the freeze plug diameter to the maximum hole diameter, obtained through hole packing theory, is governed by the pitch (P) to diameter (D) ratio (Figure 4.4). The diameter of the freeze plugs is given by

$$D = \left(\frac{P}{D}\right)^{-1} D_p. \tag{4.4}$$

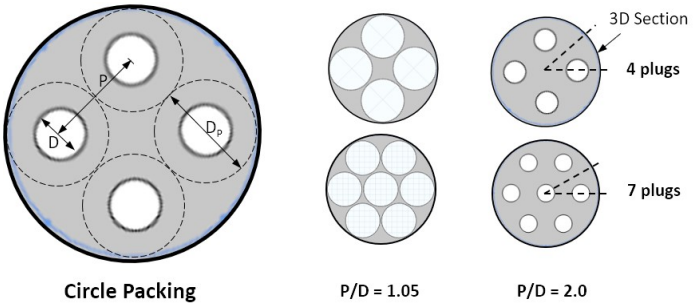

Figure 4.4: Left: Circle packing schematic. P refers to the distance between the center of two adjacent plugs, while D refers to the diameter of an individual freeze plug. Right: Schematic of freeze plug grates for 4 and 7 plug designs with P/D ratios of 1.05 and 2.0.

4.5. COMSOL Implementation

The plug was modeled in COMSOL Multiphysics using the heat transfer module with phase change, which uses the apparent heat capacity method described in Section 2.7. Flow, including natural convection or bouyancy effects, was not modeled. The accuracy of COMSOL phase change simulations for melting without convection was extensively discussed in Chapter 3. All simulations were run in the following two steps:

1. First, a steady state simulation was run with both cooling and heating active. This step resulted in a steady state approximation of the freeze plugs' shape.

2. Second, a transient simulation was run with both cooling and heating switched off. In this step, the melting of the freeze plugs was modeled.

4.5.1. Meshing and phase change temperature range, ΔT

A tetrahedral mesh was used in all simulations. The mesh was refined significantly in the region of the freeze plug (Figure 4.5) in order to ensure a smooth melting front. For the experimental scale, the maximum element face length within the freeze plug region was set at $6.7{\cdot}10^{-4}$ m. In order to maintain reasonable computational times, a larger mesh with a maximum element face length of $1.0{\cdot}10^{-3}$ m was used in the scaled model. Outside the freeze plug region, a default COMSOL mesh was used, with the element size defined for general physics as 'extremely fine'. This corresponds with a maximum element size of $7.0 \cdot 10^{-3}$ m in the experimental scale model, and $2.8 \cdot 10^{-2}$ m in the scaled model.

Following the recommendation in Section 3.1, the phase change temperature range, ΔT, should be as small as possible, and at least $\Delta T \leq T_{sub}$. Based on this criteria, $\Delta T = 2$ K was used in the experimental model and $\Delta T = 4$ K in the scaled model.

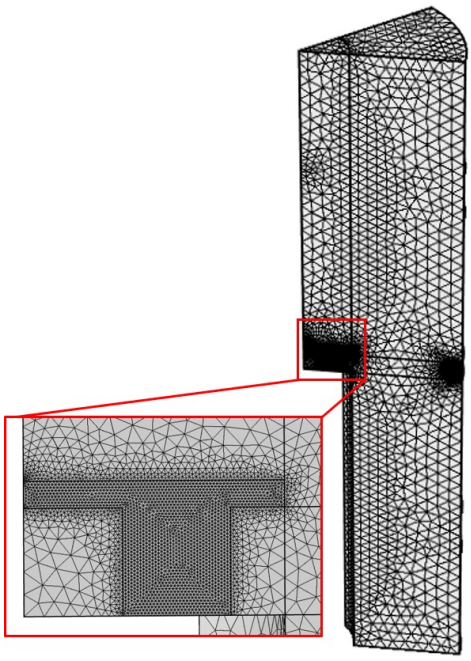

Figure 4.5: Meshing of 3D geometry, including mesh refinement in vicinity of freeze plugs.

4.5.2. Computation of melting time

In the apparent heat capacity method the phases are described according to the phase indicator, θ_l.

$$\theta_l = \begin{cases} 1, & \text{for liquid phase} \\ 0, & \text{for solid phase} \end{cases} \tag{4.5}$$

The center of the melting front is located at $\theta_l = 0.5$, while the region defined by $0 < \theta_l < 1$ captures the width of the macroscopic melting front, commonly known as the mushy zone. Unless otherwise noted, the melting times in this study are calculated using the conservative criteria that in order for an edge to be considered melted, $\theta_l = 1$ along that entire edge. Along an edge with height y, the criteria then becomes

$$\int_0^y (1-\theta_l)\,dy = 0. \tag{4.6}$$

For the designs containing multiple freeze plugs, the melting time of the freeze plug was computed at both interior and exterior plug edges, shown in Figure 4.6 for the 1, 4 and 7 plug grates. Note that these edges are defined to extend well above the height of the copper grate.

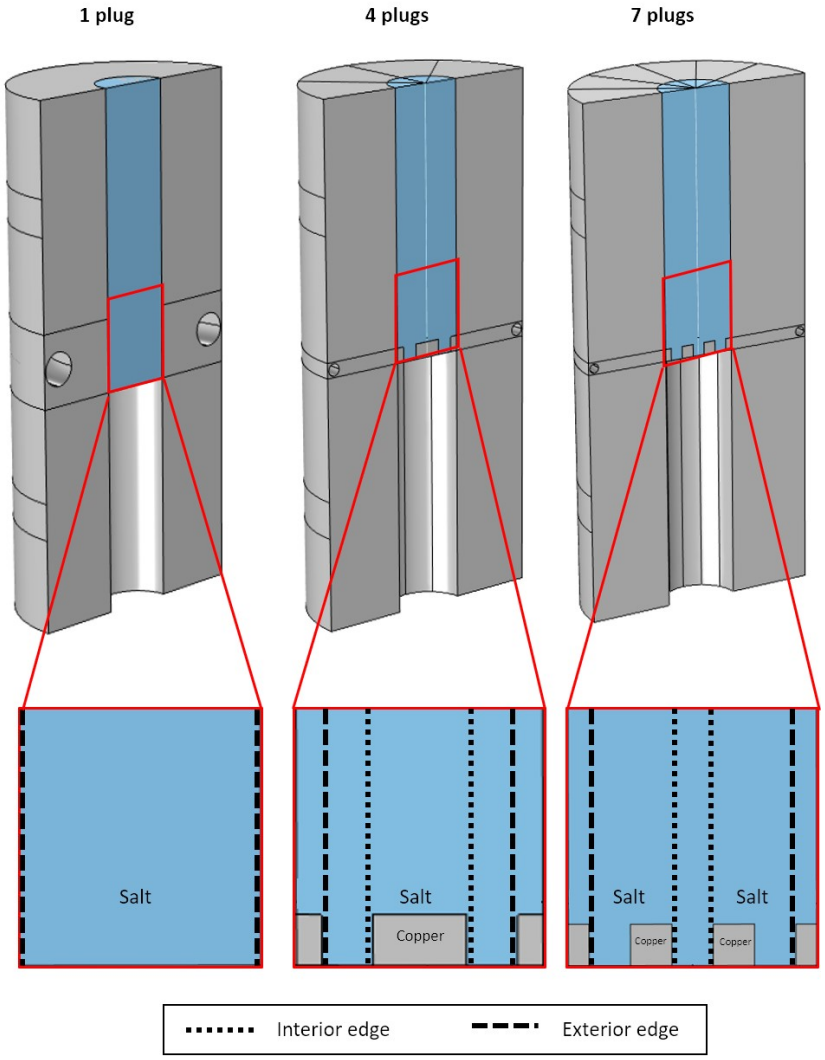

Figure 4.6: Cross sections of 1, 4, and 7-plug designs showing interior and exterior edges used to calculate plug melt times.

4.6. Results - Experimental Scale

At the experimental scale, simulations were run for the 1, 4, and 7-plug freeze plug designs. The effect of increasing P/D ratios was studied for both 4 and 7-plug designs. For the 7-plug design, aspect ratios of 0.5, 1.0, and 1.5 were also considered. Finally, effects of increasing sub-cooling of the freeze plug was studied for both 7-plug design with a P/D ratio of 1.05, as well as the 1-plug design. Study parameters and detailed results are included in the appendix in Tables A.1, A.2, and A.3.

P/D Ratio In this study, the P/D ratio in of the copper grates with 4 and 7 freeze plugs was increased from 1.05 to 2.0. Since the aspect ratio of the plugs was kept constant, the thickness of the copper plate decreased with an increasing P/D ratio, leading to a reduction in thickness of approximately 50% when the P/D ratio was increased from 1.05 to 2.0, for both 4 and 7-plug designs. Since the diameter of the cooling pipes decreases proportionally with the copper plate thickness, the compressed air flow rate had to be increased as well, in order to maintain the desired sub-cooled temperature. The maximum temperature observed in the model increased only slightly with P/D ratio, by a total of 8 K for the 4 plug model and 5K for the 7-plug models, respectively (see Tables A.1 and A.2 in the appendix). This increase is logical, since the mass of the freeze plugs is decreasing. The maximum temperature observed in these models was 1013 K, which lies well below the critical temperature of 1473 K.

The steady-state shapes of the freeze plugs at T_{sub} = 5 K and melting progression are shown in Figure 4.7 for the P/D ratios of 1.05 and 2.0. For this sub-cooling temperature, a thin layer of frozen salt forms above the copper grate with a thickness of approximately 2.1 - 2.5 mm. The tops of the freeze plugs are curved, and the level of the frozen salt is distinctly lower in the center of the plugs than at the edges. Although the maximum thickness of the frozen salt layer remains relatively constant for all simulations, it represents an increasing percentage of the plate thickness. In the model with 7 plugs, this frozen layer increases from representing 15% of the thickness of the copper plate at a P/D ratio of 1.05, to 32% at a P/D ratio of 2.0. Both the absolute and relative thickness of the frozen salt layer above the plate are plotted in Figure 4.8 as a function of increasing plate thickness.

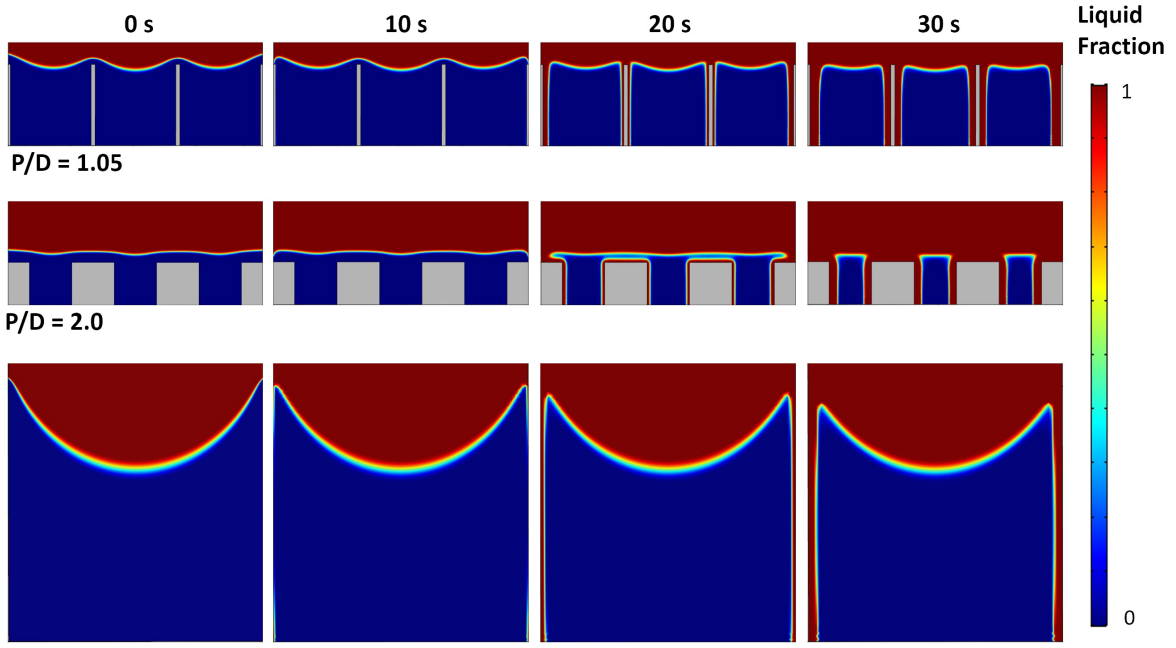

Figure 4.7: Experimental scale freeze plug cross section with T_{sub} = 5 K at different stages in melting. The 7-plug design with P/D ratios of 1.05 and 2.0 is shown on top, and the 1-plug design is shown below.

Melting results for the different P/D ratios studied are summarized in Figure 4.9. Melting time increases significantly with the increasing P/D ratio, from 22 s to 29 s for the 4-plug model, and 20 s to 30 s for the 7-plug design. This behavior is best explained by the increasing relative thickness of the frozen salt layer above the plate. Simulations show that this frozen layer is primarily melted from below, through heat conducted from the steel blocks through the copper plate. The thicker this copper plate is relative to the thickness of the salt layer, the more heat flux there is to melt the salt per unit distance. The suggestion is then that thicker plates, those with a lower P/D ratio in this case, are advantageous.

For higher P/D ratios, the interior and exterior edges melt at approximately the same time, while for the P/D ratio of 1.05, the exterior edge melts significantly sooner than the interior edge. This behavior can also be attributed to the frozen salt layer above the plug. This layer is extremely narrow with a P/D ratio of 1.05 at the exterior edge, such that it is quickly melted by both the heat in the Hastelloy-N block and heat transferred through the copper grate. As the P/D ratio increases, this layer becomes wider, and heat transfer from the

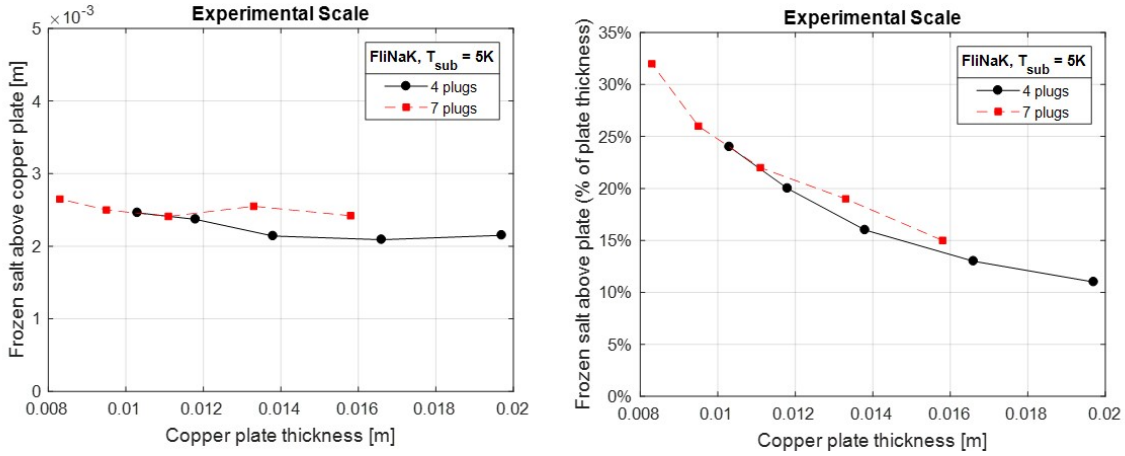

Figure 4.8: Left: thickness of frozen salt above copper plate as a function of the copper plate thickness for both 4 and 7 plug freeze plug designs. Right: Thickness of frozen salt above copper plate as a percentage of the plate thickness as a function of the copper plate thickness for both 4 and 7 plug freeze plug designs.

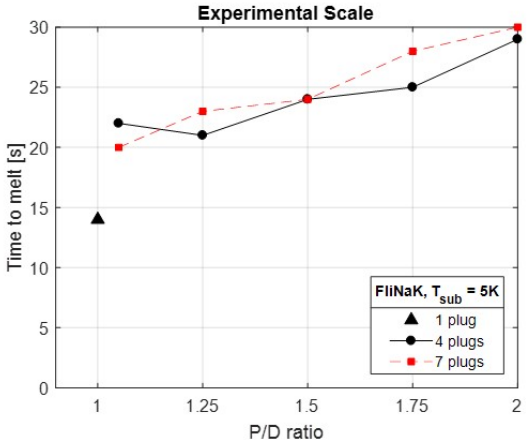

Figure 4.9: Melting time for the 1 plug design, and for 4 and 7 plug designs as a function of P/D ratio for T_{sub} = 5 K.

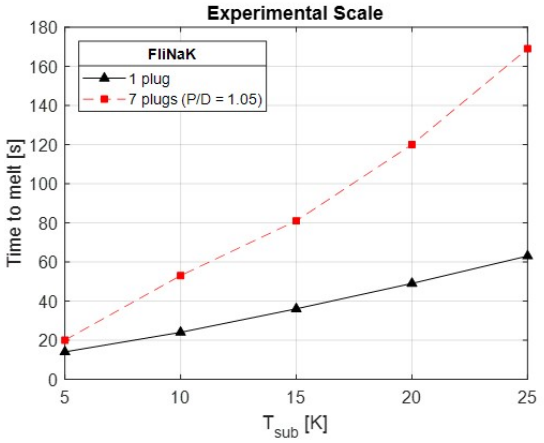

Figure 4.10: Melting time as a function of increasing sub-cooling for 1 and 7 plug designs.

draining pipe wall has less effect.

Number of plugs The melting times for the 4 and 7- hole plug configurations are comparable. The introduction of a central hole appears to have a negligible effect on both the steady state shape of the freeze plugs and melting results. This is likely because the high conductivity of the copper plate minimizes differences in heating or cooling between the center and exterior of the grate. We might expect less consistent results with a less conductive grate. The most important difference between the two plugs configurations is in their effect on the draining of the reactor. As noted in Section 2.4, the draining time is significantly affected by the degree to which a grate blocks the draining pipe (represented as % Open in the results tables). The 7-plug design is therefore favorable to the 4-plug design, since it obstructs the draining less. The following sub-cooling study will be based on the most favorable configuration identified so far: the 7-plug grate with a P/D ratio of 1.05.

The single plug design melts in 14 s at T_{sub} = 5 K, which is faster than any configuration involving multiple plugs. The distinct advantage of this design is that only the sides of the plug have to be melted, whereas the in the multi-plug designs, the salt layer on top of the plate also has to be melted.

Sub-cooling To study the effect of sub-cooling, simulations were run with both the 1 and 7-plug designs, at increasing sub-cooling temperatures of T_{sub} =5 K, 10 K, 15 K, 20 K, and 25 K. Melt times as a function of sub-cooling are presented in Figure 4.10. For the 7-plug design, each 5 K increase in T_{sub} was found to increase the melting time at the interior edges by 37 s on average. The 1-plug design is less sensitive to sub-cooling

than the multi-hole designs, with melt times increasing approximately 12 s per 5 K increase in T_{sub}.

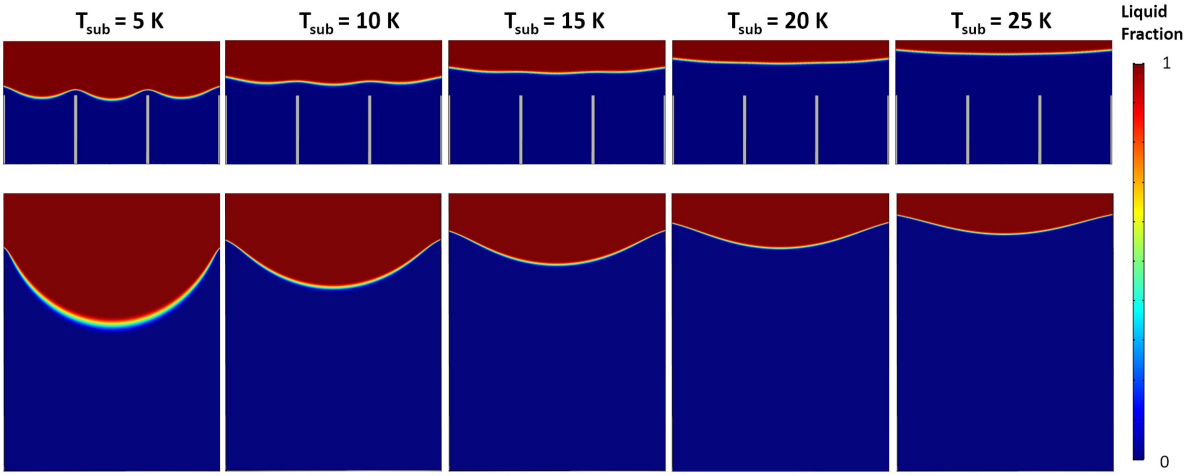

Figure 4.11: Experimental scale steady state freeze plug cross section for increasing T_{sub}. The 7-plug design is shown on top for P/D = 1.05, and the 1-plug design is shown on the bottom.

Cross sections of the 1 and 7 plug designs are shown in Figure 4.11 as a function of T_{sub}. Here, it is evident that the shape of the 7-plug design appears nearly planar after T_{sub} = 10K. Moreover, each 5 K increase in T_{sub} increases the thickness of the frozen salt by 14% on average (see Table A.3 in the appendix). For the 1-hole plug, the maximum height of the plug increases only minimally with an increase in sub-cooling, exceeding the thickness of the copper by 3% at T_{sub} = 5 K, and 19% at T_{sub} = 25 K. The minimum height of this plug, measured in the center of the pipe, increased more substantially - from just 71% of the copper grate height at T_{sub} = 5 K to 111% at T_{sub} = 25 K.

4.6.1. Aspect ratio

The effect of the freeze plug's aspect ratio was studied for the multi-hole plug by running simulations for aspect ratios of H/D = 0.5, 1.0, and 1.5 on the 7-hole plug where H is the height of a freeze plug and D the diameter. The results, summarized in Figure 4.12, are consistent with the results from the P/D study. Melting times the highest for $H/D = 0.5$, and are roughly the same for $H/D = 1$ and $H/D = 1.5$. This affirms an earlier observation that the thickness of the frozen layer above the plug (as a percentage of the plug's height) drives the melt times, not the plug surface area.

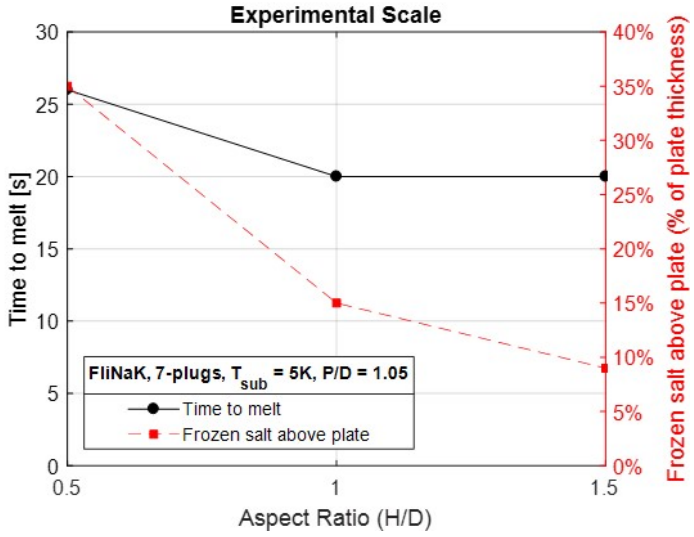

Figure 4.12: Melting time and frozen plug thickness as a percentage of the plate thickness for aspect ratios of 0.5, 1.0, and 1.5.

4.7. Results - Reactor Scale

The SWATH freeze plug design was modeled at a realistic reactor scale, in which all dimensions of the experimental design were increased by a factor of 4, resulting in a draining pipe diameter of 0.2m. Simulations were run using the 7-plug design for T_{sub} = 5 K and P/D ratios of 1.05, 1.5, and 2.0 for both FliNaK and LiF-ThF_4 salt compositions. For the 1-plug design, the effect of increasing sub-cooling was also studied for both salt compositions. The maximum temperatures observed in these models range from a 1020 K for the single plug with sub-cooling of 25 degrees, to a maximum of 1194 K for the LiF-ThF_4 7-plug design with P/D = 1.05. These temperatures lie well below the critical temperature of 1473 K (1200°C). Study parameters and detailed results are included in the appendix in Tables A.5 and A.6.

7-plug design As was seen at the experimental scale, a layer of frozen salt forms above the plate. While this layer is only slightly thinner for the plugs with a P/D ratio of 1.05 (7mm) than for the plugs with a P/D ratio of 2.0 (8mm), it represents roughly 25% of the copper plate thickness at P/D = 2.0, compared to just 11% at P/D = 1.05. Both the absolute and relative thickness of the frozen salt layer above the plate are plotted in Figure 4.13 as a function of increasing plate thickness.

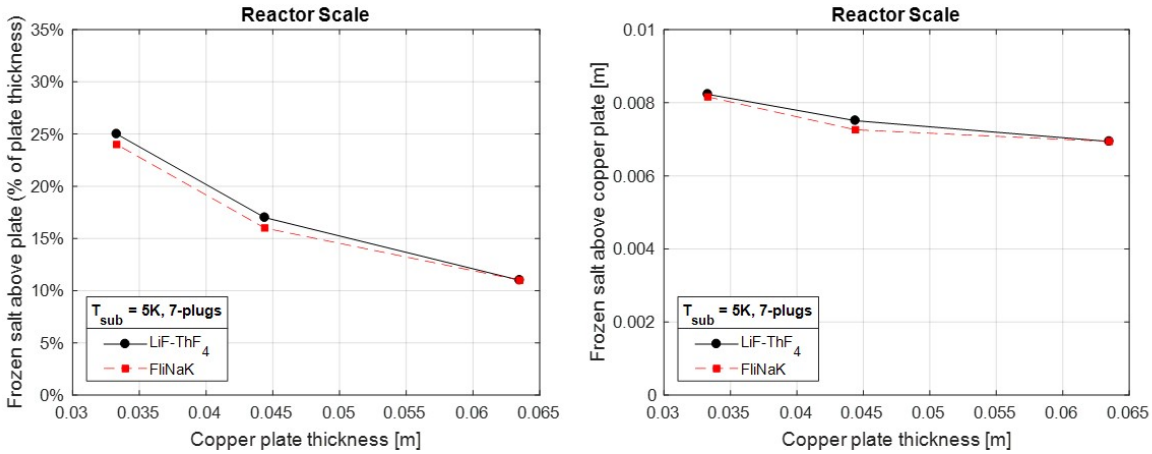

Figure 4.13: Left: thickness of frozen salt above copper plate as a function of the copper plate thickness for FliNaK and LiF-ThF_4 7-plug designs. Right: Thickness of frozen salt above copper plate as a percentage of the plate thickness as a function of the copper plate thickness for both FliNaK and LiF-ThF_4 7-plug designs.

For the FliNaK salt, melt times were consistent with the experimental scale, increasing by an average factor of 13 compared to the experimental scale, from 265s for P/D =1.05 to 375s for P/D = 2.0. Cross sections of the melting progression for the FliNaK plug at the reactor scale are shown in Figure 4.14.

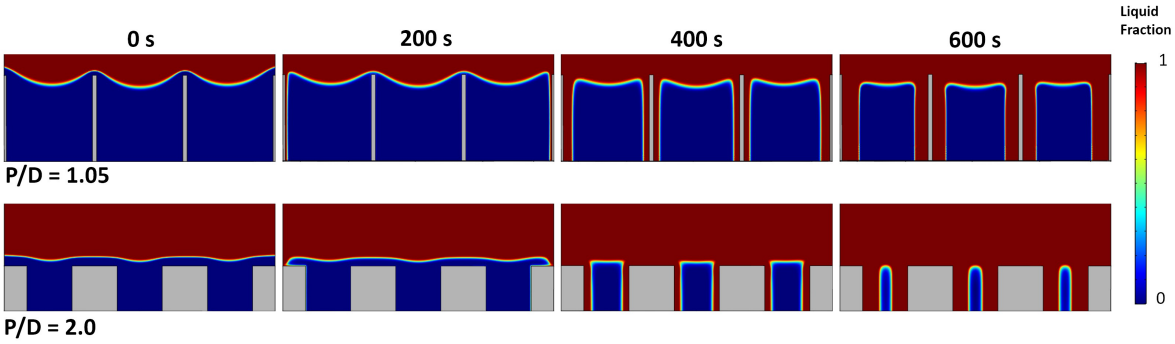

Figure 4.14: Reactor scale FliNaK freeze plug cross section at various times for 7-plug design with P/D of 1.05 and 2.0.

COMSOL simulations of the 7-plug LiF-ThF_4 design show that the interior edges melt in 750 s - 1000 s, which is 2.5 - 3.0 times slower than the FliNaK plug. Oddly, the plug with P/D ratio of 1.5 takes the longest to melt completely. For reasons that are not understood, a thin mushy layer persists in this simulation above the copper grate for a longer time than in the other models. More insight can be gained into these results by

examining images of the melting process in Figure 4.15, which shows that the design with a P/D ratio of 2.0, a mushy layer above the plug persists long after the sides of the plug have melted.

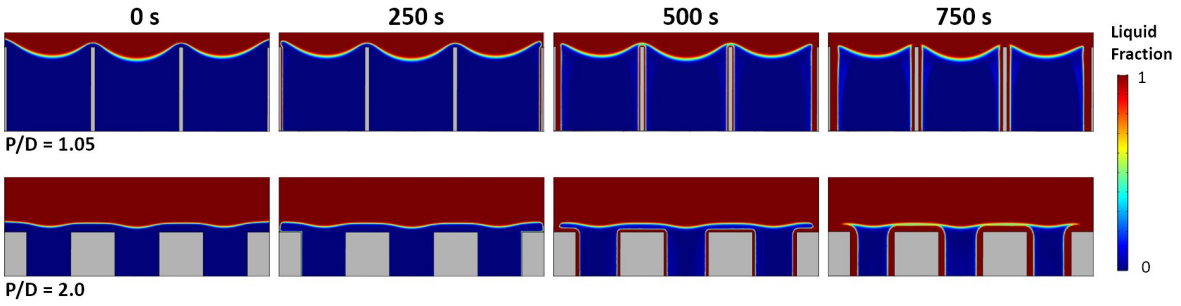

Figure 4.15: Reactor scale LiF-ThF_4 freeze plug cross section at various times for 7-plug design with P/D of 1.05 and 2.0.

To better assess the feasibility of the LiF-ThF_4 plug at the reactor scale models, the melt times were also calculated for a less conservative, but arguably more realistic melting criteria $\int_0^y (\theta_l < 0.5)dy = 0$. Here, half of the mushy zone defined by $0 < \theta_l < 0.5$ is considered liquid, with the melting front defined to lie in the center of the mushy zone. This stricter definition of the melting front location reduces the melt time at the interior edges by 15% – 30%, to 570 - 760 s for the LiF-ThF_4 plug, and the unusually high melt time for P/D =1.5 disappears. These melting results are summarized in Figure 4.16.

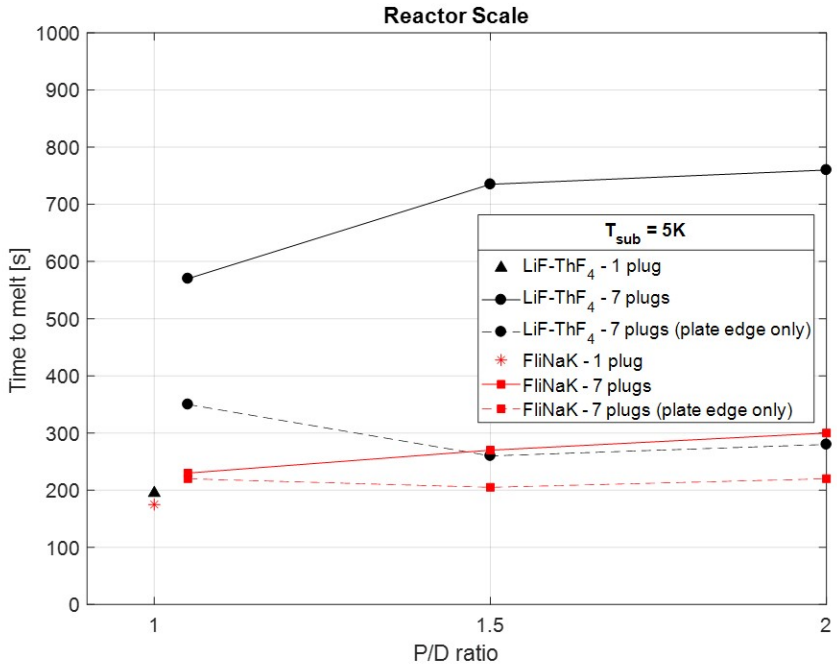

Figure 4.16: Melt times (total and plate edges only) for single plug design, and for 7 plug design as a function of P/D ratio.

The different performance of the LiF-ThF_4 and FliNaK plugs is governed by the need to melt the frozen salt layer above the copper grate. Indeed, in Figure 4.16 we see that the difference in melt times for the two salt compositions is minimal if only the contact edge of the copper grate is considered. Since only a small volume of salt needs to be melted to remove these contact edges, it is not surprising that these melt times are minimally sensitive to the material properties of the plug. In contrast, the time required to fully melt the salt layer above the copper should scale approximately with the melting rate of the material. In 1D conduction, the melting rate $s(t)$ is proportional to the square root of the Stefan number, St (see Equations 2.7 and 2.9). By this relationship, FliNaK melts approximately 3.35 times faster than LiF-ThF_4 due to its lower latent heat. This is indeed comparable to the trends observed.

1-plug design Simulations were run for the 1-plug model for increasing sub-cooling. Like the 7-plug design, the melting time of the 1-plug FliNaK design increased by a factor of 13 compared to the experimental scale, melting in 175 s at $T_{sub} = 5$ K. The 1-plug design melts much faster than the 7-plug design for $T_{sub} = 5$ K.

Differences between the melting times of the FliNaK and LiF-ThF_4 plugs are insignificant for the 1-plug model. When using only one plug, no frozen layer can form above the grate, and only the vertical contact surface between the plug and the draining pipe has to melt before the plug drops. For this melting scenario, melting times are dominated by the rate of heat conduction through to the location of the freeze plug. Since such a small amount of melting is required to melt the contact surface, the Stefan number of the salt does not drive melting times the way it does in the multi-plug designs, where the thicker frozen layer above the grate must also be melted. Figure 4.17 shows that for both FliNaK and LiF-ThF_4 plugs each 5 K increase in T_{sub} increases melt times by an average of approximately 140 s.

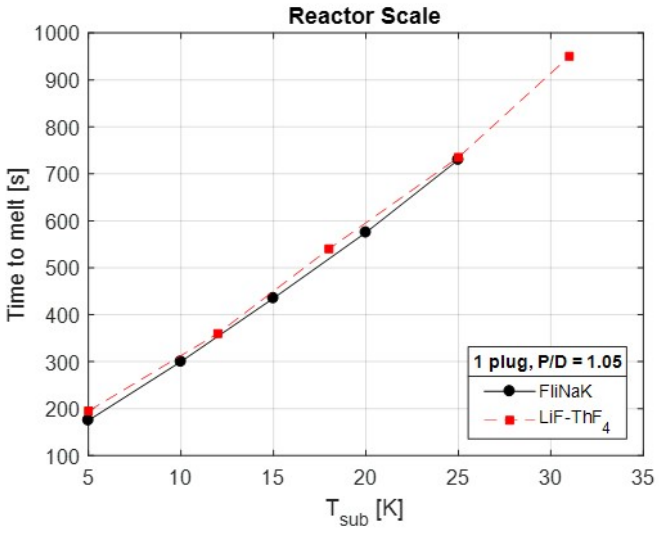

Figure 4.17: Melt times for increasing T_{sub} for 1-plug design at reactor scale.

4.8. Conclusions and Recommendations

The performance of the SWATH freeze plug design depends on many factors which were not considered in this analysis, including the thickness of the Hastelloy-N heating block and the location of the heating rings. Moreover, the objective of this study was not to optimize the design of the SWATH plug. Rather, this study sought to help guide the direction of further study into this design by identifying how some general design parameters, such as the choice of a design containing one, four, or seven plugs, the minimum degree of sub-cooling required during transient conditions, the P/D ratio and aspect ratios of the plug, affect the plug's performance, and how the design performs at a reactor scale. In this light, some general conclusions and recommendations can be drawn:

- The single-plug design melts at least 35% faster than all multi-plug configurations studied. The performance of this plug is only weakly dependent on the Stefan number of the fuel salt. Melt times under 300 s were observed for the LiF-ThF_4 plug with $T_{sub} \leq 10$ K at the reactor scale;
- For a multi-plug design, the fastest melt times are achieved by minimizing the relative thickness of the frozen salt layer above the plug. This can be achieved by minimizing the copper surface between plugs through a low P/D ratio (for example 1.05), by maintaining a plug aspect ratio of $H/D \geq 1.0$, and minimizing T_{sub};
- No clear advantages are obtained from a grate configuration in which all freeze plugs are equidistant to the heat source, compared to one featuring a central plug. The latter configuration,which minimizes the draining time, should therefore be chosen;
- The sensitivity of all results to the thickness of the frozen layer above the copper grate warrants further investigation into the salt thickness that can remain before a plug realistically drops. It is possible, for

example, that once the edges of the plugs have melted the thin (7 mm - 8 mm) layer of frozen salt above the plate breaks under the hydrostatic pressure in the reactor. In this case, the melting times used in this analysis are excessively conservative.

5

Study of Decay Heat Plug Design

The following chapter presents the results of COMSOL simulations of the original decay heat freeze plug design. First, the implementation in COMSOL is described, including the geometry, meshing, and boundary conditions used, as well as the different configurations for the freeze plug that have been considered. Simulation results are then presented. The goal of this study is to determine how the initial sub-cooling temperature, height of the cavity above the plug, and freeze plug design affect melting times.

5.1. Decay Heat Plug Description

The original MSFR freeze plug design considered within SAMOFAR involves melting the plug using decay heat that is released in the reactor, for example after a power loss accident. Such a freeze plug design is dependent on the efficient transfer of decay heat to the plug through the molten salt in the draining pipe above the plug and through the draining pipe itself. Melting times for this design are strongly dependent on the distance between the freeze plug and the reactor core, and the degree to which the decay heat in the reactor is mixed in the draining pipe above the freeze plug (Ghetta et al., 2017b; Swaroop, 2016). Additionally, factors such as the sub-cooling temperature requirement will affect the melt rate of the plug, as mentioned in Section 1.2.3.

5.2. Study Design

The studied parameters are listed in Table 5.1. A single plug, occupying the full width of the draining pipe, is studied, along with a design consisting of 7 smaller plugs in a copper plate. The single plug design was originally studied by Swaroop (2016), although melting through the sides of the plug was not taken into account. The 7-plug design was studied by Makkinje (2017) and Deurvorst (2017) in a domain limited to the height of the plate. The following study will re-examine these designs with more realistic boundary conditions.

Because mixing of decay heat in the draining cavity above the plug is minimal after power loss (Section 2.8 and Swaroop (2016)), convection is expected to play a minimal role in the melting of the plugs and is not accounted for in this study. This significantly reduces the computational effort involved, and is a conservative approximation. Because conduction is an inefficient mode of heat transfer for the fuel salt, the total heat flux reaching the plug depends strongly on the distance between the plug and the decay heat in the core. To study this effect, melting times are compared for increasing cavity heights between 0.01 m and 0.20 m.

Previous studies of the multi-plug design have optimized the spacing between plugs under the assumption that heat is conducted to the sides of the plugs through the top of the plate. Using this assumption, the distance between plugs should be approximately equal to the radius of the individual plugs to allow for efficient heat conduction to the freeze plugs (Makkinje, 2017). Realistically, however, an insulating layer of frozen salt may form on top of the plate, such that the dominant mode of heat transfer is through the sides of the freeze plugs via the draining pipe. In this case, melting of the plugs may more closely resemble that seen in the SWATH design. Keeping this and the conclusions from the SWATH study in mind, multi-plug designs were studied for P/D ratios of 1.05, a.25, and 1.5. Larger P/D ratios are not studied as they were shown to be inefficient by Makkinje (2017) and for the SWATH design.

Finally, the melting times are computed for sub-cooling temperatures ranging from 5 K to 25 K. Sub-cooling affects the steady-state shape of the freeze plug and, additionally, increases the energy required to

melt the plug. The latter may be advantageous, as the plug should be able to withstand minor fluctuations in cooling and temperature without melting.

Table 5.1: Parameters evaluated in decay heat plug study.

Parameter	Values considered
Fuel salt	LiF-ThF_4
Number of plugs	1, 7
Cavity Height [m]	0.01, 0.05, 0.1, 1.5, 2.0
P/D ratio	1.05, 1.25, 1.5
Sub-cooling (T_{sub}) [K]	5, 10, 15, 20, 25

5.3. Geometry and Boundary Conditions

The draining pipe diameter is set at 0.2 m for all simulations, while the thickness of the draining pipe was kept constant at 0.02 m. Just as with the SWATH design, the multi-plug designs were simulated with a 3D "slice" of the plug using a symmetry boundary condition applied on the interior surfaces. The 1-plug design was simulated in a 2D axisymmetric model. The reference salt composition, LiF-ThF_4 is used in all simulation. The draining pipe above the plug is assumed to be made of Hastelloy-N, while the pipe adjacent to the freeze plug is assumed to be copper. The plug geometries and boundary conditions used in the simulations of both 7- and 1-plug designs are shown in Figure 5.1. An aspect ratio of 1 is assumed for all plugs.

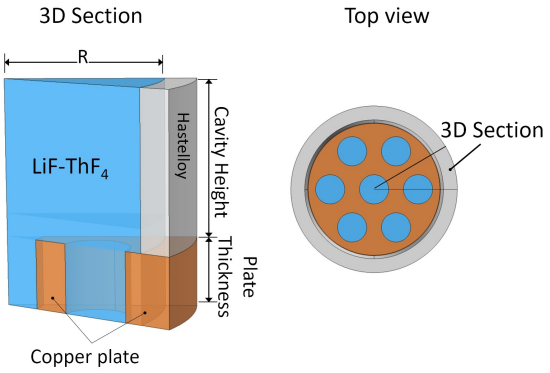

(a) Materials and geometry of 7-plug design.

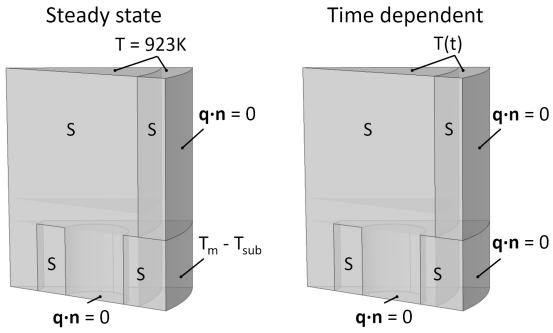

(b) Boundary conditions of 7-plug design.

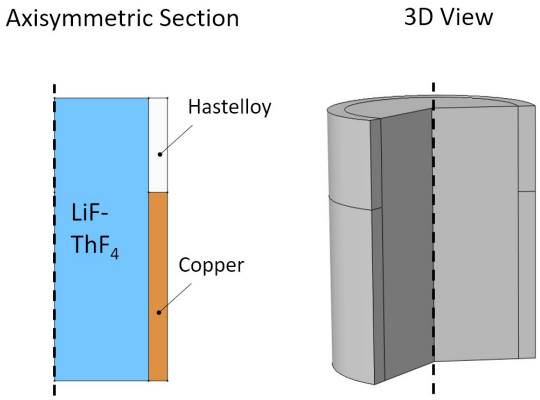

(c) Materials and geometry of 1-plug design.

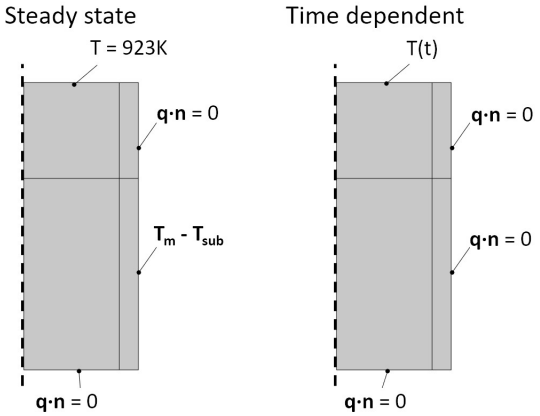

(d) Boundary conditions of 7-plug design.

Figure 5.1: Boundary conditions and geometry of 7-plug and 1-plug designs.

Like the SWATH study, these simulations were run in two steps:

1. First, a steady-state simulation was run to determine the initial conditions of the plug prior to melting. In this simulation, a temperature boundary condition equivalent to the sub-cooling temperature, $T_m - T_{sub}$, is applied to the exterior of the draining pipe in the region of the freeze plug. This boundary condition replaces the forced air cooling pipe from the SWATH simulations, and simplifies the modeling process by eliminating the need to manually adjust the cooling air flow to achieve a desired sub-cooling. Due to the high conductivity of copper, the minimum temperature in the plugs will be approximately equivalent to this sub-cooling in the steady state. At the top of the cavity, a temperature boundary condition of 923 K is applied to simulate the mean temperature in the core during reactor operation. All other exterior surfaces are modeled as adiabatic.

2. Second, a time dependent simulation was run to simulate conditions after power loss, including the melting of the plug. Here, the time-dependent temperature from Equation 2.2 is applied to the top of the cavity, and all other exterior surfaces are modeled as adiabatic.

5.4. COMSOL Implementation

Implementation in COMSOL was consistent with the scaled SWATH study in Chapter 4. A refined mesh was used in the vicinity of the freeze plug with a maximum mesh element size of 10^{-3} m. Elsewhere, the default extremely fine COMSOL mesh was used. A phase change temperature range of $\Delta T = 4$ K was used, and melt times were computed based on a melting front location at $\theta_l = 0.5$. All simulations were run for 2000 s.

5.5. Results Summary

Figure 5.2 summarizes the results of this study, showing melting times at increasing cavity heights for all P/D ratios and sub-cooling temperatures considered. For the 7-plug design, melting times are shown for both the full thickness of the plug (including any salt layer above the copper plate) and for the height of the copper plate only. This makes it possible to distinguish the effect this salt layer has on the melting times. More detailed results are included in Appendix B.

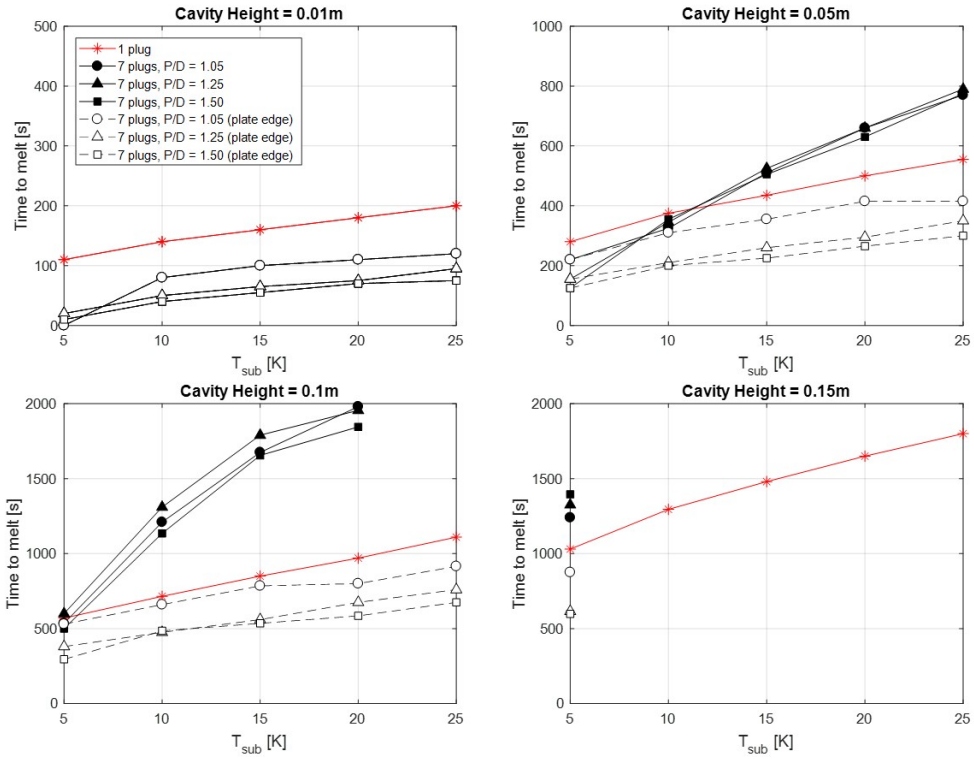

Figure 5.2: Melting times as a function of sub-cooling for all P/D ratios and cavity heights. Limited data is shown for a cavity height of 0.15 m because most models did not melt in the simulation time of 2000 s.

5.5.1. Frozen salt layer formation on grate

As the 7-plug design is moved further away from the core, a frozen salt layer forms on top of the copper grate. The thickness of this layer increases with the height of the draining cavity and with increased sub-cooling. When the cavity height it 0.01 m, this salt layer is insignificant. For a cavity height of 0.05 m the thickness of this layer increases by approximately 2-2.5 mm per 5 K increase in sub-cooling , while for a a cavity height of 0.2 m the increase is approximately 10 mm per 5 K increase in sub-cooling. These trends are shown in Figure 5.3.

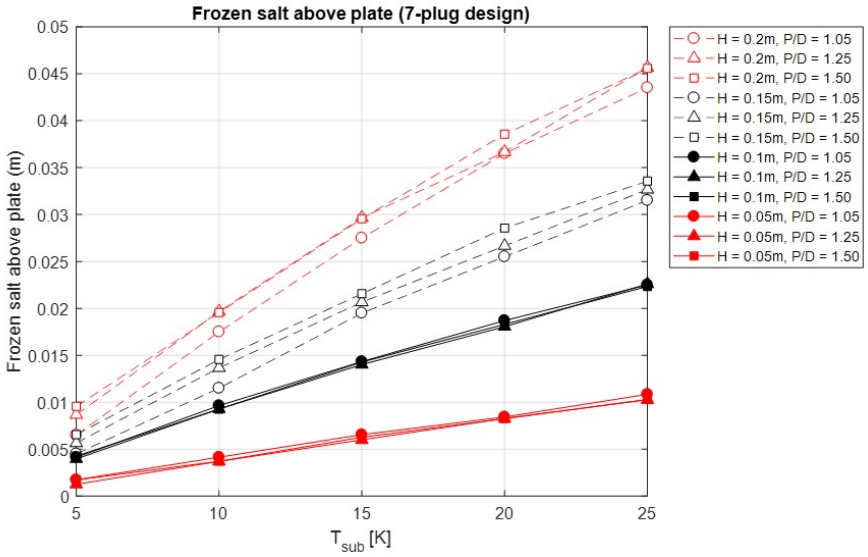

Figure 5.3: Thickness of frozen salt layer above 7-plug design as a function of sub-cooling, cavity height, and P/D ratio.

Figure 5.4 shows cross sections of the steady-state shape of the 7-plug design at 0.01 m and 0.10 m for increasing sub-cooling. At 0.01 m from the core, sub-cooling of at least 10 K is required to fully form the central plug, and the plugs maintain a significant depression in their center for all sub-cooled values. When the plug is 0.1 m from the core, minimal sub-cooling is required to fully form the plug; the frozen surface is nearly planar for sub-cooling greater than 15 K.

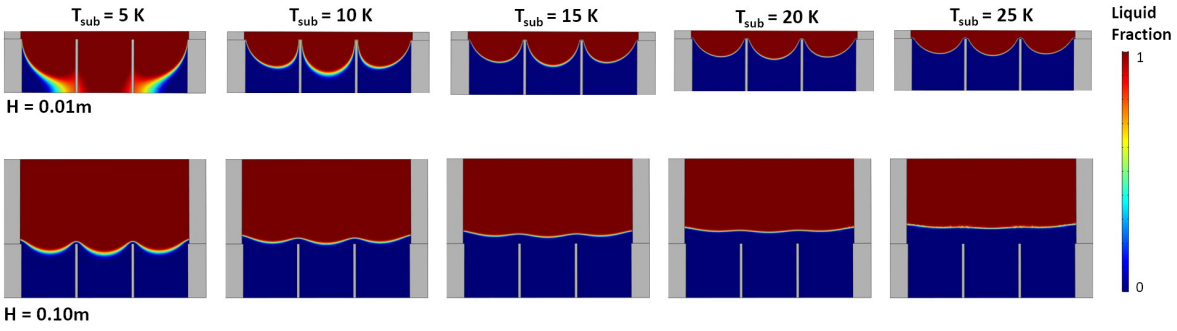

Figure 5.4: Cross section of steady-state freeze plug shape for increasing sub-cooling with plug for 7-plug design (P/D = 1.05) located 0.01 m from reactor core (top) and 0.10 m from core (bottom).

5.5.2. Effect of sub-cooling and cavity height on melting

At a cavity height of 0.01 m, all plugs melt rapidly (within 120 seconds for the 7-plug design, and within 200 s for the 1-plug design), and melt times are only weakly dependent on the amount of sub-cooling, increasing by 50% – 90% as T_{sub} is increased from 10 K to 25 K.

For greater cavity heights, Figure 5.2 shows a strong correlation between melting times and sub-cooling. In general, melting times for the 7-plug design are driven by the increasing thickness of the frozen layer above

the plugs. This is exemplified by the fact, as the thickness of the frozen salt layer approximately doubles when the cavity height increases from 0.05 m to 0.10 m, the time required to melt just the edges of the plugs roughly increases by a factor of 2 to 2.5, whereas the additional time needed to melt the frozen layer on top of the plug increases by a factor of 3.5 to 6, depending on sub-cooling. This roughly follows what we'd expect from the Neumann solution, according to which a layer with a thickness of 4 mm takes four times as long to melt than a layer with a thickness of 2 mm.

Figure 5.6 summarizes the melting times at sub-cooling of 5 K for increasing cavity heights. The increase in melting times is non-linear, and more pronounced for the 7-plug design than the 1-plug design, which clearly becomes favorable for cavity heights greater than 0.10 m.

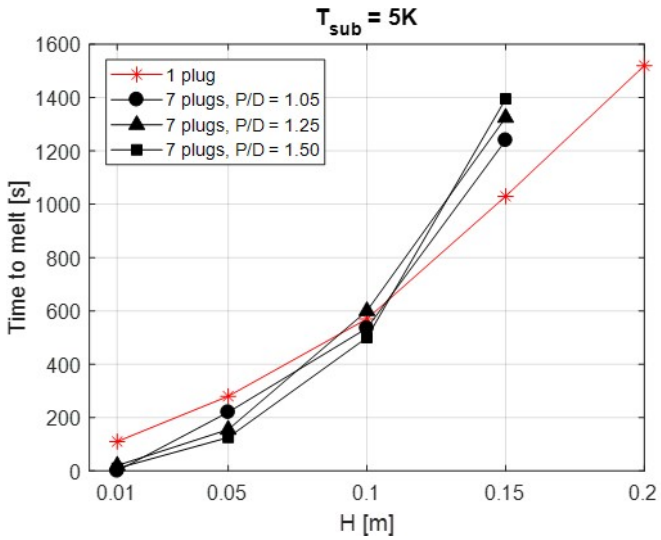

Figure 5.5: Melting time as a function of cavity height for 5K sub-cooling.

5.5.3. Effect of number of plugs

At 0.01 m from the core, the 7-plug design melts faster than the 1-plug design. As the cavity height increases, the 1-plug design becomes increasingly favorable, as the frozen layer on top of the copper grate of the 7-plug design inhibits complete melting. When the cavity height is 0.05 m, the single plug has comparable melting times to the 7-plug design at sub-cooling ≤ 10K, and outperforms the 7-plug design for a sub-cooling > 10K. At a cavity height of 0.1 m, the single plug has a comparable melt time to the 7-plug design for sub-cooling of 5 K and strongly outperforms the 7-plug design as sub-cooling is increased. At a cavity height of 0.15 m, the single-plug outperforms the 7-plug design for all sub-cooling values, none of which melted within 2000 s. Indeed, as the cavity height increases, the melting times of the single plug become increasingly comparable to the melting time of the contact edges of the multi-plug designs.

Figure 5.6 shows how the frozen layer slows down the melting process for plugs located 0.10 m from the core with sub-cooling of 20 K. Here, one can clearly see how the contact edges of the seven-plug design melt long before the frozen layer above the copper plate. Indeed, the frozen layer is melted from the bottom up, through heat conducted through the draining pipe and through the copper plate, rather than by conduction through the molten salt in the draining pipe. This is not surprising, given the favorable heat transfer coefficients of the Hastelloy-N and copper, and highlights the value added by using a highly conductive plate.

These images also highlight that the melting time estimates for the multi-plug design are highly conservative. Realistically, the frozen layer will be continuously pushed against the copper plate by the hydrostatic pressure in the draining pipe. This will ensure that the frozen layer is in direct contact with the plate at all times, and will accelerate the melting process. One should assume, therefore, that more realistic melting times lie somewhere between the time required to melt the inside edges of the plugs and the times reported in this study.

5.5.4. Effect of P/D ratio

In general, the total melting results are quite similar for plugs with a P/D ratio of 1.05, 1.25 and 1.50. All three designs melt within 20 seconds of on another when the cavity height is 0.01 m, 10 - 17 s for H = 0.05 m, and 50-

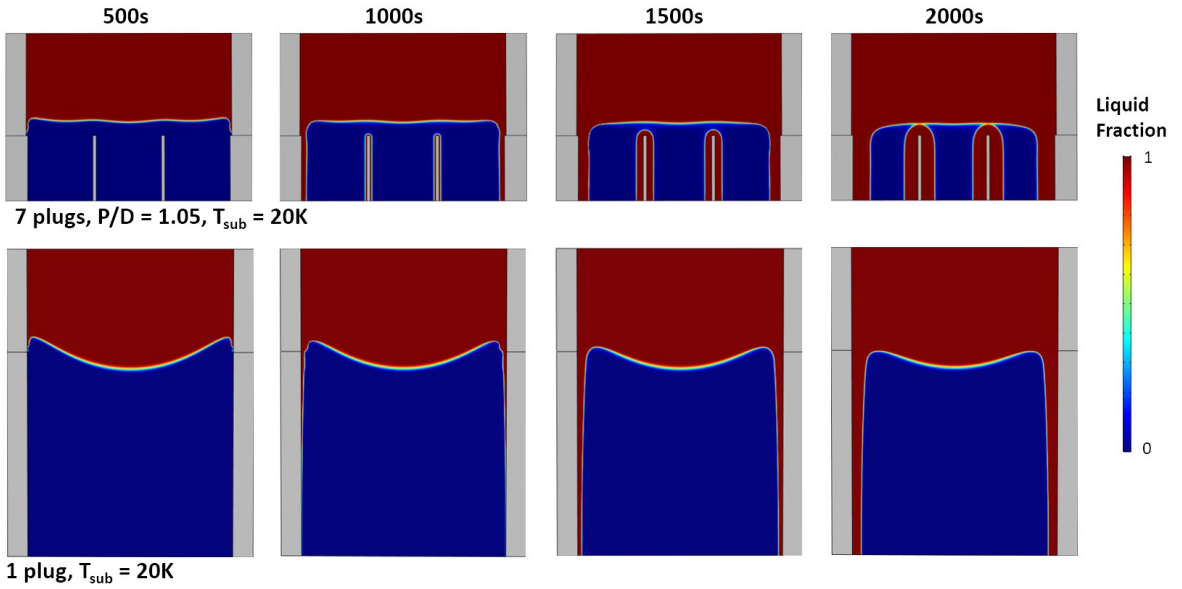

Figure 5.6: Cross sections of melting process for 7-plug design with P/D = 1.05 (top) and 1-plug design (bottom) with plugs located 0.10 m from core and with 20 K sub-cooling.

88 s when H = 0.1 m. The behavior of the P/D = 1.05 plug is a bit different from the rest. The edges of this plug melt substantially later than the edges of the others. When the edges melt, the plate is still insulated by the frozen layer above it, meaning that the edges are being melted by way of heat transfer through the draining pipe and through the sides of the plate. With a P/D ratio of 1.05, heat transfer to the middle of the plate is limited by the thin copper walls between plugs. This is consistent with the observations made by Makkinje (2017), who saw a sharp decline in the heat penetration rate for P/D ratios below 1.2 for a plate heated from above, and smaller differences for P/D ratios between 1.2 and 1.5. This effect is offset by faster melting of the frozen layer above the plate, which can likely be attributed both the smaller volume (and hence thermal mass) of this layer, as was also seen in the SWATH design. It follows that the P/D ratio of the plugs does not appear to be an important determinant of melting times, particularly relative to the height of the draining cavity and sub-cooling amount.

5.6. Conclusions and Recommendations

Several conclusions and recommendations are drawn:

- Since the P/D ratio is not an important determinant of melting times, this ratio should be minimized in a multi-plug design to reduce draining times.
- The single-plug design is generally favorable over a multi-plug design, especially for cavities ≥ 0.05m and for sub-cooling above 5 K. However, further study into the melting behavior of the frozen layer above the plate (which takes the sinking of the frozen salt into account) is required to better quantify the difference in melting times.
- Melting times below 1000 s were observed for the multi-plug design at a cavity height of 0.01 m and 0.05 m (all sub-cooling), and at 0.1 m for sub-cooling below 10 K. For the single plug design, melting times below 1000 s were observed at a cavity height of 0.1 m (all sub-cooling), and at a cavity height of 0.15 m (sub-cooling of 5 K). In the absence of more significant mixing in the draining cavity, the freeze plug would have to therefore be located within 0.1 m of the mixed flow to be melt quickly enough. This likely renders the decay heat design unfeasible based on the requirement that the plug be located some distance from this flow (see Section 1.2.3).

6

Study of Wedge Plug Design

The following chapter describes an alternative wedge shaped freeze plug for the MSFR. To model the unconstrained melting of the wedge, an analytical model is derived in Section 6.2, and validated against experimental results. In Section 6.3, the wedge is simulated in COMSOL using the semi-analytical approach described in Section 3.3. Finally, some obervations are made about the LiF-ThF_4 wedge in Section 6.4.

6.1. Wedge Plug Description

As mentioned in Section 1.2.3, an effective freeze plug melts within the required time, and is stable during transient operation of the reactor, meaning that regular flow and temperature oscillations should not trigger the plug to drop or move out of place. In previous chapters, the single-plug design was shown to be preferable to the multi-plug design for both the decay heat and SWATH freeze plug configurations. Using a single, cylindrical plug nevertheless has a major potential limitation in terms of reliability. The cylindrical plug is at risk of slipping down the draining pipe either at the onset of melting, or due to minor variability in the temperature in the reactor. The plug may then get jammed at a lower point in the draining pipe where inadequate heat reaches it to melt.

To avoid this risk, a wedge-shaped plug is proposed as an alternative to the cylindrical plug. The wedge shape eliminates the risk of the plug slipping down the draining pipe prematurely. As the slanted, 'contact', sides of the plug melt, the hydrostatic pressure in the draining pipe ensures that the sides of the plug stay in close contact with the heated walls, ensuring that a high heat flux reaches the frozen plug, and ensuring rapid melting. Because a larger mass has to be melted than in the case of a cylindrical plug (where only the contact edges had to melt), this design will likely take longer to melt than the cylindrical plug. In the following section, an effort is made to quantify this increase, and identify how factors such as the angle of the plug affect melting.

6.2. Analytical Model

The principle of contact melting for the wedge shaped plug is illustrated in Figure 6.1. The plug is pushed against the heated surface of the draining pipe with a force F_n, representing both the plug's weight and the weight of the fluid in the reactor directly above the plug, causing steady melting at the lower surface of the wedge. The molten liquid that is generated from this process fills a a gap with width δ between the wedge and the heated surface.

To derive an analytical expression for the melting of the wedge, the lubrication approximation is assumed to be valid (see Section 2.9.1). Additionally, the wedge is assumed to be isothermally heated along the slanted edges, and melting at the top of the plug is assumed to be negligible compared to melting at the sides. The governing equations are continuity (Equation 2.30), momentum (Equation 2.29), energy (Equation 2.28), and the Stefan condition (Equation 2.32).

The following boundary conditions for temperature, velocity, and pressure apply to the molten layer:

$$T = \begin{cases} T_h & \text{at} \quad y = 0; \\ T_m & \text{at} \quad y = \delta; \end{cases} \tag{6.1}$$

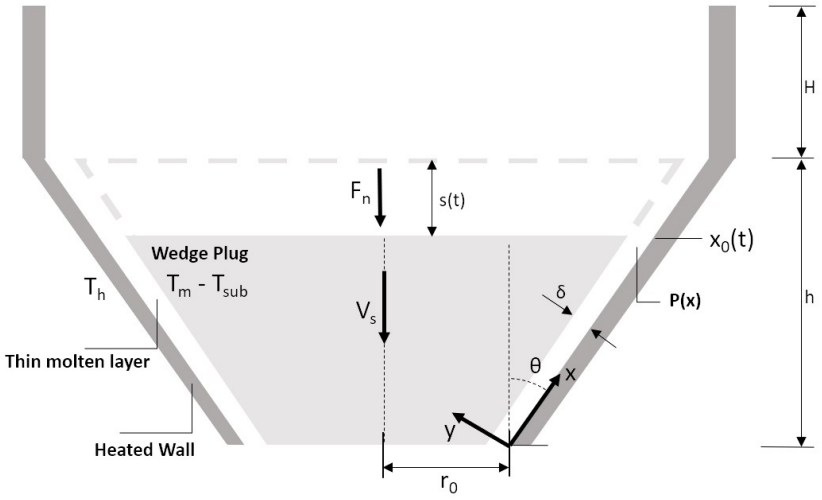

Figure 6.1: Schematic of the wedge plug

$$u = \begin{cases} 0 & \text{at} \quad y = 0; \\ -V_s \cos\theta & \text{at} \quad y = \delta; \end{cases} \tag{6.2}$$

$$v = \begin{cases} 0 & \text{at} \quad y = 0; \\ -V_s \sin\theta & \text{at} \quad y = \delta; \end{cases} \tag{6.3}$$

$$P = \begin{cases} \rho_l g(H + s(t)) & \text{at} \quad x = x_0(t); \\ 0 & \text{at} \quad x = 0. \end{cases} \tag{6.4}$$

The length of the contact surface with the wedge is denoted by $x_0(t)$, defined in terms of the progression of the top of the wedge, $s(t)$:

$$x_0(t) = \frac{h - s(t)}{\cos\theta}, \tag{6.5}$$

where h is the initial height of the wedge. Integrating the momentum equation twice and applying boundary conditions 6.2 gives an expression for the velocity in the fluid layer:

$$u = \frac{1}{2\mu}\frac{dP}{dx}(y^2 - \delta y) - \frac{V_s}{\delta}\cos\theta y. \tag{6.6}$$

Integrating the conservation of mass equation and applying boundary conditions 6.3 yields

$$\frac{d}{dx}\int_0^\delta u\,dy - V_s \sin\theta = 0. \tag{6.7}$$

Substituting u into this expression and integrating yields

$$-\frac{\delta^3}{12\mu}\frac{d^2P}{dx^2} - V_s \sin\theta = 0. \tag{6.8}$$

Integrating twice and applying the pressure boundary conditions gives a general expression for the pressure in the molten layer:

$$P(x) = \frac{6V_s\mu\sin\theta}{\delta^3}(x_0 x - x^2) + \frac{\rho_l g(H+s)x}{x_0}. \tag{6.9}$$

Solving the energy equation and applying the temperature boundary conditions 6.1 gives a linear temperature distribution across the fluid layer:

$$T = T_m + (1 - \frac{y}{\delta})(T_h - T_m). \tag{6.10}$$

From the Stefan condition, the heat balance for the fluid layer gives

$$-\int_0^{x_0} k_l \frac{\partial T}{\partial y}\bigg|_{y=0} dx = \int_0^{x_0} \rho_s V_s \sin\theta (L_H + C_{P_s} T_{sub}) dx. \tag{6.11}$$

Applying 6.10 and assuming that the wedge moves uniformly, such that the melting rate is independent of x, we can write

$$-k_l (T_h - T_m) \int_0^{x_0} \frac{1}{\delta} dx = (L_H + C_{P_s} T_{sub}) \rho_s V_s \sin\theta \int_0^{x_0} dx. \tag{6.12}$$

Thus, the thickness of the fluid layer, δ, can be expressed in terms of the sinking velocity, V_s, as

$$\delta = \frac{k_l (T_h - T_m)}{\rho_s V_s \sin\theta (L_H + C_{P_s} T_{sub})}. \tag{6.13}$$

Substituting Equation 6.13 allows us to represent the pressure in the molten layer independent of the molten layer thickness, δ:

$$P(x) = \left(\frac{\rho_s V_s \sin\theta (L_H + C_{P_s} T_{sub})}{k_l (T_h - T_m)}\right)^3 6 V_s \mu \sin\theta (x_0 x - x^2) + \frac{\rho_l g (H + s) x}{x_0}. \tag{6.14}$$

The forces in the molten layer are balanced if the pressure force in the molten layer is equal to the normal force acting on it

$$2\pi \int_0^{x_0} (x \sin\theta + r_0) P(x) dx = -F_n \sin\theta. \tag{6.15}$$

Here, F_n represents the combined weight of the freeze plug and the fluid in the reactor above the plug, subtracting the bouyancy force of the solid. Accounting for the reduced size of the plug during melting, and assuming the height of the reactor, H, stays constant, this force becomes:

$$F_n = \underbrace{\frac{1}{3}\left(\pi r^2 \left(\frac{r_0}{\tan\theta} + (h - s)\right) - \frac{\pi r_0^2 r}{\tan\theta}\right)}_{\text{Volume of wedge}} (\rho_s - \rho_l) g + \underbrace{(s + H)\pi r^2}_{\text{Volume above plug}} \rho_l g, \tag{6.16}$$

where r is the upper radius of the wedge, given by $r(t) = r_0 + (h - s(t)) \tan\theta$. Substituting the pressure distribution (Equation 6.14) into the force balance (Equation 6.15) allows us to solve for the sinking velocity, V_s:

$$V_s = \frac{ds(t)}{dt} = \left(-\frac{(T_h - T_m) k_l}{(L_H + C_{P_s} T_{sub}) \rho_s x_0)}\right)^{3/4} \left(\frac{\frac{2}{3}((H + s) g \rho_l \pi x_0^2) + (H + s) g \rho_l \pi x_0 + F_n \sin\theta}{\pi \mu \sin^4\theta (2 r_0 + x_0 \sin\theta)}\right)^{1/4}, \tag{6.17}$$

$$= \left(-\frac{St k_l}{C_{p_l} \rho_s x_0}\right)^{3/4} \left(\frac{\frac{2}{3}((H + s) g \rho_l \pi x_0^2) + (H + s) g \rho_l \pi x_0 + F_n \sin\theta}{\pi \mu \sin^4\theta (2 r_0 + x_0 \sin\theta)}\right)^{1/4}. \tag{6.18}$$

Equation 6.17 can be solved by numerical integration to give the progression of the melting front, $s(t)$.

6.2.1. Experimental validation

The analytical model was validated through a simple experiment in which a paraffin wedge was melted in a glass funnel. The objective of this experiment was to document the melting rate of an unconstrained phase change material in a wedge-shaped enclosure heated from the sides.

Experimental setup The experimental setup is depicted in Figure 6.2. The setup includes a glass funnel (Vitrulab Laborware KG), a transparent plastic water tank, a thermocouple thermometer, and an electric immersion water heater (Rommelsbacher). The stem of the funnel extends through a hole in the bottom of the tank and is clamped in place with an o-ring sandwiched between two plastic plates which could be screwed into the plastic tank. This allows the funnel to be removed between experiments in order to form the plug. A scale was placed under the funnel to measure the drained mass, but was ultimately not used because the o-ring seal was not completely waterproof (due to warping of the plastic tank under high temperatures), and the drained wax could therefore not be distinguished from draining water.

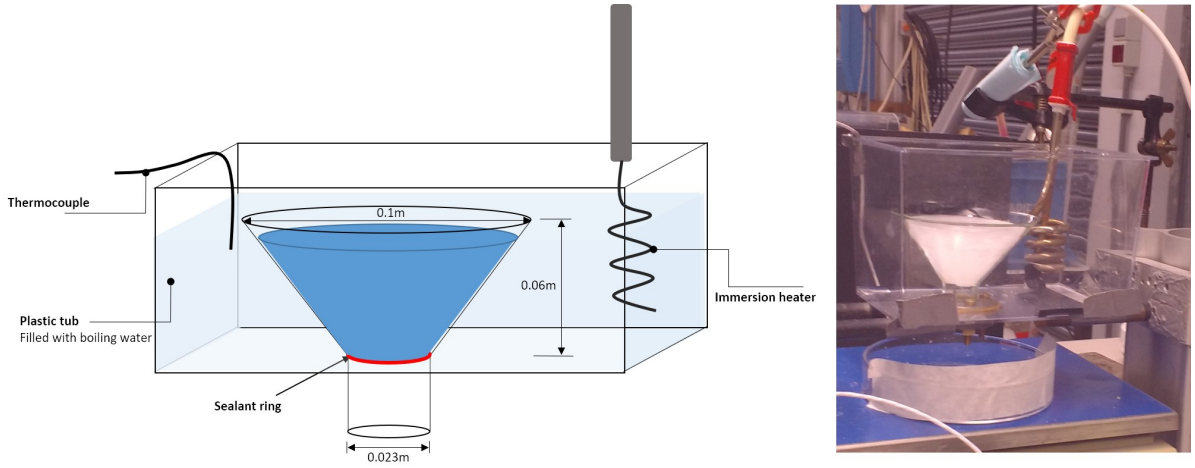

Figure 6.2: Schematic (left) and picture (right) of experimental setup.

Phase change material Paraffin wax was used because it is easily available, inexpensive, and has a comparable Stefan number and thermal conductivity to the fuel salt. The material properties of the Paraffin wax are listed in Table 6.1. Paraffin waxes are typically classified by their melting point. Hard, white paraffin wax granules (Glorex GmbH) were used in this study with a reported melting point of 54°C. Although a melting temperature range was not specified on the product, similar paraffin waxes are classified by melting point ranges of 50 – 52°C, 54 – 56°C, and 58 – 60°C (Sigma-Aldrich, 2017). We therefore assume the paraffin used in this study has a melting temperature range of 2°C.

Table 6.1: Paraffin Material Properties

Property	Paraffin[a]		Units
	Liquid	Solid	
Thermal Conductivity (k)	0.15	0.24	$W{\cdot}m^{-1}K^{-1}$
Density (ρ)	780	860	$kg{\cdot}m^{-3}$
Heat Capacity (C_p)	2100	2900	$J{\cdot}kg^{-1}K^{-1}$
Dynamic Viscosity (μ)	0.205	-	Pa·s
Latent Heat (L_H)	$2.1 \cdot 10^5$		$J{\cdot}kg^{-1}$
Melting Temperature (T_m)	54 [b]		$°C$
Sub-cooling (T_{sub})	34		$°C$
Mean heated wall temperature (T_h)	95		$°C$

[a] Material properties from Ettouney et al. (2006) based on paraffin wax with melting temperature of $52°C$.
[b] As reported on product packaging

Test procedure The wedge was formed by plugging the stem of the funnel with a cork, pouring 90 g of melted paraffin into the funnel, and then allowing the plug to solidify overnight at room temperature (20°C). The mass of the plug corresponds with a wedge height of 0.045 m. However, due to contraction of the wax

during cooling, the top surface of the wedge extended approximately 0.0075 m higher at the edges of the wedge than at the center.

Melting was initiated by filling the plastic tank with boiling water to the top rim of the funnel. At the same time, the immersion heater was turned on. Because no stirring device was used, the temperature was measured at the opposite side of the tank to track the temperature gradient in the tank. The water near the immersion heater was actively boiling for the duration of the experiment, while a temperature of $90 \pm 1^{\circ}C$ was measured at the opposite side of the plug. Photographs were taken every 2 seconds for the duration of the melting process, and the melting progression was measured from these photos using a web-based plot digitizer (Rohatgi, 2017).

Two simulations were conducted: one with a 50 g weight placed on top of the paraffin wedge, and one without. No duplicate simulations were run due to degradation of the plastic tank under high temperatures.

Melting results The melting progression of the paraffin plug without the 50 g weight is shown in Figure 6.3, with the original size of the freeze plug outlined in red. It is clear that the water level in the tank decreases slightly throughout the experiment due to leakage, but remains above the height of the solid wedge. Additionally, the majority of molten fluid is squeezed up, rather than draining out of the funnel: directly before the end of melting, the height of the molten paraffin remains at approximately 2/3 the original plug height. The plug maintains close contact with the glass throughout, and the contact melting fronts appear to stay planar. Unfortunately, the quality of the experimental setup and imaging are insufficient to capture the thickness of the thin molten layer between the solid plug and glass. In fact, the use of a round funnel causes some light distortion where this layer would be.

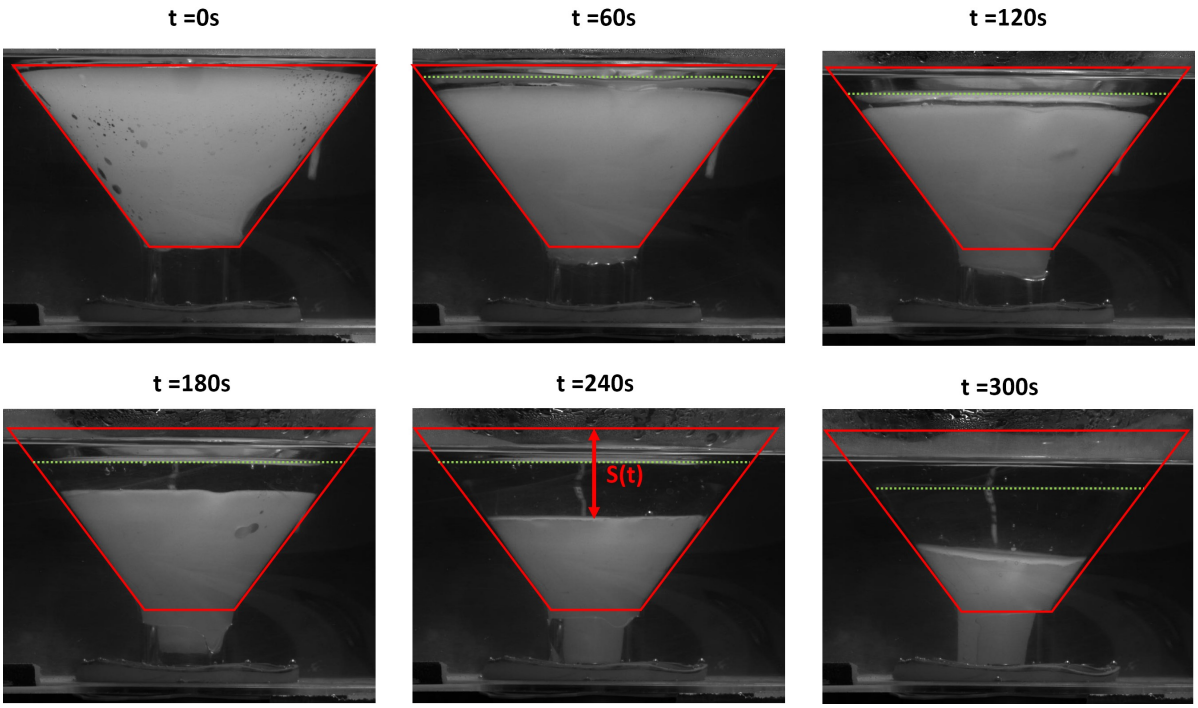

Figure 6.3: Melting progression of paraffin plug without additional weight. The original size of the plug is outlined in red, and the height of the molten paraffin is shown in green.

Figure 6.4 shows that the melting progression, $s(t)$, agrees well with the numerical solution of Equation 6.17. In the experimental simulations, the wedge melted in 340 s without a weight, and in 326 s with a 50 g weight, while the numerical solution yielded melting times of 354 s and 319 s, respectively. Both simulations and the numerical solutions show the melting rate increasing with time. This is in contrast with the cylindrical melting study examined in Section 2.9, where the melting rate was steady. This increase can likely be attributed to the fact that the contact area between the wedge and the funnel decreases more quickly than the decrease in the force acting onto this surface. With more force distributed over a smaller area, the thickness of the molten layer decreases, and the melting rate increases.

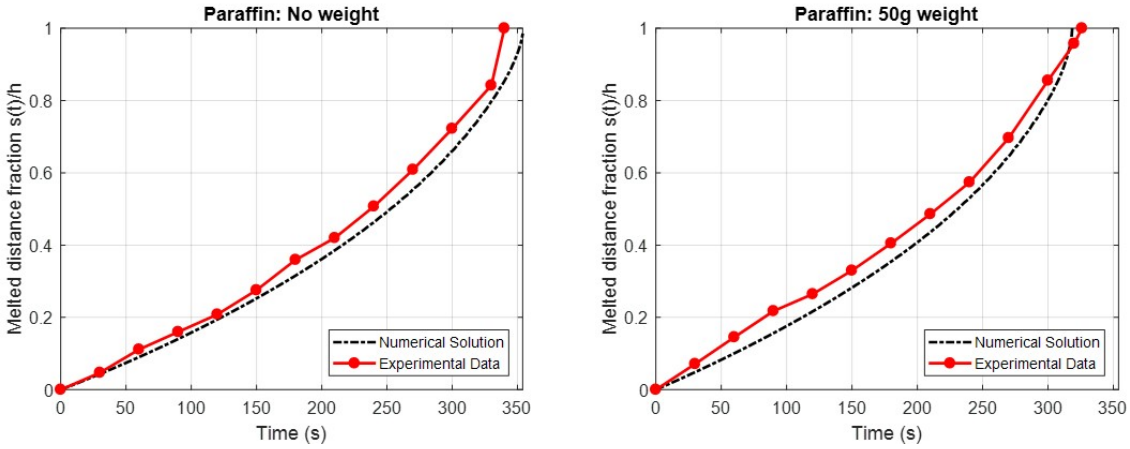

Figure 6.4: Melting progression of paraffin plug compared to numerical solution without weight (Figure 6.4a) and with weight (Figure 6.4b).

For the numerical solution, the reactor height, H, was taken as zero, and it was assumed that none of the liquid drained out during the melting process. Likely sources of error in the experimental results and the corresponding numerical solution include:

1. **Material properties**: The material properties listed in Table 6.1 are estimates based on paraffin wax with a slightly lower melting point than the wax used. Ideally, the experiment would be repeated with an isothermal phase change material with documented material properties (for example, *n*-Octadecane).

2. **Hot wall temperature,** T_h: Because a temperature difference of approximately 10°C was measured within the water tank during the experiment, a constant mean temperature $T_h = 95$°C was assumed in the numerical solution. Ideally, the experiment should be repeated with a more uniform temperature distribution in the water. This could be accomplished by replacing the immersion heater with a system in which hot water is heated externally and continuously pumped through the water tank. Increasing the size of the water tank and insulating the sides not needed to photograph the melting progression would also help ensure a more uniform temperature distribution.

3. **Melting through top of plug**: Melting of the top of of the plug is ignored in the numerical solution, as it is assumed to be negligible compared to melting of the contact surface. This is a standard assumption made in the close contact melting literature (see for example (Kozak et al., 2014; Rozenfeld et al., 2015), and work by Sparrow & Geiger (1986) showed that for a horizontal cylinder only 85−95% of melting was due to close contact melting, with the rest accounted for by natural convection at the top of the solid.

4. **Thermal resistance of glass funnel**: The temperature drop over the glass is assumed to be negligible.

5. **Height of fluid layer above plug**: The numerical model assumes no draining, so the entire melted distance, $s(t)$, of the solid is replaced by liquid paraffin, which exerts a pressure onto the plug. In reality, it was observed that some of the mass drains before the plug drops.

6.3. COMSOL Simulation of Paraffin Wedge Plug

The paraffin wedge was modeled in COMSOL using the same semi-analytical approach explored in detail for an *n*-Octadecane cylinder in Section 3.3. Unlike the cylinder, however, the melting of the wedge is unsteady. As shown in Figure 6.5a, the sinking velocity, V_s, increases linearly throughout the melting process until shortly before the end of melting, when it increases exponentially. As expected, Figure 6.5b shows the inverse for the molten layer thickness, δ, which decreases in thickness almost linearly with time for the first 250 s, and then rapidly narrows.

The approach previously demonstrated with some success for a cylindrical contact melting process assumes quasi-steady melting, and is therefore not really appropriate for this problem. Accounting for the time-dependent melting using this approach would require deriving an analytical solution to Equation 6.17,

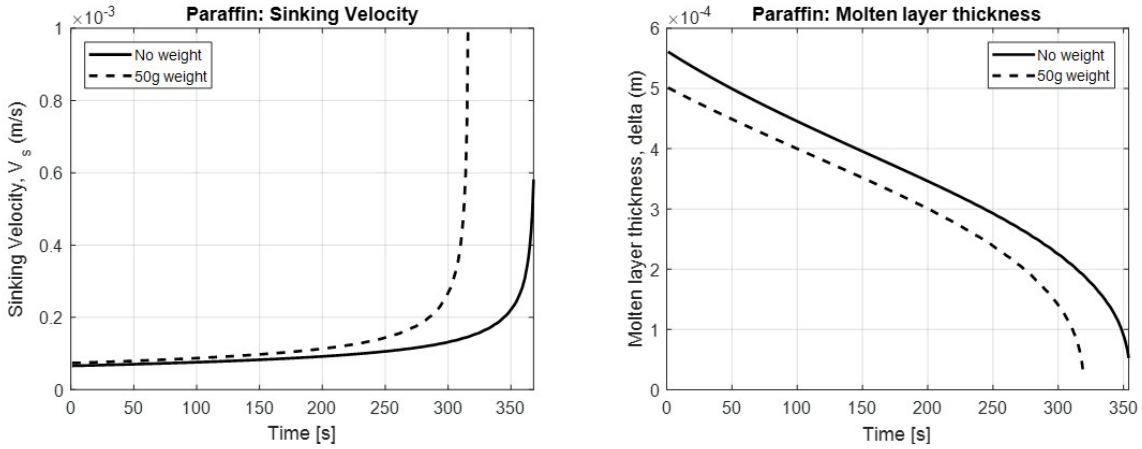

Figure 6.5: Sinking velocity, V_s, and molten layer thickness, δ, as a function of time for the paraffin plug, based on numerical solution to the analytical model (Equation 6.17).

and adjusting the proportionality constant used in the sinking velocity accordingly. Since this could not be done, the following section models the plug with the assumption that melting is steady. While this will not accurately capture the melting process, it is a conservative approach.

The goal of simulating the melting of the paraffin wedge in COMSOL is to gain further insights into the melting process. In particular, the COMSOL model can be used to examine the flow in the molten layer and the importance of natural convection.

6.3.1. Geometry and boundary conditions

The geometry and boundary conditions of the COMSOL model are shown in Figure 6.6. The wedge was modeled with 2D axisymmetry. In the flow module, inlet and outlet pressure boundary conditions of 1 atm were assigned to the top and bottom surfaces of the wedge, respectively. In the heat transfer module, the sides and top of the wedge were assigned a constant heated temperature, $T_h = 95^\circ$ C, while an adiabatic temperature outflow boundary condition ($-\mathbf{n}\cdot\mathbf{q} = 0$) was assigned to the lower boundary. The plug was assumed to initially have uniform sub-cooling of $T_{sub} = 34^\circ$ C.

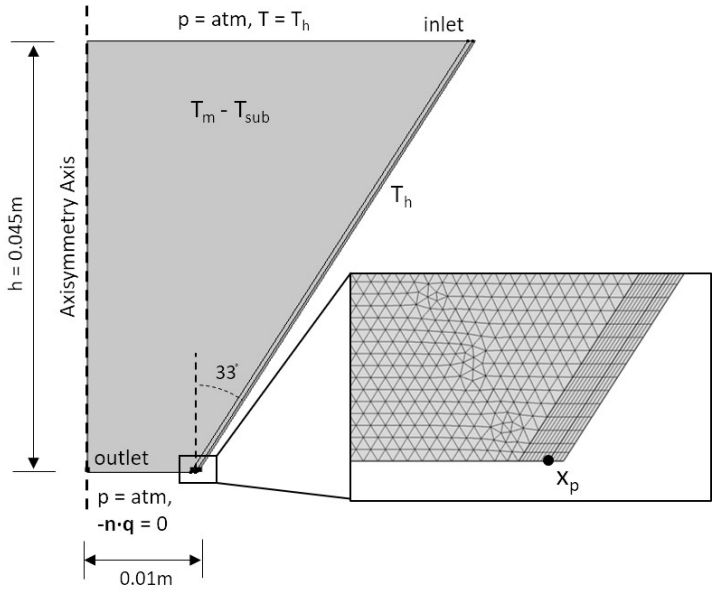

Figure 6.6: Dimensions, boundary conditions, and meshing of paraffin wedge plug modeled in COMSOL with 2D axisymmetry.

Despite the known melting temperature range of 2 K for paraffin, a larger melting temperature range of 10 K was used in this model to avoid excessively fine meshing and/or small time-steps otherwise needed to resolve the melting interface. A mixed mesh was used, as shown in Figure 6.6, with boundary layer elements adjacent to the heated edges and triangular meshing elsewhere. A mesh sensitivity study, equivalent to that already shown in Section 3.3, was repeated for this problem, and showed no sensitivity of the solution on the mesh considered (see Appendix C.1).

6.3.2. Melting results

As before, the sinking velocity was defined at the point x_p, as $V_s = c(T(x_p) - T_m)$. Following the recommendation from Section 3.3, the point x_p was located half way between the expected location of the melting front and the heated surface. Here, the expected location of the melting front was assumed to be $\delta = 4.0 \cdot 10^{-4}$m, equivalent to the average distance expected within the first 250 s of melting seen in Figure 6.5b.

Figure 6.7 shows the wedge after 120 s, 240 s, and 360 s of melting based on the proportionality constant, $c = 5.0 \cdot 10^{-6}$. As was seen in the experiments, the wedge maintains its shape throughout the melting process: the top surface of the wedge remains planar while the sides remain parallel to the heated surface. Some rounding of the wedge is observed at the top corners where the molten fluid is pressed upwards.

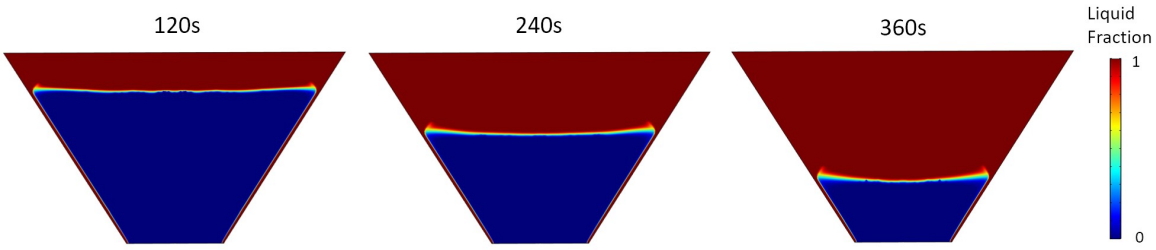

Figure 6.7: Cross sections of the wedge-shaped paraffin plug simulated in COMSOL at 120s, 240s, and 360s.

6.3.3. Effect of proportionality constant, c

The melting progression is shown in Figure 6.8 for a range of proportionality constants. The simulation results agree well with the analytical solution until $t = 200$ s for a proportionality constant $c = 5.0 \cdot 10^{-6}$, after which time the COMSOL solution under-predicts the melting rate.

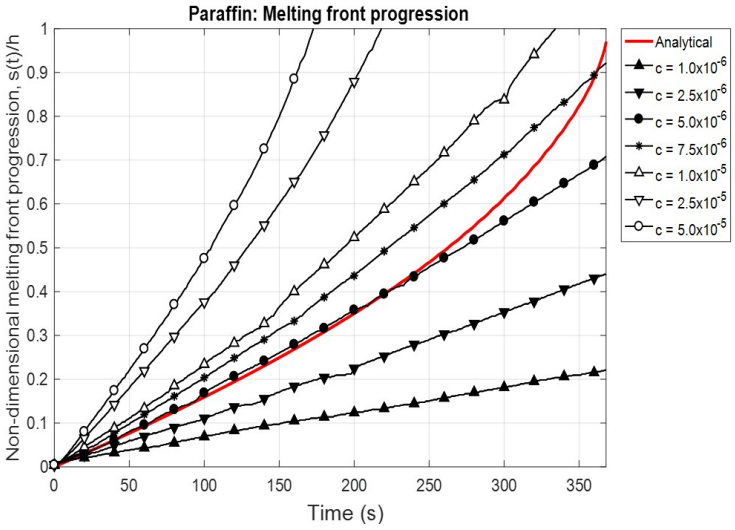

Figure 6.8: Melting front progression in COMSOL simulation for different proportionality constants, compared to analytical solution.

6.3.4. Draining and natural convection

The effect of natural convection on the rate of melting is nearly indistinguishable. Figure 6.9a shows the plug after 240 s of melting with natural convection accounted for through the Boussinesque approximation, while Figure 6.9b shows the same model without natural convection. Velocity streamlines are shown in black in the two models. The fact that natural convection has little effect is not surprising, since continuous sinking of the wedge causes the thin molten layer to remain extremely narrow throughout the melting process.

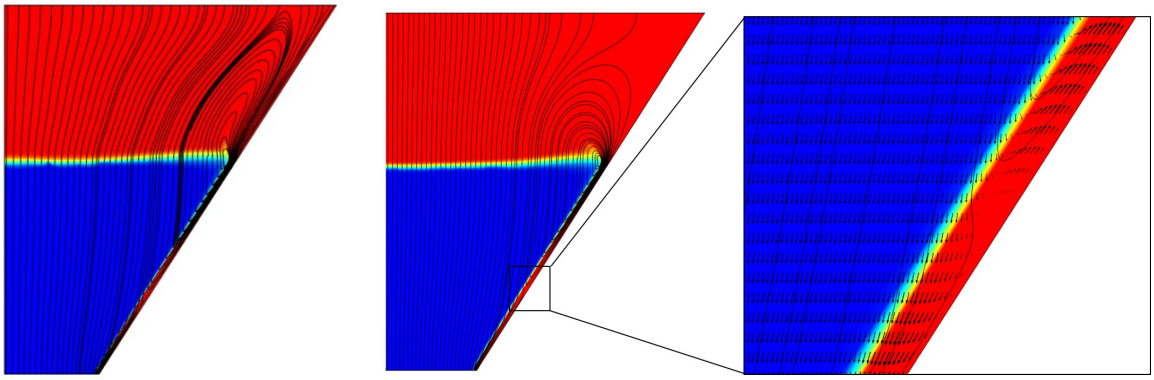

(a) With natural convection

(b) Without natural convection

Figure 6.9: Paraffin wedge after 240 s of melting with and without natural convection. Velocity streamlines are depicted in black, and the velocity magnitude is additionally shown with arrows in Figure 6.9b at the point along the wedge where the flow separates.

In the experiments, it was observed that a portion of the molten wedge is squeezed upward rather than draining out. Unfortunately, the amount of draining could not be tracked due to leaking of the water tank, and was restricted in part by wax build up in the stem of the glass funnel. Although COMSOL simulations of the wedge show that approximately 44% of the melted mass consistently drains out (see Figure 6.10), the proportion should likely be higher, and non-constant with time. The COMSOL simulation does not account for the increase in hydrostatic pressure as fluid builds up above the wedge. For example, in Figure 6.9b the flow separation in the molten layer is occur approximately mid-way up the side of the wedge for the duration of the melting process. Examining the pressure distribution expected analytically in the molten layer (Figure 6.11) nevertheless shows that, as fluid builds up on top of the wedge, the pressure distribution in the molten layer becomes asymmetrical, with an increasing percentage of the molten mass draining out.

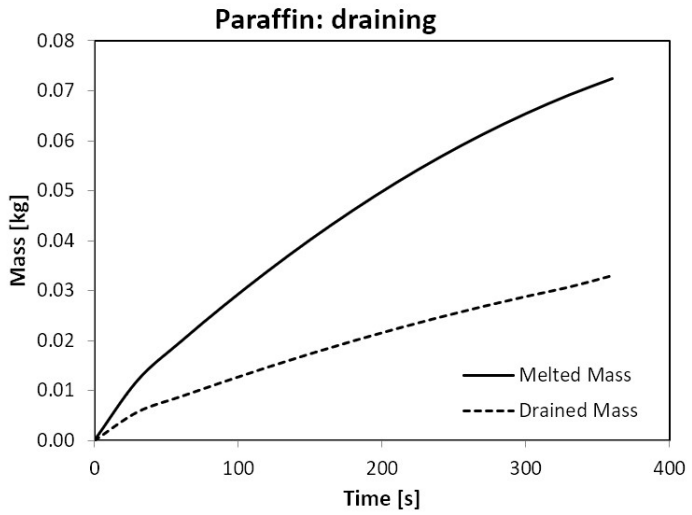

Figure 6.10: Melted mass and drained mass as a function of time for paraffin wedge. From COMSOL simulation with $c = 5.0 \cdot 10^{-6}$.

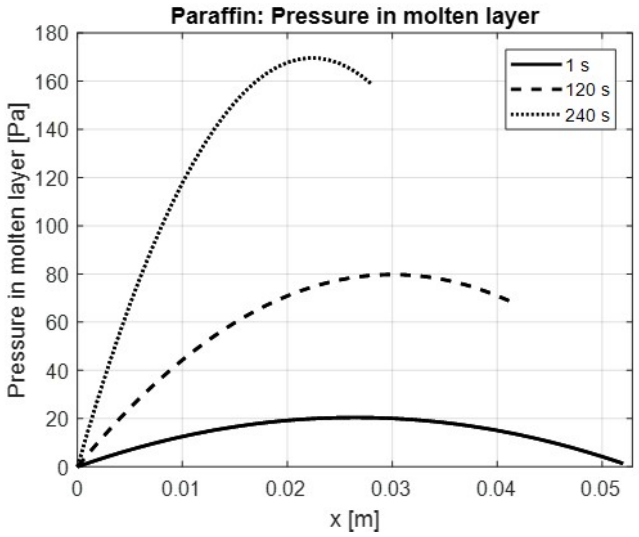

Figure 6.11: Pressure distribution in molten layer of paraffin wedge after 1 s, 120 s, and 240 s of melting, based on analytical solution.

6.4. Wedge shaped MSFR freeze plug

In the following section, the analytical model is applied to a realistic MSFR plug design, and the melting time of the plug is estimated for different wedge angles and Stefan numbers. A reactor height of 2.225 m is assumed (Ghetta et al., 2017a), and both the smaller plug radius, r_0, and the plug height, h, are fixed at 0.20 m. The melting progression of the LiF-ThF_4 wedge is shown in Figure 6.12 as a function of time. As was seen for the experimental wedge, the melting rate is non-linear and increases with time. A wedge angle of 5 degrees, sub-cooling of 5 K, and hot wall temperature of $T_m + 10$ K are assumed throughout this section, unless noted.

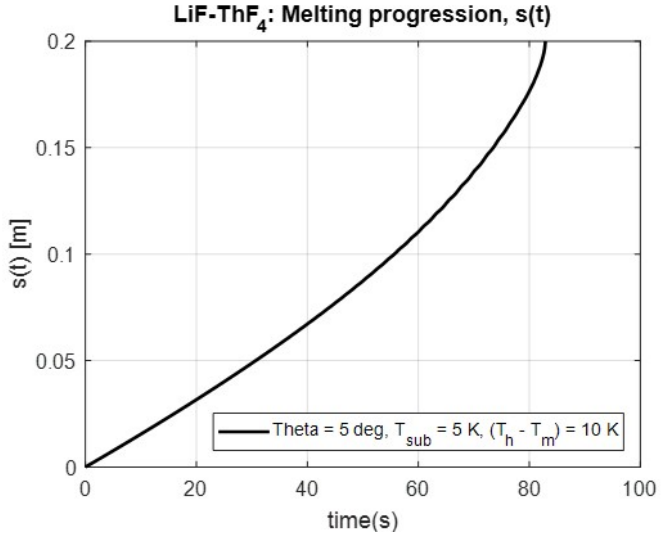

Figure 6.12: Melting progression of LiF-ThF_4 wedge plug with an angle fo 5 degrees, sub-cooling of 5 K and hot wall temperature of $T_m + 10$ K.

The primary difference between the MSFR plug and the experimental plug described above is the pressure boundary condition acting at the top of the plug. With the paraffin wedge, a significant proportion of melt was expected to be squeezed upward, ending up above the plug as it melted. Realistically, more substantial hydrostatic pressure will act on the plug in the MSFR. Indeed, as shown in Figure 6.13, subjecting the LiF-ThF_4 wedge to realistic hydrostatic pressure means that the maximum pressure in the thin molten layer will always occur at the top of the wedge, and that all the melt will drain out.

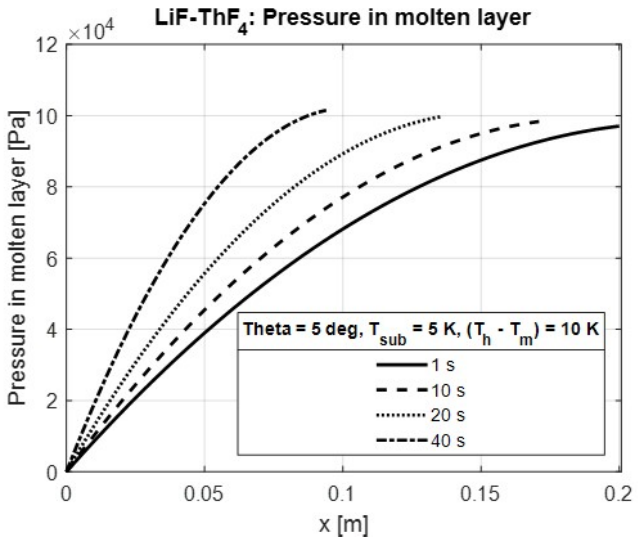

Figure 6.13: Pressure distribution in the thin molten layer of a LiF-ThF_4 wedge-plug after 1, 10, 20, and 40 s of melting in a reactor with a height of 2.225 m. An angle of 5 degrees, sub-cooling of 5 K and hot wall temperature of $T_m + 10$ K are assumed.

6.4.1. Effect of wedge angle, θ, and sub-cooling, T_{sub}

Melting times are linearly dependent on both the wedge angle (Figure 6.14a) and wedge-sub-cooling (Figure 6.14b). The melting times vary from 82 s for an angle of 5 degrees to 660 s for an angle of 45 degrees. The dependence on sub-cooling is weaker, with melting times increasing just 15 s when the sub-cooling is increased from 0 K to 50 K. It should be stressed that these are melting times beginning at the onset of melting, which will realistically be delayed with greater sub-cooling. Both graphs are based on the LiF-ThF_4 wedge heated isothermally to 10 K above the melting temperature.

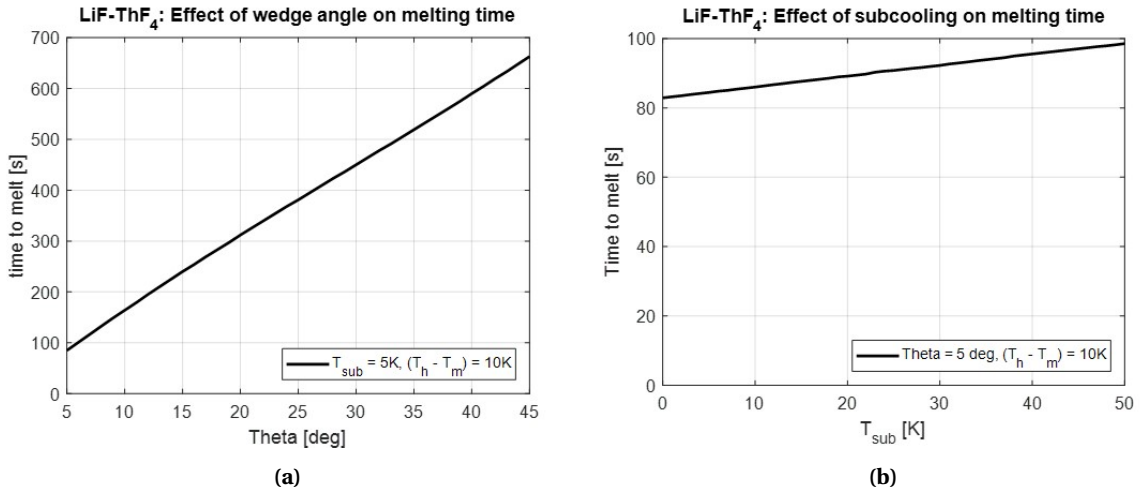

(a) **(b)**

Figure 6.14: Melting time as a function of the wedge angle (6.14a) and subcooling (6.14b) for the LiF-ThF_4 wedge with a temperature difference $(T_h - T_m)$ = 10 K. Based on numerical solutions.

6.4.2. Effect of Stefan number

Figure 6.15 shows the melting time of the wedge as a function of the Stefan number (represented here simply as the temperature difference, $(T_h - T_m)$), compared with the time required to melt 0.001m of LiF-ThF_4 according to the 1D Stefan problem for which the Neumann solution (Equation 2.7) applies. This is expected to roughly capture the time required to melt a cylindrical plug subjected to the same temperature boundary conditions. The distance of 0.001m was arbitrarily chosen as an amount of melting that would likely cause the plug to drop. For the wedge, an angle of 5 degrees and sub-cooling of 5K are assumed.

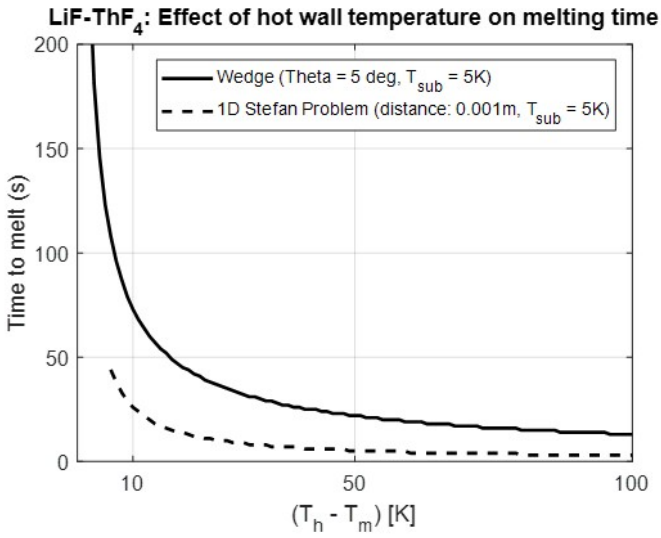

Figure 6.15: Melting time as a function of Stefan number, represented by $(T_h - T_m)$. The melting time for the LiF-ThF_4 wedge plug based on the numerical solution is compared with the time required to melt 0.001m of LiF-ThF_4 according to the Neumann solution for 1D melting. Sub-cooling of 5 K is assumed.

It is clear that the melting times of the wedge have the same temperature dependence as the Neumann solution, with melting times increasing exponentially as the Stefan number (and hence temperature difference) goes to zero. The Neumann solution is only shown for $(T_h - T_m) > 5$ because it is invalid for $(T_h - T_m) < T_{sub}$. This comparison shows that from the onset of melting, the time required to melt the wedge is approximately 2 - 5 times greater than the time to melt a non-wedge shaped plug.

7

Conclusions and Recommendations

As outlined in the research goals presented in Section 1.4, the objective of this thesis was two-fold:

1. To evaluate the feasibility of previous freeze plug designs, including the new SWATH design, in which a plug is melted through heat stored in metal blocks adjacent to the plug, and the decay heat design, in which the plug melts from decay heat produced in the core, and estimate the sensitivity of these designs to various parameters of interest; and

2. To conduct a preliminary investigation into a wedge-shaped freeze plug, which has potential advantages in terms of stability and reliability.

7.1. Conclusions: Existing Freeze Plug Designs

Both the SWATH and decay heat freeze plug designs were simulated in COMSOL using more realistic boundary conditions than have been considered in previous work (to the author's knowledge, the SWATH plug has not been simulated at all). In particular, including the draining pipe and cavity above the freeze plug allowed the steady-state solidified shape of the plugs to be simulated for the first time, including the presence of a thin frozen salt layer on top of the plugs in the case of a multi-plug design. This frozen salt layer is insulating, and inhibits the transfer of heat through the top of the copper grate. This ensures that the dominant heat transfer pathway to the freeze plugs is through the draining pipe wall, rather than the molten salt above the freeze plug. Simulations of both the SWATH and decay heat freeze plug designs showed that this insulating effect consistently renders a freeze plug consisting of a single plug the same width as the draining pipe superior to a design consisting of multiple smaller plugs encased in a copper plate.

More detailed result pertaining to the SWATH and decay heat studies are summarized below.

7.1.1. SWATH design

The single-plug design was found to melt at least 35% faster than all multi-plug configurations studied. Because the amount of mass that has to be melted in a single-plug design is minimal, melting times depend very minimally on the Stefan number of the plug material.

In general, the number of plugs (4 and 7 were considered) or the P/D ratio (which describes the ratio between the spacing between plugs and the plug diameter) had a smaller effect on the total melting time than other factors, such as the degree of plug sub-cooling.

At the experimental scale, using two 1250 W heating rings located 0.09 m above and below the freeze plugs allowed all plugs to melt within 30 s for sub-cooling of 5 K. These melting times depend linearly on sub-cooling; increasing sub-cooling to 25 K resulted in melting times of 80 s for the single plug, and 185 s for the multi-plug design (7 plugs, P/D = 1.05).

At the reactor scale, two 6375 W heating rings were used, located 0.36 m above and below the freeze plugs. The multi-plug, LiF-ThF_4 design with sub-cooling of 5 K, needed 250 - 350 s (depending on P/D ratio) before the edges of the plugs were melted, and needed at least 570 s before the frozen layer above the copper plate was fully melted as well. In contrast, the single-plug design melted in just under 200 s with sub-cooling of 5 K. The results from this study provide a preliminary indication that a freeze plug design which makes use of heating rings is feasible.

7.1.2. Decay heat design

The performance of the decay heat design was shown to be extremely sensitive to the distance between plug and reactor core. To melt within 600 s, a plug with sub-cooling of 5 K has to be located ≤ 0.10 m from the mixed core flow, regardless of whether a single or multi-plug design is used. At just 0.15 m from the core, melt times for all plugs exceed 1000 s. This confirms suggestions by Swaroop (2016) and Ghetta et al. (2017b) that the decay heat plug design is likely unfeasible as long as the design constraint - that the plug cannot be located close to the reactor core - holds.

The melting times of the multi-plug design are more sensitive to the plug sub-cooling than the single-plug design, due to the build-up of a frozen salt layer above the copper plate. Generally, the single plug is favorable to the multi-plug design for cavities ≥ 0.05 m and for sub-cooling about 5 K. However, if this frozen layer is ignored and only the interior edges of the plugs in the multi-plug design are considered, the single-plug takes slightly longer to melt. This contrasts with the trends seen in the SWATH design, where the single-plug design was always preferable, and highlights the importance of understanding the melting behavior of this layer.

As with the SWATH design, the P/D ratio was found to have an insignificant effect on melting times compared to other factors, such as the thickness of the frozen salt layer on top of the copper plate, sub-cooling, or cavity height.

7.2. Recommendations: Existing Freeze Plug Designs

- A freeze plug which relies on decay heat from the core to melt is unfeasible unless the freeze plug is located within 0.01 m of the core, and should therefore not be pursued further unless the mixing of decay heat in the draining pipe is increased such that it extends within 0.01 m of the plug.
- A freeze plug which relies on heating rings to melt is probably feasible, and warrants further study. In particular, care should be taken to ensure that the draining pipe can withstand the continuous high temperatures of the heating rings, which are expected to be approximately 1000 K based on this study.
- Based on the results of this thesis, the single freeze plug is recommended over a multi-plug design due to the inefficient melting of the thin frozen layer above the copper plate in the multi-plug design. However, for a definitive assessment of the feasibility of the multi-plug design, a model is necessary which accounts for the continuous sinking of this layer due to the hydrostatic pressure in the reactor. It is expected that this will result in melting times that are more comparable to (but still longer than) those of the single-plug. Moreover, the frozen layer may also make such a multi-plug design more stable during transient reactor operation, keeping the plugs from slowly slipping downward, while using multiple smaller plugs may be more reliable, preventing jamming of the draining pipe. Based on the uncertainty in melting speed and inherent safety advantages of this design, it is therefore recommended for further study in the event that the wedge shaped design alternative, described below, is not pursued.
- If a multi-plug design is pursued, a configuration should be chosen to maximize the draining speed of the reactor.
- Future efforts to optimize the freeze plug should focus on enhancing heat transfer through the draining pipe.
- The stability of the freeze plug during transient reactor operation should be studied, in particular: The sub-cooling required to prevent the plug from melting due to expected fluctuations in the reactor's temperature and the plug's cooling system, the effect of flow in the core on the shape of the plug, and whether the friction between the frozen salt and the metal grate is sufficient to keep the cylindrical plugs in place, with and without an additional frozen layer in the case of the multi-plug design.

7.3. Conclusions: Wedge Shaped Freeze Plug Design

In this thesis an alternative, wedge-shaped freeze plug design was proposed and simulated in COMSOL. Unlike a single, cylindrical plug, the wedge shape ensures that the plug remains in place during transient reactor operation. At the same time, the draining pipe is not obstructed, and the uncertain role of the thin frozen layer in the multi-plug design, with regards to both melting speed, stability and reliability, is avoided.

Studying the wedge-shaped plug required coupling the apparent heat capacity method, used to model phase change in COMSOL, with convection in the flow (through the enthalpy-porosity approach) as well as the sinking of the solid phase in a phenomena known as close-contact melting. Since both the coupling of the

apparent heat capacity method with convection and close-contact melting present unique numerical challenges, these phenomena were first studied independently through validation studies common to the phase change literature. These validation studies were used to determine the methodology to use for simulating the wedge-shaped plug. To model close-contact melting, an analytical description was additionally derived for the melting of the wedge, and was validated experimentally.

Below, the results of these validation studies are presented along with a preliminary analysis of the wedge-shaped plug.

7.3.1. Convection validation

The coupling with convection was studied by replicating a reference study of melting with natural convection. Accurate results were obtained by limiting the penetration of the flow into the 'mushy zone' at the melting front as mush as possible. Specifically, the accuracy of the solution proved to be quite sensitive to solver tolerances and porosity constant used. Replacing the traditional porosity function, based on flow through porous media with a new function based on the hyperbolic tangent was found to improve results further.

7.3.2. Close-contact melting validation

The coupling with close-contact melting was studied by replicating a reference study of close-contact melting inside a horizontal cylinder. An extended Darcy term approach was used in which the sinking velocity of the solid was prescribed semi-analytically, and the molten layer thickness between the solid and heated exterior is predefined. By selecting an appropriate proportionality constant for the sinking velocity, a solution was obtained which closely resembled the reference solution by Bareiss & Beer (1984). The results obtained in this study more closely resemble experimental findings than previous studies conducted with commercial software, in which the settling of the solid is generally achieved by relaxing the viscosity or porosity, leading to a poorly defined melting front.

7.3.3. Close-contact melting of wedge plug

In order to apply the extended Darcy term approach to the wedge, an analytical solution was first derived for the melting wedge, assuming isothermal heating. This solution showed good agreement with a table top experiment involving the melting of a paraffin wedge in a heated glass funnel. Unlike most examples of close-contact melting that have been studied to date, the analytical model and experiment revealed that the melting of the wedge is unsteady. Towards the end of the melting process, the sinking velocity rapidly increases, while the thickness of the molten layer rapidly decreases.

With the appropriate proportionality constant, COMSOL simulations of the paraffin wedge accurately captured the melting of the plug for the first 70% of the melting time, during which time the melting progression is roughly steady. However, the COMSOL simulation currently does not capture the rapid acceleration toward the end of the melting process, and therefore over-estimates the total melting time.

Applying the analytical model to the LiF-ThF_4 wedge revealed a linear dependence between the time required for the wedge to melt fully and both the wedge angle, and wedge sub-cooling. On the other hand, melting times were found to depend non-linearly on the temperature of the heated wall. As an example, a wedge plug with realistic dimensions for the MSFR (i.e., lower diameter and height of 0.20 m, wedge angle of five degrees), with uniform sub-cooling of 5 K, and heated uniformly to temperature $T_h = T_m + 10$ K, is predicted to melt in 82 s, which is at least twice as long as needed to melt a cylindrical plug subject to the same isothermal boundary conditions

Unfortunately, this study was not able to estimate how much longer it would take to melt a wedge-shaped plug than a traditional cylindrical plug subjected to realistic, non-isothermal boundary conditions.

7.4. Recommendations: Wedge Shaped Freeze Plug Design

- The enthalpy-porosity method is recommended for future studies of melting or solidification of the freeze plug with convection in COMSOL. A hyperbolic tangent function (Equation 2.25) should be used instead of the traditional Darcy term. The solver tolerances should be set as small as possible (10^{-4} yielded good results in the present study), and a porosity constant of at least $C = 5{\cdot}10^7$ is recommended.

- The extended Darcy term approach, while shown to be useful for modeling steady contact melting behavior, is less suitable for unsteady problems such as the wedge, or contact melting problems involving arbitrary geometries, such as the thin frozen layer previously seen in the multi-plug design. In order

to properly model these plugs, an extended Darcy term approach should be used with the immersed boundary method (see, for example Faden et al. (2018); Kozak & Ziskind (2017)). Since this cannot be done in COMSOL, a more customizable numerical solver such as OpenFOAM is recommended for future study of the freeze plug.

A

SWATH Design Data

Table A.1: Experimental scale freeze plug with 1 and 4 plugs: P/D ratio study parameters and results.

		1 plug	**4 plugs**				
	P/D Ratio	**1**	**1.05**	**1.25**	**1.5**	**1.75**	**2.0**
Model	% Open	100%	62%	44%	31%	22%	17%
	h_{air} [W·m^{-2}K^{-1}]	186	239	286	349	417	490
	Copper thickness [m]	0.05	0.02	0.016	0.014	0.012	0.01
Steady State	T_{sub} [K]	5	5	5	5	5	5
	Max. Pipe temp. [K]	972	1004	1007	1010	1011	1012
	Frozen salt above grate [%]	3%	11%	13%	16%	20%	24%
	Frozen salt above grate [m]	1.50E-03	2.15E-03	2.09E-03	2.14E-03	2.37E-03	2.46E-03
	Min. plug height as % of grate	71%	95%	100%	107%	113%	118%
Time to melt	**Interior edge [s]**	**14**	**22**	**21**	**24**	**25**	**29**
	Exterior edge[s]		14	19	20	25	27

Table A.2: Experimental scale freeze plug with 7 plugs: P/D ratio study parameters and results.

		7 plugs				
	P/D Ratio	**1.05**	**1.25**	**1.5**	**1.75**	**2.0**
Model	% Open	70%	50%	34%	25%	19%
	h_{air} [W·m^{-2}K^{-1}]	299	363	449	545	647
	Copper thickness [m]	0.016	0.013	0.011	0.0095	0.008
Steady State	T_{sub} [K]	5	5	5	5	5
	Max. Pipe temp. [K]	1008	1011	1012	1012	1013
	Frozen salt above grate [%]	15%	19%	22%	26%	32%
	Frozen salt above grate [m]	2.42E-03	2.55E-03	2.41E-03	2.50E-03	2.65E-03
	Min. plug height as % of grate	99%	106%	113%	119%	125%
Time to melt	**Interior edge [s]**	**20**	**23**	**24**	**28**	**30**
	Exterior edge[s]	14	19	23	29	29

Table A.3: Experimental scale freeze plug with 7 plugs: Aspect ratio and T_{sub} study parameters and results.

		7 Plugs						
	Aspect ratio	**1**	**1**	**1**	**1**	**1**	**0.5**	**1.5**
	$\boldsymbol{T_{sub}}$ [K]	**5**	**10**	**15**	**20**	**25**	**5**	**5**
Model	h_{air} [W·m^{-2}K^{-1}]	299	303	307	311	314	690	198
	Copper Plate thickness [m]			0.016			0.008	0.024
Steady State	Max. pipe temp. [K]	1008	1003	998	994	989	1013	1000
	Frozen salt above grate [%]	15%	31%	44%	57%	70%	35%	9%
	Min. plug height as % of grate	99%	121%	136%	151%	164%	101%	98%
Time to Melt	**Interior edge [s]**	**20**	**53**	**81**	**120**	**169**	**26**	**20**
	Exterior edge [s]	14	24	35	47	57	17	13

Table A.4: Experimental scale freeze plug with 1 plug: T_{sub} study parameters and results.

		1 Plug				
	$\boldsymbol{T_{sub}}$ [K]	**5**	**10**	**15**	**20**	**25**
Model	h_{air} [W·m^{-2}K^{-1}]	186	188	191	193	195
	Copper Plate thickness [m]			0.05		
Steady State	Max. pipe temp. [K]	972	967	962	957	952
	Frozen salt above grate [%]	3%	7%	11%	15%	19%
	Min. plug height as % of grate	71%	87%	97%	104%	111%
Time to Melt	**Exterior edge [s]**	**14**	**24**	**36**	**49**	**63**

Table A.5: Reactor scale freeze plug with 7 plugs: P/D study for LiF-NaF-KF and LiF-ThF_4 fuels.

		7 Plugs					
		LiF-NaF-KF			**LiF-ThF_4**		
	P/D Ratio	**1.05**	**1.5**	**2.0**	**1.05**	**1.5**	**2.0**
Model	% Open	71%	34%	19%	71%	34%	19%
	h_{air} [W·m^{-2}K^{-1}]	89	127	174	69	99	134
	Copper Plate thickness [m]	6.35E-02	0.044	0.033	0.0635	0.044	0.033
Steady State	T_{sub}[K]	5	5	5	5	5	5
	Max. pipe temp. [K]	1081	1085	1048	1194	1153	1154
	Frozen salt above grate [%]	11%	16%	24%	11%	17%	25%
Time to Melt ($\theta_s < 1.0$)	**Interior edge [s]**	**265**	**330**	**375**	**750**	**1000**	**905**
	Exterior edge [s]	180	325	360	295	905	855
Time to Melt ($\theta_s < 0.5$)	**Interior edge [s]**	**230**	**270**	**300**	**570**	**735**	**760**
	Exterior edge [s]	175	250	290	270	725	745
	Interior grate edge [s]	220	205	220	350	260	280
	Exterior grate edge [s]	175	195	195	165	195	210

Table A.6: Reactor scale freeze plug with 1 plug: T_{sub} study parameters and results.

		1 Plug									
		LiF-NaF-KF					**LiF-ThF$_4$**				
	$\boldsymbol{T_{sub}}$ [K]	**5**	**10**	**15**	**20**	**25**	**5**	**12**	**18**	**25**	**31**
Model	h_{air} [W·m^{-2}K^{-1}]	56	57	57	58	59	44	45	45	46	46
	Copper thickness [m]			0.2					0.2		
Steady State	Max. pipe temp. [K]	1040	1035	1030	1025	1020	1154	1148	1141	1135	1129
	Salt above grate [%]	2%	5%	8%	12%	15%	2%	6%	10%	14%	18%
	Min. plug height [%]	66%	81%	90%	97%	103%	66%	84%	95%	103%	109%
Time to Melt	**Exterior edge [s]**	**175**	**300**	**435**	**575**	**730**	**195**	**360**	**540**	**735**	**950**

B

Decay Design Data

Table B.1: 1-plug Design

Cavity height (m)	**0.01**					**0.05**					**0.10**					**0.15**					**0.20**				
T_{sub} (K)	5	10	15	20	25	5	10	15	20	25	5	10	15	20	25	5	10	15	20	25	5	10	15	20	25
Max. plug height (m)	0.195	0.200	0.201	0.201	0.202	0.202	0.204	0.207	0.209	0.211	0.205	0.210	0.214	0.219	0.222	0.207	0.215	0.222	0.228	0.234	0.210	0.220	-	-	-
Outer melting time (s)	110	140	160	180	200	280	375	435	500	555	570	715	850	970	1110	1030	1295	1480	1650	1800	1520	1910			

Table B.2: 7-plug design, P/D = 1.05

Cavity height (m)	**0.01**					**0.05**					**0.10**					**0.15**					**0.20**				
T_{sub} (K)	5	10	15	20	25	5	10	15	20	25	5	10	15	20	25	5	10	15	20	25	5	10	15	20	25
Copper plate thickness (m)	0.063	0.063	0.063	0.063	0.063	0.063	0.063	0.063	0.063	0.063	0.063	0.063	0.063	0.063	0.063	0.063	0.063	0.063	0.063	0.063	0.063	0.063	0.063	0.063	0.063
Max. plug height (m)	0.060	0.064	0.064	0.064	0.065	0.065	0.068	0.070	0.072	0.074	0.068	0.073	0.078	0.082	0.086	0.068	0.075	0.083	0.089	0.095	0.070	0.081	0.091	0.100	0.107
Thickness of salt layer above plate (m)	0.000	0.000	0.001	0.001	0.001	0.002	0.004	0.007	0.008	0.011	0.004	0.010	0.014	0.019	0.023	0.005	0.012	0.019	0.025	0.031	0.007	0.017	0.027	0.037	0.044
Outer melting time (s)	20	30	35	45	55	85	150	200	270	285	240	385	580	640	650	495									
Inner melting time (s)	0	80	100	110	120	220	325	510	660	770	535	1210	1675	1980	nm	1240									
Outer melting time-plate edge only (s)	20	30	35	45	55	85	140	185	260	260	215	350	545	595	625	375									
Inner melting time-plate edge only (s)	0	80	100	110	120	220	310	355	415	415	530	660	785	800	915	875									

Table B.3: 7-plug design, P/D = 1.25

Cavity height (m)	**0.01**					**0.05**					**0.10**					**0.15**					**0.20**				
T_{sub} (K)	5	10	15	20	25	5	10	15	20	25	5	10	15	20	25	5	10	15	20	25	5	10	15	20	25
Copper plate thickness (m)	0.053	0.053	0.053	0.053	0.053	0.053	0.053	0.053	0.053	0.053	0.053	0.053	0.053	0.053	0.053	0.053	0.053	0.053	0.053	0.053	0.053	0.053	0.053	0.053	0.053
Max. plug height (m)	0.053	0.053	0.054	0.054	0.055	0.055	0.057	0.059	0.062	0.064	0.057	0.063	0.067	0.071	0.076	0.059	0.067	0.074	0.080	0.086	0.062	0.073	0.083	0.090	0.099
Thickness of salt layer above plate (m)	0.000	0.000	0.001	0.001	0.001	0.001	0.004	0.006	0.008	0.010	0.004	0.009	0.014	0.018	0.023	0.006	0.014	0.021	0.027	0.033	0.009	0.019	0.029	0.037	0.045
Outer melting time (s)	15	25	35	40	55	80	245	340	410	450	460	730	870	985	970	965									
Inner melting time (s)	20	50	65	75	95	155	345	525	660	790	600	1310	1790	1955	nm	1325									
Outer melting time - plate edge only (s)	15	25	35	40	55	75	130	175	215	270	195	330	430	555	635	355									
Inner melting time - plate edge only (s)	20	50	65	75	95	155	210	260	295	350	380	475	560	675	760	615									

Table B.4: 7-plug design, P/D = 1.50

Cavity height (m)	**0.01**					**0.05**					**0.10**					**0.15**					**0.20**				
T_{sub} (K)	5	10	15	20	25	5	10	15	20	25	5	10	15	20	25	5	10	15	20	25	5	10	15	20	25
Copper plate thickness (m)	0.044	0.044	0.044	0.044	0.044	0.044	0.044	0.044	0.044	0.044	0.044	0.044	0.044	0.044	0.044	0.044	0.044	0.044	0.044	0.044	0.044	0.044	0.044	0.044	0.044
Max. plug height (m)	0.044	0.045	0.045	0.045	0.046	0.046	0.048	0.051	0.053	0.055	0.049	0.054	0.059	0.063	0.067	0.051	0.059	0.066	0.073	0.078	0.054	0.064	0.074	0.083	0.090
Thickness of salt layer above plate (m)	0.000	0.000	0.001	0.001	0.001	0.002	0.004	0.006	0.008	0.010	0.004	0.009	0.014	0.018	0.022	0.007	0.014	0.022	0.028	0.033	0.010	0.020	0.029	0.038	0.046
Outer melting time (s)	10	20	30	40	45	90	275	405	495	485	435	895	1005	1065	1325	1115	1790	nd	nd	nd	1895	nd	nd	nd	nd
Inner melting time (s)	10	40	55	70	75	125	355	505	630	775	500	1135	1655	1845	nm	1395	nm	nd	nd	nd	nm	nd	nd	nd	nd
Outer melting time-plate edge only (s)	10	20	30	40	45	65	135	160	200	235	180	380	420	485	580	380	550	nd	nd	nd	475	nd	nd	nd	nd
Inner melting time-plate edge only (s)	10	40	55	70	75	125	200	225	265	300	295	485	535	585	675	598	720	nd	nd	nd	925	nd	nd	nd	nd

C

Wedge Plug Design

C.1. Mesh sensitivity study

A mesh sensitivity study was performed on both boundary layer mesh and interior mesh. Following the same method described for the horizontal cylinder in Section 3.3.5, the total number of elements spanning the width of the boundary layer was varied from 6 to 24, while the maximum size of the triangular mesh was varied from $1.6 \cdot 10^{-4}$ to $5.0 \cdot 10^{-4}$m. The proportionality constant was taken to be $c = 5 \cdot 10^{-6}$, and the reference point, x_p was located a distance $\delta = 2 \cdot 10^{-4}$m from the edge, equivalent to approximately half the expected average width of the molten layer.

Figure C.1 shows the progression of the top of the melting front as a function of time for the different mesh. The solution does not vary with refinement, but is slightly less smooth for the courses interior mesh. Based on these results, and because computing time did not differ substantially between these simulations, the intermediate interior mesh and minimum number of boundary layer elements were considered most appropriate.

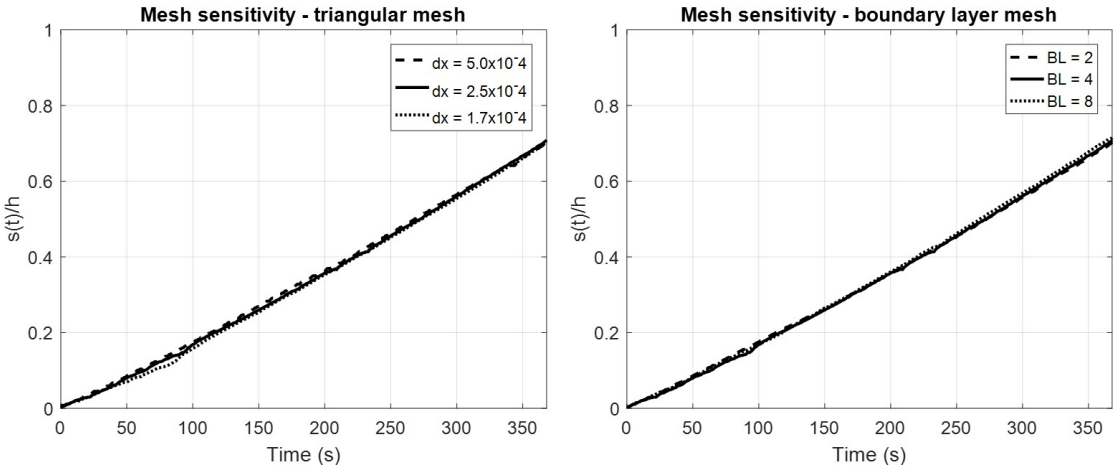

Figure C.1: Shift in top melting front of wedge plug as function of time for increasing number of boundary layer mesh elements and triangular mesh element size; $c = 5 \cdot 10^{-6}$.

C.2. Paraffin plug experiment with 50 g weight

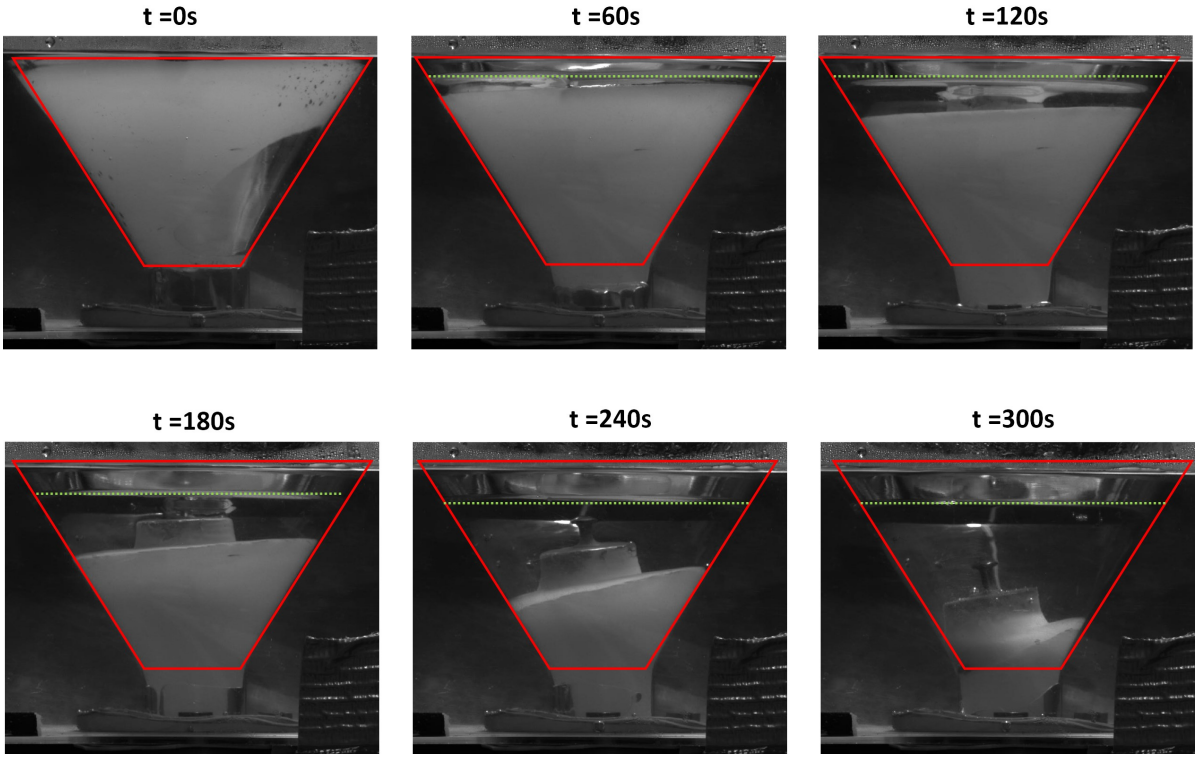

Figure C.2: Melting progression of paraffin plug with additional 50g weight. The original size of the plug is outlined in red, and the height of the molten paraffin is shown in green.

D

COMSOL Settings

The specific solver settings used in the above simulations were determined in part through trial and error, and by the recommendation of COMSOL support staff. A fully coupled solver, which essentially uses the Newton Raphson approach, was used in Section 3.2 for melting with natural convection. For modeling close contact melting, much better convergence was achieved with a segregated solver, which iterates between the heat transfer and fluids physics. However, this was not realized during the study of the horizontal cylinder (Section 3.3), and was therefore only implemented for the study of the wedge-shaped plug.

For melting with convection (with and without close contact melting), results were found to be very sensitive to the tolerance on the convergence criteria, which were therefore made to be as strict as possible without inhibiting convergence. The absolute tolerance in the time-dependent solver was set at $5 \cdot 10^{-4}$ in all studies. For melting with natural convection (Section 3.2), a tolerance of $5 \cdot 10^{-8}$ was used in the fully coupled solver. For the contact melting studies, a slightly more relaxed tolerance of $5 \cdot 10^{-6}$ was used in the fully coupled and segregated solvers, respectively.

Unless noted, the maximum time step was restricted to 0.01 s in all simulations; this was found to be appropriate for the ranges of mesh used. Linear elements were always used, after finding no improvement in the solution accuracy from using higher order elements. The default P1 + P1 discretization was applied to the fluids module, which uses first order elements for velocity and pressure. Streamline and crosswind stabilization are applied by default. A first order backward differences time integration scheme was used because of its stability for transport problems with large gradients. For more detailed information about the tolerances and convergence criteria used in COMSOL, the reader is referred to the COMSOL Multiphysics Reference Manual (COMSOL, 2016).

Bibliography

(2016). International energy outlook 2016. Report DOE/EIA-0484(2016), EIA (US Energy Information Administration).

Alexiades, V., & Solomon, A. D. (1993). *Mathematical Modeling of Melting and Freezing Processes*. Hemisphere Publishing Corporation.

Allibert, M., Gerardin, D., Heuer, D., Huffer, E., Laureau, A., Merle, E., Beils, S., Cammi, A., Carluec, B., Delpech, S., Gerber, A., Girardi, E., Krepel, J., Lathouwers, D., Lecarpentier, D., Lorenzi, S., Luzzi, L., Poumerouly, S., Ricotti, M., & Tiberi, V. (2016). D1.1 description of initial reference design and identification of safety aspects. Report, SAMOFAR.

Assis, E., Katsman, L., Ziskind, G., & Letan, R. (2007). Numerical and experimental study of melting in a spherical shell. *International Journal of Heat and Mass Transfer*, *50*, 1970 – 1804.

Bareiss, M., & Beer, H. (1984). An analytical solution of the heat transfer process during melting of an unfixed solid phase change material inside a horizontal tube. *International Journal of Heat and Mass Transfer*, *27*(5), 739–746.

Bejan, A. (2013). *Convection Heat Transfer*. Wiley.

Benes, M., & Konings, R. (2009). Thermodynamic properties and phase change diagrams of flouride salts for nuclear applications. *Journal of Flourine Chemistry*, *130*, 22–29.

Bertrand, B., O.and Binet, Combeau, H., Couturier, S., Delannoy, Y., Gobin, D., Lacroix, M., Le Quere, P., Medale, M., Mencinger, J., Sadat, H., & Vierira, G. (1999). Melting driven by natural convection, a comparison exercise: first results. *Int. J. Therm. Sci*, *38*, 5–26.

Binet, B., & Lacroix, M. (1998). Numerical study of natural-convection-dominated melting inside uniformly and discretely heated rectangular cavities. *Numerical Heat Transfer, Part A: Applications*, *33*(2), 207–224.

Brent, A. D., Voller, V. R., & Reid, K. J. (1988). Enthalpy-porosity technique for modeling convection-diffusion phase change: Application to the melting of a pure metal. *Numerical Heat Transfer*, *13*(3), 297–318.

Brovchenko, M., Heuer, D., Merle-Lucotte, E., Allibert, M., Ghetta, V., Laureau, A., & Rubiolo, P. (2013). Design-related studies for the preliminary safety assessment of the molten salt fast reactor. *Nuclear Science and Engineering*, *175*(3), 329–339.

Capelli, E., Benes, M., & Konings, R. (2013). Thermodynamic investigation of the LiF-ThF4 system. *J. Chem. Thermodynamics*, *58*, 110–116.

COMSOL (2016). COMSOL multiphysics reference manual. Report.

Deurvorst, F. (2017). *Design of Cooling Fins on the Freeze Plug*. Bachelor's thesis, Delft University of Technology.

Erturk, E., Corke, T., & Gokcol, C. (2005). Numerical solutions of 2-d steady incompressible driven cavity flow at high reynolds numbers. *International Journal for NUmerical Methods in Fluids*, *48*, 747 – 774.

Ettouney, H., Alitiqi, I., Al-Sahali, M., & Al-Hajirie, K. (2006). Heat transfer enhancement in energy storage in spherical capsules filled with paraffin wax and metal beads. *Energy conversion and management*, *47*, 211–228.

Faden, M., Konig-Haagen, A., Hohlein, S., & Bruggemann, D. (2018). An implicit algorithm for melting and settling of phase change material inside macrocapsules. *International Journal of Heat and Mass Transfer*, *117*, 757–767.

Ghetta, V., Giraud, J., Rubiolo, P., & Tano-Retamales, M. (2017a). D3.1 MSFR fuel salt conditions during typical draining transients. Report, SAMOFAR.

Ghetta, V., Giraud, J., Rubiolo, P., & Tano-Retamales, M. (2017b). D3.3 design and building of SWATH experiment (shut-down system). Report, SAMOFAR.

Groulx, D., & Lacoix, M. (2006). Study of close contact melting of ice from a sliding heated flat plate. *International Jounral of Heat and Mass Transfer*, *49*, 4407–4416.

Gudibande, N., & Iyer, K. (2017). Numerical simulation of contact melting using the cell-splitting modified enthalpy method. *Numerical heat transfer, Part B*, *71*, 84–107.

Hannoun, N., Alexiades, V., & Mai, T. Z. (2003). Resolving the controversy over tin and gallium melting in a rectangular cavity heated from the side. *Numerical Heat Transfer, Part B: Fundamentals*, *44*, 253 – 276.

Hannoun, N., Alexiades, V., & Mai, T. Z. (2005). A reference solution for phase change with convection. *International Journal for Numerical Methods in Fluids*, *48*, 1283–1308.

Haubenreich, P. N., & Engel, J. R. (1970). Experience with the molten-salt reactor experiment. *Nuclear Applications and Technology*, *8*, 118 – 136.

Hosseinizadeh, S., Rabienataj Darzi, A. A., Tan, F. L., & Khodadadi, J. M. (2013). Unconstrained melting inside a sphere. *International Journal of Thermal Sciences*, *63*, 55–64.

Iwatsu, R., & Hyun, J. M. (1995). Three-dimensional driven-cavity flows with a vertical temperature gradient. *International Journal of Heat and Mass Transfer*, *63*(18), 3319–3328.

Iwatsu, R., Hyun, J. M., & Kuwahara, K. (1993). Mixed convection in a driven cavity with a stable vertical temperature gradient. *International Journal of Heat and Mass Transfer*, *36*(6), 1601–1608.

Jianfeng, L., Jing, D., & Jianping, Y. (2010). Solidification and melting behaviors and characteristics of molten salt in cold filling pipe. *International Journal of Heat and Mass Transfer*, *53*, 1628–1635.

Jin, X., Huoyan, H., Shi, X., Zhou, X., & Zhang, X. (2018). Comparison of two numerical heat transfer models for phase change material board. *Applied Thermal Engineering*, *128*, 1331–1339.

Kasibhatla, R. R., Konig-Haagen, A., Rosler, F., & Bruggemann, D. (2017). Numerical modeling of melting and settling of an encapsulated PCM using variable viscosity. *Heat Mass Transfer*, *53*, 1735–1744.

Kowalewski, T. A., & Gobin, D. (2004). *Phase Change with Convection: Modelling and Validation*, vol. 449. Springer-Verlag Wien, 1 ed.

Kozak, Y., Rozenfeld, T., & Ziskind, G. (2014). Close-contact melting in vertical annular enclosures with a non-isothermal base: Theoretical modeling and application to thermal storage. *International Journal of Heat and Mass Transfer*, *72*, 114–127.

Kozak, Y., & Ziskind, G. (2017). Novel enthalpy method for modeling of pcm accompanied by sinking of the solid phase. *International Journal of Heat and Mass Transfer*, *112*, 568–586.

Kumar, A., & Roy, S. (2010). Heat transfer characteristics during melting of a metal spherical particle in its own liquid. *International Journal of Thermal Sciences*, *49*, 397–408.

Lacroix, M., & Voller, V. R. (1990). Finite difference solutions of solidification phase change problems: Transformed versus fixed grids. *Numerical Heat Transfer, Part B: Fundamentals*, *17*(1), 25–41.

Mahaffey, J. (2014). *Atomic Accidents: A History of Nuclear Meltdowns and Disasaters*. Pegaus Books.

Makkinje, A. (2017). *Design of a Freeze Plug Grate*. Bachelor's thesis, Delft University of Technology.

Malavasi, S., Messa, G., Fratino, U., & Pagano, A. (2012). On the pressure losses through perforated plates. *Flow measurement and instrumentation*, *28*, 57–66.

Moallemi, K. K., Webb, B. W., & Viskanta, R. (1986). An experimental and analytical study of close-contact melting. *ASME Journal of Heat Transfer*, *108*, 895–899.

Myers, T., Mitchell, S., & Muchatibaya, G. (2008). Unsteady contact melting of a rectangular cross-section material on a flat plate. *Physics of fluids*, *20*.

Richardson, M. (1962). Development of freeze valve for use in the MSRE. Report ORNL-TM-128, Oak Ridge National Laboratory.

Robertson, R. (1965). MSRE design and operations report, part 1, description of reactor design. Report ORNL-TM-728, Oak Ridge National Laboratory.

Rohatgi, A. (2017). Webplotdigitizer version 4.1.
URL `https://automeris.io/WebPlotDigitizer`

Rozenfeld, T., Hayat, R., Kozak, Y., & Ziskind, G. (2015). Enhanced melting for transient thermal management. In *Proceedings of the ASME 2015 International Technical Conference and Exhibition on Packaging and Integration of Electronic and Photonic Microsystems*.

Samara, F., Groulx, D., & Biwole, P. H. (2012). Natural convection driven melting of phase change material: Comparison of two methods. In *Proceedings of the 2012 COMSOL Conference in Boston*.

Shmueli, H., Ziskind, G., & Letan, R. (2010). Melting in a vertical cylindrical tube: Numerical investigation and comparison with experiments. *International Journal of Heat and Mass Transfer*, *53*(19-20), 4082–4091.

Sigma-Aldrich (2017). Paraffin wax product comparison guide.
URL `https://www.sigmaaldrich.com/catalog/substance/paraffinwax123458002742l1?lang=en&region=NL&attrlist=Transition%20temperature`

Sparrow, E. M., & Broadbent, J. A. (1982). Inward melting in a vertical tube which allows free expansion of the phase-change medium. *Journal of Heat Transfer*, *104*(2), 309.

Sparrow, E. M., & Geiger, G. T. (1986). Melting in a horizontal tube with the solid either constrained of free to fall under gravity. *Int. J. Heat Mass Transfer*, *29*(7), 1007–1019.

Swaroop, P. (2016). *Design of a Freeze Plug for the Molten Salt Fast Reactor (MSFR)*. Master's thesis, Delft University of Technology.

Tano, M. (2017). personal communication.

Tano, M., Rubiolo, P., & Doche, O. (2017). Progress in modeling solidification in molten salt coolants. Report, Oak Ridge National Laboratory.

Thornton, G. (1963). Introduction to nuclear propulsion- introduction and background lecture 1. Report, NASA.

van Noorden, T. (2017). personal communication.

van Tuyll, F. (2016). *A new design for the safety plug in a Molten Salt Fast Reactor*. Master's thesis, Delft University of Technology.

Viswanath, R., & Jaluria, Y. (1993). A comparison of different solution methodologies for melting and solidification problems in enclosures. *Numerical Heat Transfer*, *24*, 77–105.

Voller, V., & Cross, M. (1981). Accurate solutions of moving boundary-problems using the enthalpy method. *International Journal of Heat and Mass Transfer*, *24*(3), 545–556.

Voller, V. R., & Prakash, C. (1987). A fixed grid numerical modelling methodology for convection-diffusion mushy region phase-change problems. *International Journal of Heat and Mass Transfer*, *30*(8), 1709–1719.

Voller, V. R., Swaminathan, C. R., & Thomas, B. G. (1990). Fixed grid techniques for phase-change problems - a review. *International Journal for Numerical Methods in Engineering*, *30*(4), 875–898.

Wang, S., Massone, M., Rineiski, A., & Merle-Lucotte, E. (2016). Analytical investigation of the draining system for a molten salt fast reactor.

Williams, D. F. (2006). Additional physical property measurements and assessment of salt compositions proposed for the intermediate heat transfer loop. Report, ORNL.

Williams, D. F., Toth, L. M., & Clarno, K. T. (2006). Assessment of candidate molten salt coolants for the advanced high-temperature reactor (AHTR). Report TM-2006/12, ORNL.